Sun, Yudong:

Probing local current measurements at finite temperature
A numerical toolkit for bosonic flux ladders

Masterarbeit, Sommersemester 2025

Gutachter*in: Schollwöck, Ulrich ; Paeckel, Sebastian

Fakultät für Physik

Ludwig-Maximilians-Universität München

https://doi.org/10.5282/ubm/epub.127284

Probing Local Current Measurements at Finite Temperatures: a Numerical Toolkit for Bosonic Flux Ladders

Yudong Sun

München 2025

Lokale Strommessungen bei endlichen Temperaturen: ein numerisches Toolkit für bosonische Flussleiter

Yudong Sun

Masterarbeit
an der Fakultät für Physik
der Ludwig–Maximilians–Universität
München

vorgelegt von
Yudong Sun

München, den 7. Juli 2025

Betreut von
Prof. Dr. Ulrich Schollwöck und Dr. Sebastian Paeckel
in Zusammenarbeit mit Prof. Dr. Monika Aidelsburger

Probing Local Current Measurements at Finite Temperatures: a Numerical Toolkit for Bosonic Flux Ladders

Yudong Sun

Master Thesis
Faculty of Physics
Ludwig–Maximilians–University of Munich

submitted by
Yudong Sun

Munich, 7th July 2025

Supervised by
Prof. Dr. Ulrich Schollwöck and Dr. Sebastian Paeckel
in collaboration with Prof. Dr. Monika Aidelsburger

Abstract

Bosonic flux ladders serve as a promising framework for exploring gauge theories and investigating fundamental phenomena in condensed matter physics, as they exhibit non-trivial topology due to the presence of an artificial magnetic field. While conventional non-topological phases are typically characterized by local densities, topological phases, such as the recently experimentally realized Meissner phase, are captured only by local currents, necessitating different measurement protocols.

In this thesis, we investigate the measurement of local currents in ultracold atomic bosonic flux ladders, focusing on the discrepancy between experimentally measured currents and numerical simulations, particularly in the context of finite-temperature effects. We rigorously investigate the dynamic current measurement protocol proposed by Kessler and Marquardt (2014) through analytical derivations and numerical simulations with exact diagonalisation (ED), assessing the impact of the employed approximations on measurement outcomes. We observe that non-bosonic statistics arising from finite-dimensional Hilbert spaces introduce systematic errors for ground states and thermal states, which are however subleading compared to the uncertainties arising from the parity-projected measurement. We identify possible criteria for the validity of the protocol in the absence of parity projection, but find isolating finite-temperature effects challenging due to the numerous competing error sources.

Further comparison of the directly measurable rung correlator with larger-system finite-temperature matrix product state (MPS) simulations suggests that the experimentally realised state is neither a ground state nor a thermal state, but rather a non-equilibrium state. Additionally, we develop and benchmark a robust numerical toolkit for bosonic flux ladders, enabling exact results (small systems) and approximate results (large systems) across unified ED/MPS interfaces based on existing toolkits.

Our work underscores fundamental limitations of modern local current measurement protocols in quantum gas microscopes and provides pathways for future theoretical and experimental refinements.

Zusammenfassung

Bosonische Flussleitern bieten sich als eine vielversprechende Plattform für die Erforschung von Eichtheorien und grundlegenden Phänomenen in der Physik der kondensierten Materie an, da sie aufgrund eines künstlichen Magnetfelds nichttriviale Topologie aufweisen. Während konventionelle nicht-topologische Phasen typischerweise durch lokale Dichten charakterisiert sind, werden topologische Phasen, wie die kürzlich experimentell realisierten Meissner-Phase, nur durch lokale Ströme erfasst, was andere Messprotokolle erforderlich macht.

In dieser Arbeit untersuchen wir die Messung lokaler Ströme in ultrakalten atomaren bosonischen Flussleitern mit einem Fokus auf der Diskrepanz zwischen experimentell gemessenen Strömen und numerischen Simulationen, insbesondere im Kontext von Effekten endlicher Temperaturen. Wir untersuchen das von Kessler und Marquardt (2014) vorgeschlagene dynamische Strommessprotokoll durch analytische Herleitungen und numerische Simulationen mit exakter Diagonalisierung (ED) und bewerten die Auswirkungen der zugrundeliegenden Näherungen auf die Messergebnisse. Wir stellen fest, dass nicht-bosonische Statistiken, die sich aus endlich-dimensionalen Hilbert-Räumen ergeben, zu systematischen Fehlern für Grundzustände und thermische Zustände führen, die jedoch im Vergleich zu den Unsicherheiten, die sich aus der Paritätsprojektions-Messung ergeben, untergeordnet sind. Wir identifizieren mögliche Bedingungen für die Gültigkeit des Protokolls ohne Paritätsprojektion, stellen jedoch fest, dass die Isolierung von Effekten endlicher Temperatur aufgrund der vielen anderen Störfaktoren schwierig ist.

Der Vergleich des direkt messbaren Sprossenkorrelators mit Finite-Temperatur-Matrixprodukt-Zustandssimulationen (MPS) für größere Systeme legt nahe, dass der experimentell realisierte Zustand weder ein Grundzustand noch ein thermischer Zustand ist, sondern ein Nichtgleichgewichtszustand. Darüber hinaus entwickeln wir ein robustes numerisches Toolkit für bosonische Flussleitern, das exakte Ergebnisse (kleine Systeme) und Näherungsergebnisse (große Systeme) über einheitliche ED/MPS-Schnittstellen auf der Grundlage bestehender Toolkits ermöglicht.

Unsere Arbeit unterstreicht grundlegende Beschränkungen moderner lokaler Strommessprotokolle in Quantengasmikroskopen und schlägt Wege für zukünftige theoretische und experimentelle Verfeinerungen vor.

Contents

Chapter 1

Introduction

Quantum many-body problems play a central role in condensed matter physics. While the physics of few-particle systems are relatively well-described, emergent phenomena arising from the interaction between many particles can be very complex and rich. Arguably, one of the most interesting yet simple models is the Hubbard model, which was first proposed by Hubbard in 1963 to describe electrons in solids [1].

In this model, neighbouring sites on a lattice are coupled with a hopping term of strength J. In the interacting regime, the particles on each site also couple via a density interaction with strength U. Despite the simplicity of these two parameters, the physics that result from this model have continued to capture the interests of physicists since it was first proposed [2].

Its rise in popular interest, especially in the 2D fermionic case, can generally be attributed to the observation of high-T_c superconducting in LBCO in the 80s [3]. The observed phenomena raised doubts about the applicability of the prevailing theory of superconductivity developed by Bardeen, Cooper, and Schrieffer (BCS) [4, 5, 6], leading to the search for alternative explanations. The Hubbard model was proposed as a possible explanation for the observed phenomena [7].

Generally, the Hubbard model serves as a minimal model for many-body systems, and is often used as a starting point for more complex models. A wide range of phenomena has since been described using this model, especially in higher dimensions. This includes superconductivity, magnetism, and quantum phase transitions. In fact, the model has proved to be especially consequential for the study of high-T_c cuprate superconductors [8]. It exhibits a rich phase diagram, with various phases such as the Mott insulator, superfluid, and charge density wave phases. Yet, exact solutions to the Hubbard model are rare, necessitating numerical explorations [9].

For a system consisting of bosons, such a model is referred to as the Bose-Hubbard model [10]. We may extend the Bose-Hubbard Model model by introducing a(n) (artificial) magnetic field to obtain the Hofstadter-Bose-Hubbard (HBH) model. By having real-valued hopping along one axis and complex-valued hopping along the other axis, an artificial magnetic field can be simulated, allowing this model to incorporate the effects of the Hofstadter Butterfly. [11] Using

this model, rich and complex physics such as those of topological ordered phases (e.g. fractional Chern insulators and quantum Hall effect) have long been predicted [12, 13, 14].

Due to their versatility and controllability, ultracold atoms present an ideal platform for experimentally exploring the physics of these models that have until not too long ago only been theoretically described. A ladder-like quasi-1D lattice of ultracold atoms lends itself as the perfect minimal system where we can realise the HBH model. Such ladder systems, with their artificial magnetic field, have a non-vanishing flux that pierces through each plaquette unit, and are known as *flux ladders*.

Just from this short history of the Hubbard model, we have already seen the beautiful back and forth between experiment and theory, where observations in one inform the research direction of the other, and vice versa. Where experiments cannot immediately be built, or appropriate theoretical descriptions not yet developed, numerics provide a bridge between the two, helping us to understand observations and predict new physics. This thesis stands exactly at the intersection of theory and experiment, with the goal of answering experimental questions not just through numerical simulations, but also by following the theory to its meaningful conclusion.

1.1 Problem Statement

Recently, strongly interacting Meissner states have been realized by Impertro et al. [15] in bosonic flux ladders. These states are generally characterised not by their density distribution but by their local current distribution, which is a direct consequence of the non-trivial topology of the flux ladder. Current measurements are therefore essential in characterising these states. However, since the particle current is not a observable that is directly measurable in a quantum gas microscope, the platform on which the flux ladders were realised, a dynamic protocol [16, 17] has to be used.

In this protocol, the state is first projected onto double-wells, after which a basis rotation in the form of a time-evolution is applied to the system, allowing one, at least in theory, to measure the density difference $\langle \Delta\hat{n} \rangle$ to obtain the local current $\langle \hat{j} \rangle$.

Comparing the local currents measured and the local currents we expect from ground-state simulations, we notice a discrepancy. In this thesis project, we approach the problem from the perspective of numerical simulations to explore whether we can understand this reduced current and the different sources of error. Since we expect factors such as finite-temperatures, particle-loss and other interactions with the environment to be potential sources of errors, it is necessary to move beyond the hard-core boson description of the system (maximum occupation per site $M = 1$), as published in [17], and use soft-core bosons instead ($M > 1$).

Surprisingly, this change to soft-core bosons revealed unexpected subtleties in the current measurement protocol. We therefore systematically carry out a numerical verification of this protocol, explicitly incorporating the non-bosonic commutation relations of soft-core bosons. In contrast to the analysis of particle currents in flux ladders using snapshot-based techniques [18], this project explores specifically the experimental measurement protocol, and the finite-

temperature effects on a specific experimental state. Where it is meaningful, we also explored how features change with increasing temperature.

As one of the main contributions of this project, we also developed a well-tested and robust numerical toolkit for investigating the physics of bosonic flux ladders that produces not just exact results for smaller systems using exact diagonalisation (ED) techniques, but also approximate results for larger system using matrix product state (MPS) techniques.

This thesis is organised as follows: we begin in chapter 2 with exploring the relevant theory. We establish definitions, and derive the experimental current measurement protocol, exploring the theoretical consequences of a finite-dimensional Hilbert space on bosonic commutation relations and its effect on the protocol. In chapter 3, we summarise the relevant experimental details. In chapter 4, we introduce our numerical simulation toolkit, some of the design choices that went into it, and detail the numerical methods used. Finally, in chapter 5, we present results of our numerical simulations, including a numerical verification of the dynamic measurement protocol, and discuss their implications. We conclude with a summary of our results and an outlook on future work in chapter 6.

At the end of the thesis, we answer the following questions:

- Does the dynamic protocol for measuring local currents in flux ladders work as expected?
- Do we have a finite-temperature state in the experiment of Impertro et al. [19]?

Both of which can be answered with a resounding "no"[1].

In fact, we realise that in general, the current measurement protocol is not valid for a system of soft-core bosons where the number of bound states per site M is finite. There are conditions in which this protocol does indeed work, but without better characterisation of other sources of error originating from experimental parameters such as M and the total number of particles in the system N, it is challenging to reach definitive conclusions about the impact of each source of error on the current measurement.

To circumvent limitations of the current measurement protocol, we also analysed the rung correlator, which is a directly measurable quantity. Comparison of experimental data with our large-system finite-temperature MPS simulations provides strong evidence that the experimentally realised state is not a finite-temperature state.

[1] At least we are rather confident of our results based on the data and simulations that we have done. After all, in science there is always a chance that one is wrong.

Chapter 2

Theoretical Background

2.1 Second Quantisation and Fixing Notations

An efficient way of representing quantum states in a quantum many-body system is to employ second quantisation and express the states in Fock space [20], which is a separable Hilbert space that is the direct sum of Hilbert spaces $\mathcal{H}_{(N)}$ of a fixed particle number N over the system:

$$\mathcal{F} = \bigoplus_{N=0}^{\text{Max } N} \mathcal{H}_{(N)} \ . \tag{2.1}$$

Choosing the occupational number basis for $\mathcal{F}$ proves to be particularly convenient. In the case of a bosonic system, the Fock space $\mathcal{F}$ is unbounded in terms of the number of particles on each site, and we can decompose a state as:

$$|\psi\rangle = \sum_{n_1 \ldots n_G} C_{n_1 \ldots n_G} \Big(|n_1\rangle \otimes \cdots \otimes |n_G\rangle \Big) = \sum_{n_1 \ldots n_G} C_{n_1 \ldots n_G} |n_1, \ldots, n_G\rangle \ , \tag{2.2}$$

where each basis state $|n_i\rangle \in \mathcal{H}_i, i \in \mathbb{N}, n_i \in \mathbb{N}_0$, is an occupational number basis state of identical bosons in the local Hilbert space $\mathcal{H}_i$ on each site i, and G is the total number of sites in the many-body system. Generally, the local Hilbert spaces on each site are identical and $\mathcal{H}_i = \mathcal{H}_0$ for all $i \in \mathbb{N}$. [21]

In this representation, the creation and annihilation operators on each site have the following action:

$$\hat{b}_i \, |n_1, \ldots, n_i, \ldots, n_G\rangle = \sqrt{n_i} \, |n_1, \ldots, n_i - 1, \ldots, n_G\rangle \ , \tag{2.3}$$

$$\hat{b}_i^\dagger \, |n_1, \ldots, n_i, \ldots, n_L\rangle = \sqrt{n_i + 1} \, |n_1, \ldots, n_i + 1, \ldots, n_G\rangle \ . \tag{2.4}$$

and fulfil the canonical bosonic commutation relations

$$\left[\hat{b}_i, \hat{b}_j^\dagger\right] = \delta_{i,j} \qquad \text{and} \qquad \left[\hat{b}_i, \hat{b}_j\right] = \left[\hat{b}_i^\dagger, \hat{b}_j^\dagger\right] = 0 \ . \tag{2.5}$$

Consequently, we see that given the vacuum state $|\varnothing\rangle = |0, 0, \ldots\rangle$, where there are no bosons anywhere in the system, we can easily create any Fock state:

$$|n_1, n_2, \ldots\rangle = \left[\prod_{i=1}^{G} \frac{\left(\hat{b}_i^\dagger\right)^{n_i}}{\sqrt{n_i!}}\right] |\varnothing\rangle \ . \tag{2.6}$$

Following the above definitions, the number operator $\hat{n}_i = \hat{b}_i^\dagger \hat{b}_i$ has the following action:

$$\hat{n}_i \, |n_1, \ldots, n_i, \ldots, n_G\rangle = n_i \, |n_1, \ldots, n_i, \ldots, n_G\rangle \ , \tag{2.7}$$

where $i \in \mathbb{N}$ is the index of the site [22].

2.2 Bosonic Flux Ladders

Bosonic flux ladders are excellent platforms to simulate the interaction of charged particles with a magnetic field, exhibiting interesting topological features [24]. Indeed, the defining feature of flux ladders is the manifestation of an external electromagnetic field's influence on quantum particles in a lattice. Such effects first received serious attention after the publication of the Aharonov-Bohm Effect in 1959 [25, 26]. Yet, pioneering work began as early as 1933, when Peierls investigated the dynamics of atoms on a lattice in presence of an external magnetic field $\mathbf{B} = \nabla \times \mathbf{A}$. In his paper, he considered a tight-binding model, where the electrons may only hop between discrete lattice sites. By enforcing local gauge invariance on the system Hamiltonian, he found that the wave function of an electron bound to an ion[1] at site (i, j) gains

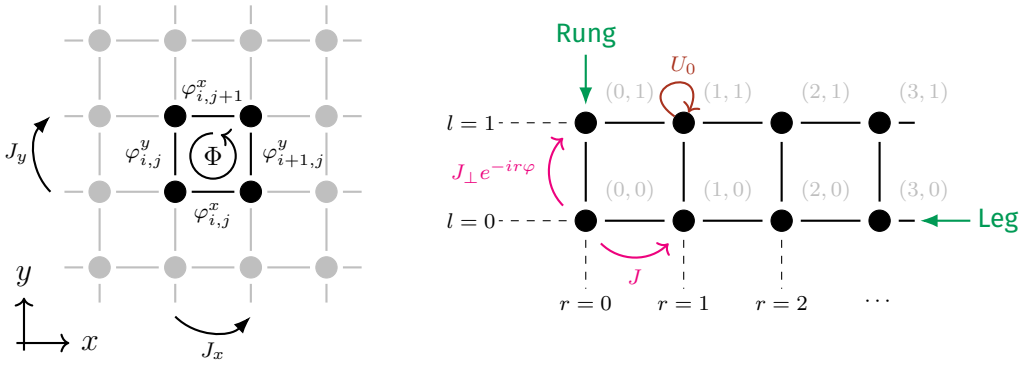

(a) (b)

Figure 2.1: **(a)** Schematic of flux in a square lattice with complex tunneling. Illustration adapted from Figure 2.1 of [23]. **(b)** Sketch of a paradigmatic two-legged flux ladder. The hopping along the legs are real-valued, while the hopping along the rungs are complex-valued. The flux φ is defined as the Peierls phase factor per rung. The flux ladder is defined by the number of rungs R and the number of legs L. The sites are indexed by (r, l), where r is the rung index and l the leg index.

[1] i.e. in an atom

a compensating site-dependent phase, known today as the Peierls phase. [27] This could also be understood as the encoding of the effects of the magnetic field as complex tunnelling amplitudes in our model Hamiltonian. Given some vector potential $\mathbf{A}$ and some original hopping J_{ij}, the Peierls phase shift of a particle with charge q may be written in the form [28]:

$$J_{ij} \to J_{ij} e^{i\varphi_{ij}} \quad \text{, where } \varphi_{ij} = \frac{q}{\hbar} \int_{(i,j)}^{(i+1,j)} \mathbf{A} \cdot d\mathbf{l} \,. \tag{2.8}$$

In the continuum, the Peierls phase $e^{i\varphi_{ij}}$ encodes the Aharonov-Bohm phase. Consequently, one can define the magnetic flux per lattice unit cell in units of the magnetic flux quantum as illustrated in Figure 2.1a [23, Chap. 2]:

$$\Phi = \frac{1}{2\pi} \left(\varphi^x_{i,j} + \varphi^y_{i+1,j} - \varphi^x_{i,j+1} - \varphi^y_{i,j} \right) \,. \tag{2.9}$$

In 1976, Hofstadter published his calculations of the spectrum for electrons on a square lattice in a uniform, perpendicular magnetic field. The calculated spectrum unveiled periodic patterns that are now known as the Hofstadter's butterfly [11], establishing the Hofstadter model. When bosonic particles and on-site interactions are included, this generalizes to the Hofstadter-Bose-Hubbard model:

$$\begin{aligned} \hat{H}_{\text{HBH}} = &- J_x \sum_{i,j} \left(e^{i\varphi^x_{i,j}} \hat{b}^\dagger_{(i+1,j)} \hat{b}_{(i,j)} + \text{h.c.} \right) - J_y \sum_{i,j} \left(e^{i\varphi^y_{i,j}} b^\dagger_{(i,j+1)} \hat{b}_{(i,j)} + \text{h.c.} \right) \\ &+ \frac{U_0}{2} \sum_{i,j} \hat{n}_{(i,j)} \left(\hat{n}_{(i,j)} - 1 \right) \,, \end{aligned} \tag{2.10}$$

where J_x, J_y are the respective tunnelling amplitudes along the x and y direction, $\varphi^\nu_{m,n}$, $\nu = \{ x, y \}$ are Peierls phases satisfying $\Phi = {}^1\!/_{2\pi} \oint_\square \mathbf{A} \cdot d\mathbf{l}$ per plaquette, and U_0 is the on-site interaction.

In the quasi-one-dimensional limit of two legs ($i = 0, 1$), this reduces to the bosonic flux ladder Hamiltonian, providing a minimal framework for studying the interplay between gauge fields, interactions, and dimensionality.

Given the gauge invariant nature of the system Hamiltonian, we may choose the rung-gauge. In this gauge, only the hopping along the rungs are complex-valued, while the hopping along the legs remain real-valued. Paradigmatic two-legged bosonic flux ladders without periodic boundary conditions (as sketched out in Figure 2.1b) can thus be described with the following Hamiltonian [24]:

$$\begin{aligned} \hat{H}_{\text{FL}} = &\overbrace{- J \sum_{r=0}^{R-2} \sum_{l=0}^{L-1} \left(\hat{b}^\dagger_{(r,l)} \hat{b}_{(r+1,l)} + \text{h.c.} \right)}^{\text{(1) Hopping along legs}} \overbrace{- J_\perp \sum_{r=0}^{R-1} \left(e^{-ir\varphi} \cdot \hat{b}^\dagger_{(r,0)} \hat{b}_{(r,1)} + \text{h.c.} \right)}^{\text{(2) Hopping along rungs}} \\ &\underbrace{+ \sum_{r,l} \frac{U_0}{2} \left[\hat{n}_{(r,l)} \left(\hat{n}_{(r,l)} - 1 \right) \right]}_{\text{(3) On-site interaction}} \,. \end{aligned} \tag{2.11}$$

This Hamiltonian may be separated into three different parts. The kinetic terms (1) and (2) describe the hopping along the legs and rungs respectively. Here, J is the tunnelling amplitude along the legs, and $J_\perp$ the tunnelling amplitude along the rungs. In the potential term (3), U_0 describes the strength of the on-site inter-particle repulsion. Here, $L = 2$ is the total number of legs and R is the total number of rungs of the flux ladder. Periodic boundary conditions along the legs can be included by adjusting the limits of the sum over r in (1) and including the interaction between site $(R-1, l)$ and $(0, l)$, with $l \in [0, L) = [0, 1]$.

2.2.1 Ground States Phases

Since a bosonic flux ladder is a system of bosonic particles on a lattice with short-ranged repulsive interactions, we generally expect there to be two phases in which it may exist at zero temperature: a superfluid-phase, and a Mott-insulating phase [30]. The ground state phase is then determined by the relative strength of the inter-site tunnelling amplitude J and the inter-particle repulsion U_0. When J dominates, the system is in a superfluid phase, where bosons are delocalised and can flow freely across the lattice. Conversely, when U_0 dominates, the system enters a Mott-insulating phase where the bosons are localised on individual sites and cannot flow freely. [31]

Analytically, while non-interacting flux ladder model with periodic boundary conditions may be probed rather simply [24, Sec. 2.1.1], intricate analyses are often only possible through more complex theoretical methods, as exemplified in [32] and [33]. Where analytical methods struggle, particularly for non-zero inter-particle interactions U_{ss}, comprehensive numerical studies like [34] help bridge the gap.

Quantum phase transitions beyond these two phases were initially not expected in two-leg bosonic ladders due to the absence of long-range superconducting order. However, should a synthetic magnetic field be introduced to the system, theoretical analysis by Orignac and Giamarchi (2001) demonstrated that the system exhibits phase transitions between Meissner and vortex phases analogous to those found in type-II superconductors [35]. Importantly, both the Meissner and vortex phases can coexist with either underlying ground state: the Meissner phase has been shown to exist on top of both Mott insulators [36, 37] and superfluids [38], while the vortex phase similarly manifests on both Mott insulating and superfluid backgrounds [34]. The seminal work by Orignac and Giamarchi then paved the way for using neutral bosonic systems to emulate orbital physics of charged superconductors through effective gauge fields.

As one of the motivations of this thesis lay in the characterisation of the strongly interacting

Figure 2.2: Local density profile (green shading) and current patterns (red arrows) of the Superfluid biased-ladder (left) and Mott-insulating Meissner (right) phases. Figure adapted from [29, Figure 2(b, c)].

Mott-Meissner phase realized by [19], current measurements are critical. In this phase, the system is in a Mott insulating state with a fixed particle number, while exhibiting Meissner currents induced by the artificial magnetic field, as depicted in Figure 2.2 (right). The characterisation of this phase thus lies mainly in its local currents and not its local density. These currents are localised due to the Mott insulating background, which prevents the bosons from delocalising across the lattice. This results in a unique state where the system exhibits both interaction-induced localisation and chiral currents induced by an artificial magnetic field.

Local Particle Current Operator

The most important observables of interest for this thesis are the local particle current operators $\hat{j}_{\text{leg: }(r,l)}$ and $\hat{j}_{\text{rung: }(r,l)}$. The definition of the current operator for a lattice was initially proposed [39] for fermionic electrons using the position operator $\hat{\mathbf{R}} = \sum_{i,\sigma} R_i \hat{n}_{i,\sigma}$ and the commutator $\left[\hat{\mathbf{R}}, \hat{H}\right]$. This was subsequently disputed [40, 41], before being resolved by the use of the continuity equation [42]. Using the continuity equation in the Heisenberg picture equivalent for bosonic particles

$$\frac{\partial}{\partial t}\hat{n}_{(r,l)[\mathrm{H}]} + \boldsymbol{\nabla} \cdot \hat{\mathbf{J}}_{(r,l)[\mathrm{H}]} = 0 \qquad \text{, with} \qquad \hat{\mathbf{J}}_{(r,l)[\mathrm{H}]} = \left(\hat{j}_{\text{leg: }(r,l)[\mathrm{H}]}, \hat{j}_{\text{rung: }(r,l)[\mathrm{H}]}\right)^T , \tag{2.12}$$

we derive (see Appendix B) the rung and leg current operators [16, 19, 24]. However, it is worth noting that the continuity equation differs slightly from that presented in Impertro et al. [19] and Kessler and Marquardt [16]. Following the sign conventions in Buser [24, Chap. 2.1], we obtain:

$$\hat{j}_{\text{leg: }(r,l)\to(r+1,l)} = iJ\left[\hat{b}^\dagger_{(r,l)}\hat{b}_{(r+1,l)} - \text{h.c.}\right] , \tag{2.13}$$

$$\hat{j}_{\text{rung: }(r,l)\to(r,l+1)} = iJ_\perp\left[e^{-ir\varphi}\cdot\hat{b}^\dagger_{(r,l)}\hat{b}_{(r,l+1)} - \text{h.c.}\right] . \tag{2.14}$$

Significantly, this sign convention is the opposite of what is used in many publications.

2.3 Soft-Core Bosons

In contrast to a system with real bosons, a system with soft-core bosons only allow a finite number of bosons to occupy the same site. As computational resources are limited, this restriction is a natural step in reducing the Hilbert space dimension of the system that we are simulating. Experimentally, this maximum occupation can correspond to the number of bound states on the relevant lattice site. This restriction on the maximum number of bosons per site while seemingly trivial, has non-trivial consequences. Given the action of the bosonic creation and annihilation operators described in Equations 2.3 and 2.4, we can explicitly write down

operators in the Fock basis:

$$\hat{b}_i^\dagger = \sum_{n=0}^{\infty} \sqrt{n+1}\,|n+1\rangle\langle n| \ , \tag{2.15}$$

$$\hat{b}_i = \sum_{n=1}^{\infty} \sqrt{n}\,|n-1\rangle\langle n| = \sum_{n=0}^{\infty} \sqrt{n+1}\,|n\rangle\langle n+1| \ . \tag{2.16}$$

Imposing a maximum occupation M per site, we obtain:

$$\hat{b}_i^\dagger = \sum_{n=0}^{M-1} \sqrt{n+1}\,|n+1\rangle\langle n| \qquad \text{and} \qquad \hat{b}_i = \sum_{n=0}^{M-1} \sqrt{n+1}\,|n\rangle\langle n+1| \ . \tag{2.17}$$

From Equation 2.5, we expect that the following commutation relation to hold true:

$$\left[\hat{b}_i, \hat{b}_i^\dagger\right] \stackrel{!}{=} \hat{\mathbb{1}} \ . \tag{2.18}$$

However, writing out the commutator

$$\hat{b}_i^\dagger \hat{b}_i = \sum_{n=0}^{M-1} (n+1)\,|n+1\rangle\langle n+1| \ , \tag{2.19}$$

$$\hat{b}_i \hat{b}_i^\dagger = \sum_{n=0}^{M-1} (n+1)\,|n\rangle\langle n| \ , \tag{2.20}$$

and calculating the terms explicitly, we realise that that is not the case:

$$\begin{aligned}
\left[\hat{b}_i, \hat{b}_i^\dagger\right] &= \sum_{n=0}^{M-1} (n+1)\,|n\rangle\langle n| - \sum_{n=0}^{M-1} (n+1)\,|n+1\rangle\langle n+1| \\
&= \sum_{n=0}^{M-1} (n+1)\,|n\rangle\langle n| - \sum_{n=1}^{M} n\,|n\rangle\langle n| \\
&= |0\rangle\langle 0| + \sum_{n=1}^{M-1} |n\rangle\langle n| - M\,|M\rangle\langle M| \\
&= \sum_{n=0}^{M-1} |n\rangle\langle n| - M\,|M\rangle\langle M| \equiv \begin{bmatrix} \mathbb{1}_M & 0 \\ 0 & -M \end{bmatrix} \neq \hat{\mathbb{1}}_{M+1} \ .
\end{aligned} \tag{2.21}$$

In the limit of $M \to \infty$ (i.e. in the case of real bosons), we see that $\left[\hat{b}_i, \hat{b}_i^\dagger\right]$ indeed tends to $\hat{\mathbb{1}}$, which is what we expect.

2.4 Measurement of the Local Particle Current in the Fock Basis

For ultracold atoms in optical lattices, it is convenient to measure in the occupational number basis, also known as the Fock basis. This is usually achieved using a quantum gas microscope [17, 43, 44]. For each snapshot, the wave function of our many-body state is projected onto this basis, and we measure the number of atoms occupying each atomic site on the lattice. This choice of basis therefore restricts our directly measurable observables to those that are diagonal in the Fock basis, for example density correlations. Consequently, it is not possible for us to directly access the current densities, which is an off-diagonal observable. [45]

To address this problem and perform spatially resolved measurement of the current between nearest-neighbour lattice sites, Kessler and Marquardt proposed an experimental scheme in 2014 [16]. In this scheme, the many-body state is first projected onto double wells of neighbouring sites, and then allowed to evolve under the double-well Hamiltonian for some time τ such that essentially, the current basis is rotated into the occupational basis. The measured value of the current value may then be obtained from the difference in the occupancy between the two sites.

Given the central role of this protocol in our analysis, it is worth taking a closer look at its details. We will see that subtle assumptions embedded within the method could have significant implications for the measured current values.

Diagonalising the Current Operator Concretely, let us begin by diagonalising the current operators $\hat{j}_{\text{leg}}$ and $\hat{j}_{\text{rung}}$. By defining a generic tunnelling $\tilde{J} = J$ or $J_\perp e^{-ir\varphi}$, we can generalize the current operators (2.13) and (2.14):

$$\hat{j}_{k\to l} = i\left[\tilde{J}\,\hat{b}_k^\dagger \hat{b}_l - \tilde{J}^* \hat{b}_l^\dagger \hat{b}_k\right] . \tag{2.22}$$

Since the operator is quadratic, we can rewrite it in matrix product form to obtain:

$$\hat{j}_{k\to l} = \begin{pmatrix}\hat{b}_k^\dagger & \hat{b}_l^\dagger\end{pmatrix}\begin{pmatrix}0 & i\tilde{J}\\ -i\tilde{J}^* & 0\end{pmatrix}\begin{pmatrix}\hat{b}_k\\ \hat{b}_l\end{pmatrix} \equiv \begin{pmatrix}\hat{b}_k^\dagger & \hat{b}_l^\dagger\end{pmatrix} A \begin{pmatrix}\hat{b}_k\\ \hat{b}_l\end{pmatrix} . \tag{2.23}$$

Diagonalising $A = PDP^{-1}$, we get:

$$\begin{aligned}\hat{j}_{k\to l} &= \begin{pmatrix}\hat{b}_k^\dagger & \hat{b}_l^\dagger\end{pmatrix} PDP^{-1}\begin{pmatrix}\hat{b}_k\\ \hat{b}_l\end{pmatrix}\\ &= \frac{|\tilde{J}|}{2}\begin{pmatrix}-i\frac{\tilde{J}}{|\tilde{J}|}\hat{b}_k^\dagger + \hat{b}_l^\dagger & i\frac{\tilde{J}}{|\tilde{J}|}\hat{b}_k^\dagger + \hat{b}_l^\dagger\end{pmatrix}\begin{pmatrix}-1 & 0\\ 0 & 1\end{pmatrix}\begin{pmatrix}i\frac{\tilde{J}^*}{|\tilde{J}|}\hat{b}_k + \hat{b}_l\\ -i\frac{\tilde{J}^*}{|\tilde{J}|}\hat{b}_k + \hat{b}_l\end{pmatrix} \qquad (2.24)\\ &\equiv \begin{pmatrix}\hat{b}_{\leftarrow}^\dagger & \hat{b}_{\rightarrow}^\dagger\end{pmatrix}\begin{pmatrix}-|\tilde{J}| & 0\\ 0 & |\tilde{J}|\end{pmatrix}\begin{pmatrix}\hat{b}_{\leftarrow}\\ \hat{b}_{\rightarrow}\end{pmatrix} . \qquad (2.25)\end{aligned}$$

Therefore, the current operator may be written as

$$\hat{j}_{k\to l} = |\tilde{J}| \left(\hat{b}^\dagger_{\rightarrow} \hat{b}_{\rightarrow} - \hat{b}^\dagger_{\leftarrow} \hat{b}_{\leftarrow} \right) , \tag{2.26}$$

with

$$\hat{b}_{\rightarrow} = \frac{1}{\sqrt{2}} \left(\hat{b}_l - i \frac{\tilde{J}^*}{|\tilde{J}|} \hat{b}_k \right) \equiv \hat{j}_+ \qquad \text{and} \qquad \hat{b}_{\leftarrow} = \frac{1}{\sqrt{2}} \left(\hat{b}_l + i \frac{\tilde{J}^*}{|\tilde{J}|} \hat{b}_k \right) \equiv \hat{j}_- , \tag{2.27}$$

corresponding to the annihilation operators for right-going ($k \to l$, $\hat{j}_+$) and left-going ($l \to k$, $\hat{j}_-$) particles respectively[2]. In other words, the eigenstates of $\hat{j}_{k\to l}$ are generated by acting $\hat{j}^\dagger_\pm$ on the vacuum state: $\left| j^n_\pm \right\rangle = \left(\hat{j}^\dagger_\pm \right)^n |\varnothing\rangle$, $n \in \mathbb{N}$.

To understand how the eigenstates of the current operator $\hat{j}_{k\to l}$ evolve in time, let us calculate the time evolution of the operators $\hat{j}_\pm = \hat{b}_{\rightarrow/\leftarrow}$ in the Heisenberg picture.

Time Evolution of Current Eigenstates under the Double-Well Hamiltonian Let us first generalise the double well Hamiltonian to obtain:

$$\hat{H}_{\text{DW}} = - \left(\tilde{J}\, \hat{b}^\dagger_k \hat{b}_l + \text{h.c.} \right) + \sum_{m=\{k,l\}} \frac{U_0}{2} \left[\hat{n}_m \left(\hat{n}_m - 1 \right) \right] \equiv \hat{H}_{\text{hop}} + \hat{H}_{\text{int}} , \tag{2.28}$$

where j and k are the indices of the two neighbouring sites in the double well. This double well could be along a rung (to measure $\hat{j}_{\text{rung}}$) or a leg (to measure $\hat{j}_{\text{leg}}$), and is none other than the flux ladder Hamiltonian (2.11) reduced to just two sites.

Inverting the relation (2.27), we can express the original bosonic operators in terms of the right-going and left-going operators:

$$\hat{b}_k = \frac{i\tilde{J}}{\sqrt{2}|\tilde{J}|} \left(\hat{b}_{\rightarrow} - \hat{b}_{\leftarrow} \right) \qquad \text{and} \qquad \hat{b}_l = \frac{1}{\sqrt{2}} \left(\hat{b}_{\rightarrow} + \hat{b}_{\leftarrow} \right) , \tag{2.29}$$

which allows us to rewrite the terms of the Hamiltonian (2.28) in the new basis:

$$\hat{H}_{\text{hop}} = i|\tilde{J}| \left(\hat{b}^\dagger_{\rightarrow} \hat{b}_{\leftarrow} - \hat{b}^\dagger_{\leftarrow} \hat{b}_{\rightarrow} \right) , \tag{2.30}$$

$$\hat{H}_{\text{int}} = \frac{U_0}{4} \left[\left(\hat{n}_{\rightarrow} + \hat{n}_{\leftarrow} \right)^2 + \left(\hat{b}^\dagger_{\rightarrow} \hat{b}_{\leftarrow} + \hat{b}^\dagger_{\leftarrow} \hat{b}_{\rightarrow} \right) - 2 \left(\hat{n}_{\rightarrow} + \hat{n}_{\leftarrow} \right) \right] , \tag{2.31}$$

where $\hat{n}_{\rightarrow} = \hat{b}^\dagger_{\rightarrow} \hat{b}_{\rightarrow}$ and $\hat{n}_{\leftarrow} = \hat{b}^\dagger_{\leftarrow} \hat{b}_{\leftarrow}$ are the number operators for the right-going and left-going particles respectively.

[2] The definitions here differ from those in Kessler and Marquardt [16] due to the sign convention of the current operator. The right-going operator here is associated with the term that has a positive sign in expression (2.26).

We first consider the non-interacting case with just $\hat{H}_{\text{hop}}$ and set $U_0 = 0$. The time evolution of the operators is then given by the Heisenberg equation of motion [46]:

$$\frac{\mathrm{d}}{\mathrm{d}t}\hat{b}_{\rightarrow/\leftarrow} = \frac{i}{\hbar}\left[\hat{H}_{\text{hop}}, \hat{b}_{\rightarrow/\leftarrow}\right] . \tag{2.32}$$

To account for the non-bosonic statistics arising from finite-dimensional soft-core bosons with maximal occupation M, we may rewrite the commutation relation (2.21) as

$$\left[\hat{b}_q, \hat{b}_q^\dagger\right] = \hat{\mathbb{1}} + \hat{\delta}_q \,, \qquad \text{where} \qquad \hat{\delta}_q = -(M+1)\,|M\rangle_q\langle M|_q \;\text{ and }\; q \in \{\,k, l\,\} \,, \tag{2.33}$$

Setting $\hat{\delta}$ to zero would allow us to recover the canonical bosonic commutation relation. In the case of classical bosons, the canonical commutation relations (2.5) hold, and we obtain a set of coupled differential equations:

$$\frac{\mathrm{d}}{\mathrm{d}t}\hat{b}_{\rightarrow/\leftarrow} = -\frac{|\tilde{J}|}{\hbar}\left[\mp\hat{b}_{\leftarrow/\rightarrow}\right] . \tag{2.34}$$

which may be rewritten in the matrix form as:

$$\frac{\mathrm{d}}{\mathrm{d}t}\begin{pmatrix}\hat{b}_\rightarrow \\ \hat{b}_\leftarrow\end{pmatrix} = -\frac{|\tilde{J}|}{\hbar}\begin{pmatrix}0 & -1 \\ 1 & 0\end{pmatrix}\begin{pmatrix}\hat{b}_\rightarrow \\ \hat{b}_\leftarrow\end{pmatrix} . \tag{2.35}$$

Diagonalising the matrix and solving for $\hat{b}_\rightarrow(t)$ and $\hat{b}_\leftarrow(t)$, we get:

$$\hat{b}_\rightarrow(t) = \hat{b}_\leftarrow(0)\sin(\omega t) + \hat{b}_\rightarrow(0)\cos(\omega t) \,, \tag{2.36}$$

$$\hat{b}_\leftarrow(t) = \hat{b}_\leftarrow(0)\cos(\omega t) - \hat{b}_\rightarrow(0)\sin(\omega t) \,, \tag{2.37}$$

with $\omega = |\tilde{J}|/\hbar$.

If $U_0 \neq 0$, the contribution from $\left[\hat{H}_{\text{int}}, \hat{b}_{\rightarrow/\leftarrow}\right]$ also has to be considered. This results in a set of cubic first-order ordinary differential equations, solving which is beyond the scope of this thesis. However, from equation (2.31), we can easily see that the contribution would be non-trivial. Recent work by Stepanenko and Liberto [47] (2024) address current measurements in the presence of finite interactions U_0, and proposed a novel experimental protocol. However, examining this new approach is beyond the scope of this thesis.

Measuring Current We now rewrite our experimentally accessible observables $\hat{n}_k$ and $\hat{n}_l$ in the current basis:

$$\hat{n}_k = \frac{1}{2}\left[\hat{n}_\rightarrow - \hat{b}_\rightarrow^\dagger\hat{b}_\leftarrow - \hat{b}_\leftarrow^\dagger\hat{b}_\rightarrow + \hat{n}_\leftarrow\right] \,, \tag{2.38}$$

$$\hat{n}_l = \frac{1}{2}\left[\hat{n}_\rightarrow + \hat{b}_\rightarrow^\dagger\hat{b}_\leftarrow + \hat{b}_\leftarrow^\dagger\hat{b}_\rightarrow + \hat{n}_\leftarrow\right] . \tag{2.39}$$

We observe that

$$\hat{n}_l + \hat{n}_k = \hat{n}_{\rightarrow} + \hat{n}_{\leftarrow} \ , \text{ and} \tag{2.40}$$

$$\hat{n}_l - \hat{n}_k = \hat{b}^{\dagger}_{\rightarrow}\hat{b}_{\leftarrow} + \hat{b}^{\dagger}_{\leftarrow}\hat{b}_{\rightarrow} \ . \tag{2.41}$$

From equation (2.40), we see that

$$\left[\hat{j}_{k\to l}, \hat{n}_k + \hat{n}_l\right] = 0 \ . \tag{2.42}$$

As such, eigenstates of $\hat{j}_{k\to l}$ are also eigenstates of $(\hat{n}_k + \hat{n}_l)$. This is notably unaffected by the error term $\hat{\delta}$ as the substitution is purely algebraic.

On the other hand, substituting (2.36) and (2.37) into (2.41), we obtain:

$$\begin{aligned} \hat{n}_l(t) - \hat{n}_k(t) &= \sin(2\omega t)\left[\hat{b}^{\dagger}_{\leftarrow}(0)\hat{b}_{\leftarrow}(0) - \hat{b}^{\dagger}_{\rightarrow}(0)\hat{b}_{\rightarrow}(0)\right] \\ &\quad + \cos(2\omega t)\left[\hat{b}^{\dagger}_{\rightarrow}(0)\hat{b}_{\leftarrow}(0) + \hat{b}^{\dagger}_{\leftarrow}(0)\hat{b}_{\rightarrow}(0)\right] && (2.43) \\ &\overset{(2.26)}{=} -\sin(2\omega t)\left[\frac{\hat{j}_{k\to l}(0)}{|\tilde{J}|}\right] + \cos(2\omega t)\left[\hat{n}_l(0) - \hat{n}_k(0)\right] && (2.44) \\ \Rightarrow \hat{n}_k(t) - \hat{n}_l(t) &= \sin(2\omega t)\left[\frac{\hat{j}_{k\to l}(0)}{|\tilde{J}|}\right] + \cos(2\omega t)\left[\hat{n}_k(0) - \hat{n}_l(0)\right] \ . && (2.45) \end{aligned}$$

Indeed, when $\hat{\delta}_k = \hat{\delta}_l = 0$ and if we set $\hbar = 1$, then $\omega = |\tilde{J}|$ and we recover equation (3) of Kessler and Marquardt [16], albeit with an opposite sign corresponding to our sign convention of the current:

$$\hat{n}_k(t) - \hat{n}_l(t) = \sin\Big(2|\tilde{J}|t\Big)\left[\frac{\hat{j}_{k\to l}(0)}{|\tilde{J}|}\right] + \cos\Big(2|\tilde{J}|t\Big)\left[\hat{n}_k(0) - \hat{n}_l(0)\right] \ . \tag{2.46}$$

By choosing some evolution time $|\tilde{J}|\,t = |\tilde{J}|\,\tau = \frac{\pi}{4}(2\alpha+1)$, $\alpha \in \mathbb{N}_0$, the second term vanishes, and we can obtain the current in our double-well from the difference in the occupations between the sites:

$$\boxed{\hat{j}_{k\to l}(t=0) = |\tilde{J}| \ \cdot \left[\, \hat{n}_k(t=\tau) - \hat{n}_l(t=\tau)\,\right]} \tag{2.47}$$

Numerically, we use the following formulation of the above to simulate the experimental measurement protocol of our initial state $|\phi_0\rangle$:

$$\boxed{\Big\langle \hat{j}_{k\to l}(0)\Big\rangle_{\psi_0} = |\tilde{J}| \ \cdot \langle\psi_0|\left[\hat{U}^{\dagger}_{\text{rot}}(\tau)\Big(\hat{n}_k(0) - \hat{n}_l(0)\Big)\hat{U}_{\text{rot}}(\tau)\right]|\psi_0\rangle} \ , \tag{2.48}$$

where $U_{\text{rot}}(\tau) = \exp\Big(-i\hat{H}_{\text{hop}}\tau\Big)$.

Effects of Finite Dimensional Soft Core Bosons In experiments, the number of bound states per site is finite. If we consider a maximal occupation of M per site, then the error term $\hat{\delta}_q = -(M+1)\,|M\rangle_q\langle M|_q$ does not disappear, and the current measurement protocol will not yield the expected results.

Using the modified commutation relations (2.33) and the definitions of $\hat{b}_{\rightarrow/\leftarrow}$ in (2.27), we can calculate the relevant commutators:

$$\left[\hat{b}_{\rightarrow}, \hat{b}^{\dagger}_{\rightarrow}\right] = \left[\hat{b}_{\leftarrow}, \hat{b}^{\dagger}_{\leftarrow}\right] = \hat{\mathbb{1}} + \frac{1}{2}\left(\hat{\delta}_l + \hat{\delta}_k\right) \tag{2.49}$$

$$\left[\hat{b}_{\rightarrow}, \hat{b}^{\dagger}_{\leftarrow}\right] = \left[\hat{b}_{\leftarrow}, \hat{b}^{\dagger}_{\rightarrow}\right] = \frac{1}{2}\left(\hat{\delta}_l - \hat{\delta}_k\right) \tag{2.50}$$

$$\left[\hat{b}_{\rightarrow}, \hat{b}_{\leftarrow}\right] = 0 \tag{2.51}$$

Since $\hat{\delta}_k$ and $\hat{\delta}_l$ act on different sites, $(\hat{\delta}_l - \hat{\delta}_k)$ does not vanish. Using the above commutators, the Heisenberg equation of motion (2.32) then becomes:

$$\frac{\mathrm{d}}{\mathrm{d}t}\hat{b}_{\rightarrow/\leftarrow} = -\frac{|\tilde{J}|}{\hbar}\left[\pm\frac{\hat{\delta}_l - \hat{\delta}_k}{2}\hat{b}_{\rightarrow/\leftarrow} \mp \left(\hat{\mathbb{1}} + \frac{\hat{\delta}_l + \hat{\delta}_k}{2}\right)\hat{b}_{\leftarrow/\rightarrow}\right] . \tag{2.52}$$

Unlike what we had previously in (2.34), this set of coupled differential equations cannot be easily decoupled, and therefore does not have a simple analytical solution, especially given that $[\hat{\delta}_q, \hat{b}_{\rightarrow/\leftarrow}] \neq 0$ for $q \in \{k, l\}$ (For further calculations, see Appendix C). This means that *in general* with finite local dimensions:

$$\boxed{\left[\hat{j}_{\text{finite-dim}}, \left(\hat{n}_k(\tau) - \hat{n}_l(\tau)\right)\right] \neq 0}\,, \tag{2.53}$$

and the measurement protocol **does not work** for *arbitrary* states and local Hilbert space dimensions.

Avoiding the Error Indeed, it is possible to choose the initial state $|\phi_0\rangle$ or the maximum occupation M such that the error term $\hat{\delta}_q = -(M+1)\,|M\rangle_q\langle M|_q$, $q \in \{k, l\}$, does not affect the measurement protocol. If we calculate the expectation value of the commutator (2.33) with respect to our state $|\psi_0\rangle$:

$$\begin{aligned}\langle\psi_0|\left[\hat{b}_q, \hat{b}^{\dagger}_q\right]|\psi_0\rangle = \langle\psi_0|\left(\hat{\mathbb{1}} + \hat{\delta}_q\right)|\psi_0\rangle &= 1 + \langle\psi_0|\hat{\delta}_q|\psi_0\rangle \\ &= 1 - (M+1)\,\langle\psi_0|\left(|M\rangle_q\langle M|_q\right)|\psi_0\rangle\ ,\end{aligned} \tag{2.54}$$

we see that if $\langle M_q|\psi_0\rangle = 0$ for all sites q, then the error term does not affect the measurement protocol. As such, for numerical analyses, we can define a validity observable proxy $\hat{\nu}$:

$$\hat{\nu} = \sum_{(r,l)} |M\rangle_{(r,l)}\langle M|_{(r,l)}\ , \tag{2.55}$$

such that when the expectation value of $\hat{\nu}$ of the state $|\psi_0\rangle$ to be measured is zero ($\langle\hat{\nu}\rangle = 0$), then the current measurement protocol is valid.

Interestingly, for **hard core bosons**, the maximum occupation $M = 1$ means that in the Fock basis, the validity observable $\hat{\nu}$ is non-zero for 3 out of the 4 basis states in the Hilbert space, $|1,0\rangle, |0,1\rangle, |1,1\rangle$. Yet, the experimental protocol works. This is because for $M = 1$, explicit calculations reveal that the first term in equation (2.52) happens to vanish in the subspace $\{|0,0\rangle, |0,1\rangle, |1,0\rangle\}$. Since the subspace spanned by $|0,1\rangle$ and $|1,0\rangle$ is the only subspace where there *can be* a non-zero current, the differential equations decouple for any state with a non-zero current, allowing for its measurement using this protocol. As such, $\langle\hat{\nu}\rangle = 0$ is a *sufficient* but not *necessary* condition for the current measurement protocol to work.

Where necessary, one could potentially calculate all the non-zero matrix-elements of the first term in equation (2.52) for the relevant value(s) of M to find out whether equation (2.52) decouples for the state that we are interested in measuring. However, this calculation is beyond the scope of this thesis.

2.5 Quantum Thermal State

Among the factors contributing to the discrepancy between expected ground-state results and experimental reality, finite temperature effects are a significant and often readily identifiable one. To understand these effects, we require an appropriate definition of a quantum thermal state.

The definition of the quantum thermal state is grounded in statistical mechanics. Although initially developed for classical systems before the establishment of quantum theory [48], the principles of statistical mechanics proved to be remarkably compatible with quantum mechanics and are now fundamental to our understanding of quantum systems.

The thermal state may be defined with respect to different statistical ensembles, depending on the system's constraints. Many modern textbooks do a good job in motivating these definitions. In the following, we present some relevant central definitions as laid out in Cohen-Tannoudji, Diu and Laloe [49], summarising key assumptions. For the derivation of these definition, [49] provides a brief, but formal derivation.

Canonical Ensemble Consider a physical system $\mathcal{S}$ coupled to an environment $\mathcal{E}$, where only the exchange of energy is allowed, and not particles. Given that $\mathcal{E}$ is much larger than $\mathcal{S}$, we can assume that the temperature of the environment $T_\mathcal{E}$ is a constant T, and that the two are in thermal equilibrium ($T_\mathcal{S} = T_\mathcal{E} = T$). This configuration corresponds to that of a canonical ensemble. We may then define the constant thermodynamic β that characterises our system:

$$\beta = \frac{1}{k_B T_\mathcal{E}} = \frac{1}{k_B T_\mathcal{S}} = \frac{1}{k_B T}\,, \tag{2.56}$$

where $k_B = 1.380\,649 \times 10^{-23}\,\mathrm{J\,K^{-1}}$ [50] is the Boltzmann constant.

The density operator of the system $\hat{\rho}_{\mathcal{S}}$, also known as a Gibbs state, is then given by:

$$\hat{\rho}_{\mathcal{S}} = \mathrm{tr}(\hat{\rho}_{\mathcal{S}+\mathcal{E}}) = \frac{1}{Z_C} e^{-\beta \hat{H}_{\mathcal{S}}} \ , \tag{2.57}$$

where $\hat{H}_{\mathcal{S}}$ is the Hamiltonian of the system and Z_C is the canonical partition function defined as:

$$Z_C = \mathrm{tr}\left(e^{-\beta \hat{H}_{\mathcal{S}}}\right) = \sum_{n=0}^{\infty} e^{-\beta E_n} \ . \tag{2.58}$$

Here, E_n are the eigenenergies of the Hamiltonian $\hat{H}_{\mathcal{S}}$.

We note that this state is a mixed state representing a statistical ensemble of pure states, which sits in contrast to a pure quantum state that is a superposition of states.

Grand Canonical Ensemble Should the system $\mathcal{S}$ also be able to exchange particles with the environment $\mathcal{E}$, then we find ourselves in a grand canonical ensemble. We again assume that $\mathcal{E}$ is large and contains a very large number of particles such that the relative change due to the particle exchange is negligible and a chemical potential μ can be defined:

$$\mu = -T \left.\frac{\partial S_{\mathcal{E}}}{\partial N}\right|_{E_{\mathcal{E}}, V_{\mathcal{E}}} \ , \tag{2.59}$$

where $S_{\mathcal{E}}$, $E_{\mathcal{E}}$, $V_{\mathcal{E}}$ are the entropy, energy and volume of the environment respectively, and N the particle number. Compared to the canonical ensemble, in the grand canonical ensemble both the thermodynamic β and the chemical potential μ remain constant, but the number of particles in the system $N_{\mathcal{S}}$ is allowed to fluctuate.

The density operator $\hat{\rho}$ can then be written as:

$$\hat{\rho}_{\mathcal{S}} = \frac{1}{Z_{GC}} e^{-\beta(\hat{H}_{\mathcal{S}} - \mu \hat{N}_{\mathcal{S}})} \qquad \text{with} \qquad Z_{GC} = \mathrm{tr}\left(e^{-\beta(\hat{H}_{\mathcal{S}} - \mu \hat{N}_{\mathcal{S}})}\right) . \tag{2.60}$$

For a system of ultracold atoms in an optical lattice, such as in Impertro et al. [19], there is generally no external particle reservoir after state preparation. As such, we generally expect the thermal state of the isolated lattice system to be described by the canonical ensemble. However, due to e.g. inelastic processes or background gas collisions, particle loss could be present that introduces an effective particle exchange with the environment over experimental timescales. As such, modelling the steady-state distribution with that of a grand canonical ensemble could still be meaningful as it accommodates fluctuating particle number. Crucially, while the system lacks a true thermodynamic reservoir, the chemical potential μ here emerges as an effective parameter defined by the balance between loss rates and the experimental preparation protocol, rather than by equilibrium with a particle bath.

Chapter 3

Experimental Background

The work in this thesis was motivated by and done in collaboration with the experiment of Impertro et al. [19] at LMU Munich in the group of Monika Aidelsburger. As such, in this short chapter, it is useful for us to summarise and recap some parts of the experiment that are most relevant for this thesis, mostly based on the published articles and pre-prints [15, 17, 19]. Full descriptions of the experiment and preparation sequences may be found in the above-mentioned original sources, especially in the supplementary material of [15]. Where parameters are relevant to the numerical simulations, they have been included in their discussion in chapter 5.

3.1 Large Bosonic Flux Ladders

In the experiments of Impertro et al. [19], large bosonic flux ladders were realised using periodically driven many-body systems in a ^{133}Cs quantum gas microscope. The characteristic feature of these bosonic flux ladder is the effective magnetic flux that is threaded through each plaquette in the ladder. To engineer this magnetic flux, a laser-assisted tunnelling scheme based on an additional, superimposed optical running wave was used. By using an effective Floquet description, this time-periodic modulation results in a complex-valued tunnel coupling along the rung direction that induces the artificial magnetic flux [19]. The resulting system has an effective Hamiltonian that is described by the Hofstadter-Bose-Hubbard (HBH) model, as described in equation (2.10).

While flux ladders generally exhibit many different ground state phases (see subsection 2.2), the experiment here puts its focus on the realisation and characterisation of the Meissner phase, which itself is characterised by homogeneous, chiral leg currents and vanishing rung currents [38]. As such, current measurement is key to characterising the phase of the system, and is therefore also the focus of this thesis project.

Generally, realising such a system in the Floquet scheme is rather challenging [51], However, the following parameters seem to be well-controlled in experiments: the couplings J, $J_\perp$, and on-site interaction strength U_0.

3.2 Parity-Projection

Since the readout of the local site occupations is achieved through fluorescence imaging, the near resonant imaging light causes pairs of atoms in the same lattice site to decay into a molecular states. The energy released as a result of this is converted into kinetic energy that kicks the atom pair out of the tightly bound trap. [52]. Generally known as light-assisted collisions in literature [53, 54], such collisions during the imaging process mean that the initial atomic occupation number is projected onto the parity of itself. As such, it is generally only possible to measure either 0 or 1 for the occupation on each site.

In order to take this phenomenon into account in our simulations, we propose the parity-projected number operator $\hat{n}_{\mathrm{pp},i}$, defined in equation (4.1).

3.3 State Preparation

To prepare the states to be measured, a Bose-Einstein condensate of ^{133}Cs atoms is loaded into a two-dimensional optical lattice that comprises a bichromatic superlattice along x, and a monochromatic lattice along y. The system is then isolated into ladders of up to 40-sites.

The state preparation sequence thereafter involves many different steps [15, Supplementary Materials], but what is relevant to this project is that the initial state is a product state with one particle per rung, and coupling between sites are adiabatically turned on (or off) while particles delocalise symmetrically across the rung, and then to ladders or plaquettes, depending on the system that is being prepared. Throughout the sequence, a strong repulsive on-site interaction U_0 is maintained. This means that the preparation of the initial measurement state is generally at or around half-filling, where the total number of particles $N = G/2$, with G being the total number of sites.

Residual coupling do however exist on the order of $J', J'_\perp \sim 1\,\mathrm{Hz} \times h$.

While not immediately relevant to the work done in this thesis, another filling that could be reliably prepared experimentally would be at unity-filling, where $N = G$. [55] This presents a possible way of probing the dynamics as a function of the filling (or rather N), which is an important parameter that has non-trivial consequences for the current measurement protocol, as we will see in chapter 5.

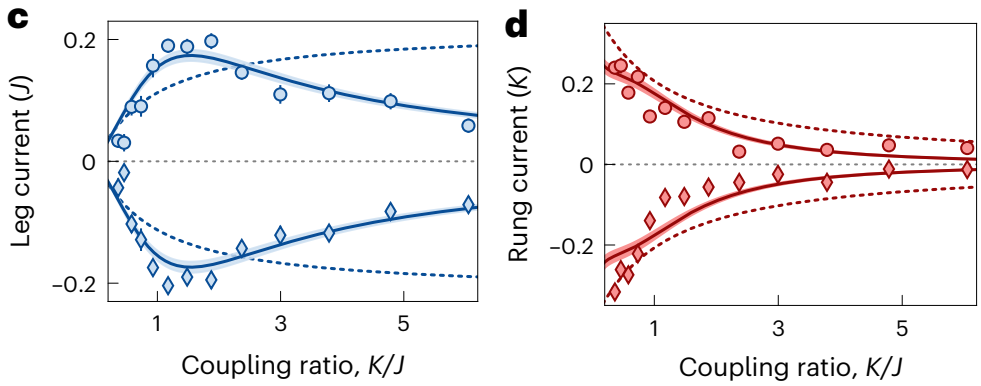

Figure 3.1: Scaling of the leg (c) and rung (d) currents as a function of $J_\perp/J$ (averaged over 140 isolated plaquettes and 200 snapshots per point). The solid line is a fit of an exact diagonalisation (ED) simulation of the ideal currents, with the amplitude as a single free parameter, yielding $0.78(4)$ for the legs and $0.71(4)$ for the rungs; All the numerical simulations take into account the reduced flux in isolated plaquettes of $0.71(2) \times \pi/2$. Figure and caption adapted from [15, Figure 2(c, d), CC BY 4.0].

3.4 Current Measurement Protocol

Once the state is prepared, the local rung and leg currents are measured using the experimental protocol [16] that we have explored in great detail in section 2.4. For the simplified case where there is exactly one boson in the whole double-well, it could also be useful to think of the states $|L\rangle$ and $|R\rangle$, where the boson is the left and the right double well respectively, as a two level system. Then, the density difference $\langle \Delta\hat{n} \rangle$ between the two wells would be given by $\langle \hat{\sigma}_z \rangle$ between the two wells, and the current $\langle \hat{j} \rangle$ is simply given by $J \cdot \langle \hat{\sigma}_y \rangle$ [17], where J is the hopping between the double well, and a $X_{\pi/2}$ rotation will allow us to measure the current as the density difference in the z-axis. In practice, this rotation is realised by a **symmetric** double well with tunnel coupling J.

As we have previously seen, the current measuring protocol may be easily described only when the interactions U_0 is turned off during the rotation. Experimentally, this is achieved by switching the scattering length to approximately zero via a magnetic Feshbach resonance.

In the example of isolated plaquette states, the experimentally measured currents are depicted in Figure 3.1 [15, Figure 2(c, d)], where the experimental data was also fitted to ED simulation data. Here we notice that there was only one free parameter $A < 1$, which meant that the experimentally measured current was less than that expected from ground state calculations. Given how many sources of error could be in play, this free parameter A results in a very simple model that is limited in its utility.

As a result, this thesis project aims to understand the discrepancy in the current measurements and the ideal calculations, and in particular, to explore the effects of finite temperature on the current measurements.

Chapter 4

Numerical Methods

Numerical methods were central to the physics explored in this thesis. This chapter describes thesis-specific implementation details and some theoretical grounding behind the numerics used in our bosonic flux ladder toolkit. The simulations were performed in Python, leveraging backend libraries written in Python and C/C++.

In our simulations in this thesis project, we employed mostly exact diagonalisation (ED) techniques (section 4.4) to simulate smaller systems, which already gave us significant insights into the physics of bosonic flux ladders. However, since the dimension of the total Hilbert space describing a system increases exponentially with the system size, the memory requirements for any calculation using ED techniques also increases exponentially, making them unsuitable for larger systems. For example, for a lattice with G sites and d states per site, the Lanczos algorithm requires vectors of dimension d^G [56]. Conversely, matrix product state (MPS) does not suffer from this limitation and can be used to represent much larger systems efficiently [57]. As such, we employed MPS techniques (section 4.6) to approximate the physics of larger systems.

4.1 Truncation of Hilbert space

Given finite computational resources, we have to restrict the following parameters in our simulated system: (1) size of our two-legged ladder (i.e. the number of rungs R) and (2) the number of local bound states (i.e. the maximum number of bosons per site M). While system sizes of up to $R \times L = 40 \times 2$ have been realised in the corresponding experiment setup associated with this thesis [19], our simulations only reach ladder sizes up to 10×2 and M up to 3 (with MPS). Nevertheless, the simulation results were able to provide valuable insights into the experimental current measurement protocol and provided a good basis for comparison with experimental results.

4.2 Platform-agnostic Definitions

While the two techniques employed (ED vs MPS) are fundamentally different, the processes that we are trying to investigate are the same. Expanding on the second quantisation formulation presented in section 2.1, we see that it is possible for us to work purely with states and operators. Using this framework, we can formulate a platform-agnostic description of our system. These higher-level abstractions in our code makes up the toolkit that facilitates our investigations and comes structurally in the form of Python solver classes:

(a) a parent `FluxLadder` class that defines platform-agnostic methods[1],

(b) a child ED solver class `FluxLadder_ED` that uses the `evos` module [58] as the backend, and

(c) a child MPS solver class `FluxLadder_MPS` that uses the SyTen Toolkit [59, 60] as the backend.

Here, we use `evos` instead other ED packages such as `quspin` because `evos` is already integrated with the SyTen toolkit, and has been specifically developed for open quantum system simulations, a natural extension of the work presented in this thesis.

Such a structure (sometimes also called abstraction [61]) proves to be very beneficial, especially because:

- it enables us to describe what the code should do instead of how it does it,
- it allows us to write high-level scripts separate from the development of the underlying solvers, enabling easy switching between the two solvers,
- it breaks code down into independent, testable components that helps ensures the correctness of the code [62], and
- it improves the readability and maintainability of our code.

Defining parameters of our systems, such as the number of rungs and legs (R, L), maximum occupation per site (M), and the hopping and interaction strengths (J, $J_\perp$, U_0), may be set when instantiating the solver classes. These parameters are then used to construct the operators and states in a platform-agnostic way, allowing us to rapidly test different configurations. These parameters may also be saved as a configuration dictionary in metadata files when data is generated using the solvers.

All operators are implemented as methods of the `FluxLadder_*` classes. For example, to get the local density operator $\hat{n}_{(r,l)}$, we use `ladder.n(r,l)`, where `ladder` is an instance of either `FluxLadder_ED` or `FluxLadder_MPS`. This offers significantly improved readability compared to other packages / modules, for example `evos` (`lattice.sso("op", i)`) and `quspin` (lists of lists as definitions).

[1] A *method* is a named sequence of instructions, also known as a subroutine or a function, that performs a specific task. This differs from the generic definition of a method (= methodology) as a procedure or process for achieving a specific goal.

A unified logging mechanism is also provided through `ladder.log(msg)` and `ladder.warn(msg)`.

In this section, we highlight some of the key considerations and implementation details relevant to our simulations.

Indexing Firstly, both computational methods (ED, MPS) use an underlying 1-dimensional chain of sites of length G to represent the system, which extends to the indexing of operators such as $\hat{b}_i^\dagger$ for the i-th site. To represent a 2-dimensional ladder of sites, we use the notation (r, l), corresponding to the rung and leg indices of the site respectively, Rather than explicitly using the underlying 1-D index in our simulation code, we consistently use the (r, l) notation, and employ an internal mapping method (`get_rl(idx)` and `get_index(r,l)`) to convert to the appropriate underlying site index i. This also allows our code to be more readable and less error-prone.

This mapping method also changes depending on whether we are simulating periodic or open boundary conditions. For more details on this mapping scheme, see Appendix F.

Parity-Projected Measurements As previously discussed in section 3.2, only the parity-projected local occupation is accessible for each measurement. This is generally easy to implement in a snapshot-by-snapshot simulation by taking the modulo of measurement result with respect to 2. However, direct and platform-agnostic access to the measurement results is possible by combining readily-accessible operators and taking the expectation value $\langle \hat{n}_{\text{pp},(r,l)} \rangle = \langle \psi | \hat{n}_{\text{pp},(r,l)} | \psi \rangle$ of a state $|\psi\rangle$. For that, we propose the following expression:

$$\begin{aligned} \hat{n}_{\text{pp},(r,l)} = \hat{n}_{\text{parity-projected, }(r,l)} &= \sum_{n=0} \left[0 \left(|2n\rangle_{(r,l)} \langle 2n|_{(r,l)} \right) + 1 \left(|2n+1\rangle_{(r,l)} \langle 2n+1|_{(r,l)} \right) \right] \\ &= \sum_{n=0} |2n+1\rangle_{(r,l)} \langle 2n+1|_{(r,l)} \ , \end{aligned} \tag{4.1}$$

where $|2n+1\rangle_{(r,l)} \langle 2n+1|_{(r,l)} = P^{(r,l)}_{2n+1}$ are single-site projectors on the odd occupations. Since we have some maximum occupation M, we need only sum to $(2n+1) \leq M$.

To obtain these projectors, we may start from the single-site number operator $\hat{n}_{(r,l)}$ and apply the annihilation/creation operators successively. Using the definitions in Equations 2.3 and 2.4, the projectors $\hat{P}_0^{(r,l)}$ for each lattice site (r, l) may be expressed as:

$$\hat{P}_0^{(r,l)} = |0\rangle_{(r,l)} \langle 0|_{(r,l)} = \frac{\left(\hat{b}_{(r,l)}\right)^M \left(\hat{n}_{(r,l)}\right) \left(\hat{b}^\dagger_{(r,l)}\right)^M}{M \cdot M!} \ , \tag{4.2}$$

and recursively for $m = 1, 2, \ldots, M$:

$$\hat{P}_m^{(r,l)} = \frac{\hat{b}^\dagger_{r,l} \, \hat{P}^{(r,l)}_{m-1} \, \hat{b}_{r,l}}{m} \ . \tag{4.3}$$

For a more detailed derivation, you may refer to Appendix A.

Parameter Scaling For neutral atoms in periodic light fields such as that of an optical lattice, the natural energy scale is the recoil energy $E_R = (\hbar k_L)^2 / 2m_a$ of the trapped atom, where m_a is the mass of the atom and k_L is the wavevector of the lattice standing wave [63]. For a ^{133}Cs trapped with visible light, this energy scale is on the order[2] of 10^{-32} J. Due to how small this energy scale is, calculations in SI units would be numerically unstable. The parameters for simulation were therefore scaled to units of J or $J_\perp$ to increase the accuracy of the results. Where absolute values were necessary, they were calculated using the value of $J_{\perp,\,\text{absolute}}$ that is saved in the solver class. We use $J_{\perp,\,\text{absolute}}$ instead of J_{absolute} because that is the parameter that is held constant in experiment when measuring over a range of $J/J_\perp$ values [64].

4.3 Parameter Sweep

Parameter sweeps were central to many of the results in this thesis. To facilitate the process and improve code reuse, we create the following classes:

`ParameterSweep(runid, variables, *arrays)`, that makes use of `LazyCartesianProduct(*arrays)`

When running jobs on a computing cluster, parameter sweeps are one of the easiest kinds of calculation to parallelise. This is because each group of parameters can be calculated independently of the others. As such, it is usually not necessary for each worker to calculate the full cartesian product of all parameters, which can be very memory intensive. Instead, we can use a lazy cartesian product class that generates only the specific relevant parameter tuple when requested. This allows us to greatly reduce memory usage, allowing more jobs to run in parallel.

The class `ParameterSweep(...)` is an abstract class from which problem-specific parameter sweep classes can be derived. The argument `runid` helps in the identification of the output of the jobs on the cluster, while `variables` are a list of names of the variables that are being swept over. These are saved in the `.metadata` file in the output folder. The argument `*arrays` is simply a list the value-lists corresponding to the data points for each variable.

When creating a new parameter sweep, one need only implement the methods `configure(...)` and `.calculate_one(...)`. The former gets called once per worker, while the latter gets called for each tuple of parameter values. The implemented

`.run(job_idx, total_jobs, cpus_per_job)`

is designed to work with SLURM array job ID's, but works just as well with any other worker indexing method. When called, `.run(...)` automatically calculates the list of parameter tuples that that particular worker is responsible for, and then calls `.calculate_one(...)` for each of these tuples.

An `ExclusiveOpen(...)` class was also implemented as a drop-in replacement for the standard `open()` in Python. Internally, `ExclusiveOpen(...)` uses `fcntl` [65] to ensure that only one

[2] $|k_L| \sim 10^7$, $|\hbar| \sim 10^{-34}$, $|m_a| \sim 10^{-22}$

worker can write to the output file at a time. This ensures output data integrity over the underlying networked filesystem that the computing cluster runs on.

We make use of these tools extensively for our finite-temperature sweeps in sections 5.1 and 5.4.

4.4 Exact Diagonalisation (ED)

In ED calculations, we map the full Hilbert space $\mathcal{H}_{\text{lattice}}$ of G sites to the complex space $\mathbb{C}^{d^G}$, where d is the dimension of the local Hilbert space on each site. Since we work in the Fock basis, d is given by $M+1$, where M is the maximum occupation per site. As such, states are represented by vectors $\in \mathbb{C}^{(M+1)^G}$, and operators are represented by matrices $\in \mathbb{C}^{(M+1)^G \times (M+1)^G}$. Global states and operators can then be created through a tensor product of single site states and operators, as described in section 2.1.

In `FluxLadder_ED`, effort was made to ensure that functions such as

- `ladder.get_expectation(state, operator)`, or
- `ladder.get_fidelity(state1, state2)`

are compatible with both state vectors $|\psi\rangle$ and density matrices $\hat{\rho}$ at the same time to avoid unnecessary conversion steps.

There are generally two ways we can represent these states and operators computationally, either using:

- dense arrays (`numpy.ndarray`), where every single element is stored, or
- sparse arrays (`scipy.sparse.spmatrix`). where only the non-zero elements are stored.

Since a bosonic lattice class using dense arrays has already been implemented in the underlying `evos` module, we create an additional `BosonicLatticeSparse` class that uses sparse arrays. Both of these classes expose the identity operator $\hat{I}$, the creation and annihilation operators, $\hat{b}_i^\dagger$ and $\hat{b}_i$, the local density operator $\hat{n}_i$, and the vacuum state $|\varnothing\rangle$.

Due to how often we require a specific Fock state, and to respect the abstraction of code, we expand both above-mentioned classes with a `get_fock_state(occupations)` method that returns the array representation of a certain Fock state. This is done efficiently in ED by treating the `occupation`-array $\left\{ n_i \in [0, M] \right\}_{i\in[0,G]}$ as a base-$(M+1)$ number, and converting this number string to a decimal integer corresponding to the index of the non-zero element in the state array[3]. This creates a state array that is equivalent to that generated using definition (2.6).

While sparse arrays are generally more memory efficient and offer much faster computation for the operations that we are interested in, the diagonalisation of sparse matrices using ARPACK routines [66, 67] does not yield the full spectrum. This is because its Lanczos/Arnoldi eigensolver

[3] For example, the four-site Fock state $|1,2,2,0\rangle$ with $M=3$ is treated as $(1220)_4 = (104)_{10}$, and the state $|1,2,2,0\rangle$ is represented by a state array where the 104^{th} (0-indexed) array element is the only element set to 1.

excels at finding a limited number of eigenvalues at either end of the spectrum, and not all eigenvalues. This makes the use of dense matrices and LAPACK routines [68] still very relevant, especially in the analysis in sections 2.4 and 5.2.

4.4.1 Projection to a Fixed-N Symmetry Subspace

Since the flux ladder Hamiltonian that we are investigating is particle-conserving, we can significantly reduce the size of the Hilbert space by only working in a fixed-N symmetry subspace and expressing our operators and states only using a basis of Fock states that have exactly N particles.

At the same time, since the measurement protocol described in section 2.4 necessitates the projection of our system onto double-wells, we have to be able to take a partial trace over all the sites that are not the particular two-site double-well that we are interested in. Crucially, this partial trace inherently disrupts the global particle-number symmetry and the reduced density matrix for the double-well may well exist in a superposition of different particle-number sectors, even when the full-system resides in a fixed-N subspace.

As a result, while it is desirable to calculate the ground state or the thermal state in some fixed-N symmetry subspace, it is necessary to do our numerical analysis involving the double-well projection and experimental current measurement protocol in the full Hilbert space. In other words, it would be desirable for our states and operators to be cross-compatible between the fixed-N symmetry subspace and the full Hilbert space.

To achieve this, we implement the Python function decorator[4] `@allow_subspace_N`, which was applied to all operators that conserve particle number (i.e. $[\hat{O}, \hat{N}] = 0$).

Using the methods `ladder.fix_N_to(N)` and `ladder.unfix_N()`, we can turn on and off whether we use the full *(symmetry disabled)* or the reduced Hilbert space *(symmetry enabled)*. The decorator `@allow_subspace_N` checks every time when a method is called whether the symmetry is enabled, and if it is, return the reduced operator:

$$\hat{O}_{\text{sym}} = \mathbf{T}\hat{O}_{\text{full}}\mathbf{T}^{\dagger} \,, \tag{4.4}$$

where $\mathbf{T}$ is the transformation matrix created from the basis states of the fixed-N symmetry subspace. Using a simple nesting depth counter, `@allow_subspace_N` prevents multiple applications of the transformation in the case of nested calls of decorated methods. Due to the way the code is structured, any secondary quantities (e.g. the thermal state density operator) will also automatically be in the fixed-N symmetry subspace if the symmetry is enabled.

The details on how we generate the full set of N-particle basis states for the matrix $\mathbf{T}$ can be found in Appendix E. We also cache $\mathbf{T}$ in a dictionary with N as the key so that a recalculation is not necessary every time.

[4] In this case, we use a function decorator [69] to "wrap" some methods of `FluxLadder_ED` and modify the output of the method.

To easily convert states between the symmetry-N subspace and the full Hilbert space, we use the methods:

- `ladder._trafo(density_op, to_big)`, and
- `ladder._trafo_state(state_vec, to_big)` ,

where `ladder` is an instance of `FluxLadder_ED`. These methods are especially essential as the partial trace should only be taken in the full Hilbert space.

Leveraging on this symmetry, we were able to run ED calculations for system sizes up to (6×2) sites and a maximum occupation of $M = 3$ bosons, which is equivalent to a system with 24 spins.

4.5 The Current Operator and Numerical Verification of Experimental Protocol

One of the central analysis of this thesis is the numerical verification of the current measurement protocol proposed by Kessler and Marquardt [16]. In this section, we document the numerical methods used for the analysis, the results of which will be discussed in section 5.2.

In `FluxLadder_ED`, we implement three different kinds of relevant current operators (listed in Table 4.1), including those based on equation (2.48), but with the double-well Hamiltonian $\hat{H}_{\mathrm{DW}}$ replacing $\hat{H}_{\mathrm{hop}}$ to allow for a finite U_0 during rotation. By setting `turn_off_onsite = True`, we recover $\hat{H}_{\mathrm{hop}}$. Here, we generate $\hat{H}_{\mathrm{DW}}$ by simply building the original system flux ladder Hamiltonian $\hat{H}_{\mathrm{FL}}$, but only for the relevant two sites. For the parity-projected measurements, we use the definition of $\hat{n}_{\mathrm{pp},(r,l)}$ in equation (4.1).

By implementing the current measuring protocol as an operator, we can obtain the experimentally measured current values simply by calculating the expectation value of the relevant operator for a given state $|\psi\rangle$, greatly simplifying and improving the readability of our code.

For our numerical analysis of the current measurement protocol for $\hat{j}_{\mathrm{leg};\,(0,0)\to(1,0)}$ in subsection 5.2.1, we first characterise the time evolution of the eigenstates of the current operator in a double well. Since the operators $\hat{j}_{\mathrm{leg}}$ and $\hat{j}_{\mathrm{rung}}$ differ only by a complex phase, we focus our analysis exclusively on the leg current operator. We diagonalise the operator $\hat{j}_{\mathrm{leg};\,0\to1}$ using its dense matrix representation to obtain the full spectrum of eigenvalues j and eigenvectors $\{|j_m\rangle\}_m$. Eigenvalues within a numerical tolerance[5] of $\sim 10^{-8}$ are grouped. Eigenvalues are averaged within each group. The time evolution operator is then applied to each eigenstate for times $t \in [0, \pi]$ to obtain the results depicted in Figures 5.3 and 5.4, and Appendix D.

In a perfect experimental measurement, we can compute the outcome probabilities using the Born rule. In particular, we can use this to construct the outcome distribution for our analysis

[5] Based on double-precision floating-point precision [70] and operator properties

Python	Operator
`j_leg(r,l)`	$\hat{j}_{\text{leg: }(r,l)\to(r+1,l)}$
`j_rung(r)`	$\hat{j}_{\text{rung: }(r,0)\to(r,1)}$
`j_leg_rot(r,l, turn_off_onsite=False)`	$J \cdot \hat{U}_{\text{rot}}^{\dagger} \left(\hat{n}_{(r,l)} - \hat{n}_{(r+1,l)}\right) \hat{U}_{\text{rot}}$
`j_rung_rot(r, turn_off_onsite=False)`	$J_{\perp} \cdot \hat{U}_{\text{rot}}^{\dagger} \left(\hat{n}_{(r,0)} - \hat{n}_{(r,1)}\right) \hat{U}_{\text{rot}}$
`j_leg_rot_parity_projected(r,l, turn_off_onsite=False)`	$J \cdot \hat{U}_{\text{rot}}^{\dagger} \left(\hat{n}_{\text{pp},(r,l)} - \hat{n}_{\text{pp},(r+1,l)}\right) \hat{U}_{\text{rot}}$
`j_rung_rot_parity_projected(r, turn_off_onsite=False)`	$J_{\perp} \cdot \hat{U}_{\text{rot}}^{\dagger} \left(\hat{n}_{\text{pp},(r,0)} - \hat{n}_{\text{pp},(r,1)}\right) \hat{U}_{\text{rot}}$

Table 4.1: Overview of the current operators implemented in `FluxLadder_ED`. The operators are defined in the Fock basis, where $\hat{n}_{(r,l)}$ is the local occupation operator at site (r,l), and $\hat{U}_{\text{rot}} = \exp(-i\hat{H}_{\text{DW}}\tau)$ is the rotation operator based on equation (2.48) and the current measurement protocol [16], however with the possibility of a finite U_0. The last two operators are parity-projected versions of the middle two operators.

in subsection 5.2.2 at three stages of the current measurement protocol: (i) pre-rotation, (ii) post-unitary-rotation, and (iii) post-parity-projection.

For stage (i), we first construct the reduced density matrix $\hat{\rho}_{\text{DW}}$ for the double well $(0,0)$ and $(1,0)$ through a partial trace of an initial plaquette state $|\psi\rangle$. Then, the probability[6] $\langle j_m|\hat{\rho}_{\text{DW}}|j_m\rangle$ for measuring each eigenstate $|j_m\rangle$ is assigned to a bin according to its associated eigenvalue j to create a histogram over all eigenvalues. This yields the theoretical distribution of $\hat{j}_{\text{leg: }(0,0)\to(1,0)}$ measurement outcomes with respect to the state $|\psi\rangle$.

Next, to simulate post-rotation measurements for stages (ii) - (iii), i.e. for the observable $(\hat{n}_{(\text{pp},)(0,0)} - \hat{n}_{(\text{pp},)1,0})$, we instead use Fock states and the corresponding eigenvalue for each Fock state to build the outcome probability distribution. To illustrate this, we may use the example of the state $|2,0\rangle$. The probability $\langle 2,0|\hat{\rho}_{\text{DW}}|2,0\rangle$ to measure the state $|2,0\rangle$ before parity-projection will be associated with the eigenvalue $(n_{(0,0)} - n_{(1,0)}) = (2-0) = 2$ and after parity-projection with the eigenvalue $(n_{\text{pp},(0,0)} - n_{\text{pp},(1,0)}) = (0-0) = 0$.

Just like with the current operators in Table 4.1, the double-well Hamiltonian $\hat{H}_{\text{DW}}$ used for the rotation in this part of the analysis can have its interaction term turned on or off.

Further details about the numerical verification of the experimental current measurement protocol are described in section 5.2.

[6] In this case, we use `ladder.get_fidelity(DW_state, eigenstate)` to calculate the probability.

4.6 Matrix Product States (MPS)

A powerful alternative to using ED techniques is to represent our quantum state as matrix product states (MPSs). The popular use of MPS to describe quantum states is generally associated with the rise in popularity of the density matrix renormalisation group (DMRG) algorithm, a variational technique used to find ground states of quantum systems [71, 72]. In this section, we present the most relevant MPS concepts and definitions. A good resource that provides a thorough introduction to MPS and its associated techniques is the review article by Schollwöck [73], on which we also base most of this section.

An arbitrary pure quantum state on a lattice of G sites has the form:

$$|\psi\rangle = \sum_{n_i} C_{n_1,\dots,n_G} |n_1, \cdots, n_G\rangle \ , \tag{4.5}$$

where $|n_1, \cdots, n_G\rangle$ is a Fock state with occupations n_i at each site i, and $C_{n_1,\cdots,n_G}$ is the corresponding coefficient. Treating the coefficient $C_{n_1,\cdots,n_G}$ as a rank-G tensor, we may use singular value decomposition (SVD) to factorise it into a product of matrices:

$$C_{n_1,\cdots,n_G} = \sum_{\alpha_1,\dots,\alpha_{G-1}} A^{(1)}_{n_1,\alpha_1} A^{(2)}_{\alpha_1,n_2,\alpha_2} \cdots A^{(G)}_{\alpha_{G-1},n_G} \ , \tag{4.6}$$

which allows us to represent the quantum state (4.5) exactly as:

$$|\psi\rangle = \sum_{n_1,\dots,n_G} A^{(1)} A^{(2)} \cdots A^{(G)} |n_1, \cdots, n_G\rangle \ , \tag{4.7}$$

where the maximum dimension of the matrices $A^{(i)}$ is called the *bond dimension* of the MPS. Operators may be defined in a similar fashion to form matrix product operators (MPOs).

For the results presented in this thesis, we worked only with the high-level functions and representations exposed by the SyTen toolkit [59, 60] through its Python library `pyten`. As such, further implementation details within the tensor network toolkit are not presented.

4.6.1 State Purification and Thermal State

Since thermal states are mixed states (see section 2.5), and MPS can only represent pure states, we use state purification to do finite-temperature calculations [74]. The idea of purification is to represent a mixed state in a physical space P as the partial trace of a pure state in an extended Hilbert space PQ, where Q is an auxiliary space:

$$\hat{\rho}_P = \sum_\alpha s_\alpha^2 |\alpha\rangle_P \langle\alpha|_P \overset{!}{=} \mathrm{Tr}_Q \left(|\psi\rangle\langle\psi|\right) \ \rightarrow \ |\psi\rangle = \sum_\alpha s_\alpha |\alpha\rangle_P |\alpha\rangle_Q \ , \tag{4.8}$$

This auxiliary space Q can simply be a copy of the physical state space P. In practical terms, that means doubling the number of sites in our lattice, with computationally neighbouring sites alternating between physical and auxiliary spaces. For a system with G sites physically

and $2G$ sites computationally, this means that site $2i$ is physical, and site $2i+1$ is auxiliary, for $i \in [0, G)$. As such, we extend our method `ladder.get_index(r, l, auxiliary=False)` to be able to take into account whether we want the auxiliary or the physical site.

Given that the Hamiltonian of our flux ladder system conserves the number of particles, we may leverage on the $U(1)$ symmetry [75] by using `pyten.mp.lat.u1u1.genBosonBosonLattice` to generate a lattice with a $U(1)$ symmetry over the physical sites and another $U(1)$ symmetry over the auxiliary sites.

To calculate the thermal state, we rewrite equation (2.57) as:

$$\hat{\rho}_\beta = \frac{1}{Z_C(\beta)} e^{-\beta \hat{H}} = \frac{1}{Z_C} e^{-\frac{\beta}{2}\hat{H}} \hat{\mathbb{1}} e^{-\frac{\beta}{2}\hat{H}} \,, \tag{4.9}$$

At this point, we recognise that (a) $\exp(\mathbf{0}) = \hat{\mathbb{1}}$ and (b) at infinite temperature, $\beta = 0$ and the infinite temperature state is given by:

$$\hat{\rho}_0 = \frac{1}{Z_C(0)} e^{\mathbf{0}} \;\Rightarrow\; \hat{\mathbb{1}} = Z_C(0)\rho(0) \,, \tag{4.10}$$

which allows us to rewrite equation (4.9) under the assumption that we know the purification of the infinite temperature state $|\Psi_0\rangle$:

$$\begin{aligned} \hat{\rho}_\beta &= \frac{1}{Z_C(\beta)} \left[e^{-\frac{\beta}{2}\hat{H}} \left(Z_C(0)\hat{\rho}_0 \right) e^{-\frac{\beta}{2}\hat{H}} \right] \\ &= \frac{Z_C(0)}{Z_C(\beta)} \left[e^{-\frac{\beta}{2}\hat{H}} \left(\mathrm{Tr}_Q \left(|\Psi_0\rangle\langle\Psi_0| \right) \right) e^{-\frac{\beta}{2}\hat{H}} \right] . \end{aligned} \tag{4.11}$$

Since $\hat{H}$ only acts on the physical space P, we have:

$$\hat{\rho}_\beta = \frac{Z_C(0)}{Z_C(\beta)} \mathrm{Tr}_Q \left[\left(e^{-\frac{\beta}{2}\hat{H}} \otimes \hat{\mathbb{1}}_Q \right) |\Psi_0\rangle\langle\Psi_0| \left(e^{-\frac{\beta}{2}\hat{H}} \otimes \hat{\mathbb{1}}_Q \right) \right] \,, \tag{4.12}$$

which means that we can calculate the thermal state by carrying out imaginary time evolution of the infinite temperature state $\hat{\rho}_0$ in the extended Hilbert space PQ from $t = 0$ to $t = -i\beta/2$. Since $Z_C(0)/Z_C(\beta)$ is just a normalisation factor, we can simply normalise our state after the imaginary time evolution to obtain the normalised thermal state $\hat{\rho}_\beta$.

To obtain the purified infinite temperature state, we may treat it as a ladder of sites, with each rung connecting a physical and an auxiliary site. It is useful to then factorise the physical infinite temperature mixed state $\hat{\rho}_0$ as a chain of maximally mixed states in the physical space P:

$$\hat{\rho}_0 = \frac{1}{d^G}\hat{\mathbb{1}} = \left(\frac{1}{d}\hat{\mathbb{1}} \right)^{\otimes G} = \left(\frac{1}{d} \sum_\alpha |\alpha\rangle_P \langle\alpha|_P \right)^{\otimes G} \,, \tag{4.13}$$

where d is the local dimension of each site.

As such, the purified infinite temperature state $|\Psi_0\rangle$ can be obtained by simply purifying each physical site locally over it and its auxiliary site to obtain a chain of maximally entangled pairs of physical and auxiliary sites in the space PQ:

$$|\Psi_0\rangle = \left(\frac{1}{\sqrt{d}}\sum_{\alpha}|\alpha\rangle_P|\alpha\rangle_Q\right)^{\otimes G} \tag{4.14}$$

To make use of the $U(1)$ symmetry and create this maximally entangled state in a particular N-particle symmetry sector, we may define the following operator [76, Equations S54 and S55]:

$$\hat{C}_{\text{tot}} = \sum_{i=0}^{G-1}\hat{b}^\dagger_{i,P}\hat{b}^\dagger_{i,Q} \tag{4.15}$$

which when applied N times to the vacuum state $|\varnothing\rangle$, creates a chain of maximally entangled states with a total particle number of N:

$$\left|\Psi_{0,N}\right\rangle = \frac{1}{N!}\hat{C}^N_{\text{tot}}|\varnothing\rangle = \frac{1}{N!}\left(\sum_{i=0}^{G-1}\hat{b}^\dagger_{i,P}\hat{b}^\dagger_{i,Q}\right)^N|\varnothing\rangle \ . \tag{4.16}$$

Once we have the infinite temperature state $\left|\Psi_{0,N}\right\rangle$, we can then carry out imaginary time evolution to obtain the thermal state $\hat{\rho}_\beta$ as described above.

Many different techniques have been developed in the last two decades to perform time-evolution on MPSs, a overview of which may be found in [77]. In contrast to trotter-based methods such as the time-evolving block-decimation (TEBD) [78, 79], time-dependent variational principle (TDVP) [80, 81, 82] uses the variational principle to obtain time-evolved states, which allows us to preserve symmetries during the time-evolution. As such, to obtain the thermal state $\hat{\rho}_\beta$, we choose to use TDVP, in particular single-site time-dependent variational principle (1TDVP), to perform the imaginary time-evolution of the infinite temperature state $\left|\Psi_{0,N}\right\rangle$. Extensions to 1TDVP using local and global subspace expansion (LSE, GSE) [83, Appendix D] were also tested to see which one performs better for our system.

Chapter 5

Results and Discussions

Can the discrepancies between the local current that is experimentally measured and the local current that we expect from theoretical calculations be explained by finite temperature effects? In this chapter, we present and discuss the results that we have obtained from our numerical simulations and analyses that were done as we sought to answer this question. In particular, we examined the results measured by Impertro et al. [19] based on the experimental protocol proposed by Kessler and Marquardt [16]. In the end, we are going to answer the following questions:

- Does the dynamic protocol for measuring local currents in flux ladders work as expected?
- Do we have a finite-temperature state in the experiment of Impertro et al. [19]?

For all our analyses and simulations, we use the notation $(r, l) \equiv (\text{rung index}, \text{leg index})$, and denote the system size with R and L for the number of rungs and legs respectively. Indices start at zero and end at $R - 1$ or $L - 1$. Given the plaquette's significance as the smallest possible flux ladder, most of our analyses and simulations were based on a system of a single plaquette. Importantly, this focus has revealed intricacies of the local current measurement protocol. While larger systems may exhibit emergent phenomena, the insights gained at the single-plaquette level are fundamental and can strongly inform our understanding of the basic mechanisms expected to persist in larger flux ladders.

All in all, we could provide ultracold atomic experiments, particularly those that realize bosonic flux ladders, with a better understanding for their current measuring protocol. A central technical contribution of this thesis project is a well-tested toolkit for investigating the physics of bosonic flux ladders that produces not just exact results for smaller systems using exact diagonalisation (ED) techniques, but also approximate results for larger system using matrix product state (MPS) techniques.

5.1 Finite Temperature Parameter Sweep of Local Current Operators in a Plaquette

If the discrepancies between the measured current and the theoretically predicted current can be fully explained by finite temperature effects, it should then be possible to assign some temperature to the system state. As such, to get a first order approximation of the temperature range that we should be looking at, a parameter sweep over temperature T and chemical potential μ was performed using ED techniques. For the parameter sweep, we measure the expectation value of the current operator, $\langle \hat{j}_{\text{leg: }(0,0)\to(1,0)} \rangle$ for some $T \in \left[10^{-10}\,\text{K}, 10^{-6}\,\text{K}\right]$, and $\mu \in [-2\pi, 2\pi] \times 100\,\text{Hz}$. Here, we describe our system using the grand canonical ensemble, where equation (2.60) defines our system's density operator. In our simulations, We have open boundary conditions and use the experimentally relevant values $\varphi = 0.75 \cdot \pi/2$ and $U_0 = 9J_\perp$. We keep $J_\perp/h = 1.4 \times 10^2\,\text{Hz}$ constant, analogous to experiments ($J_\perp/h = (1.40 \pm 0.01) \times 10^2\,\text{Hz}$) [64], and scale J accordingly. For the local Hilbert space dimension, we opted for a maximal occupation of three bosons per site, which was the largest local Hilbert space dimension for which the calculations finished within a reasonable amount of time, especially for testing purposes.

At this point of the project, we were working under the assumption that the experimental measurement protocol described in [17] works as expected, and any errors resulting from the protocol (and parity projection) are negligible. As such, the parameter sweep was done by directly taking the expectation of the current operator $\hat{j}_{\text{leg: }(0,0)\to(1,0)}$. We then overlay the experimentally measured values [64] on our simulation plots, with the error given by the standard error of the mean (s.e.m.). These plots are depicted in Figures 5.1 and 5.2.

The most prominent feature emerging from our parameter sweeps is the appearance of characteristic cones at lower temperatures. At very low temperatures, the sharp transition along the μ axis is likely linked to the discrete nature of the conductance in quantum channels [84]. Specifically, the cone structure manifests at transitions where the incremental increase in the chemical potential μ drives the addition (or removal) of a single particle to the system. As the temperature increases, thermal disorder dominates and the cones broaden and fade into a continuum.

From the plots, we see that the range of the relevant absolute temperatures (labelled green in the figure) actually varies rather significantly between the different $J_\perp/J$ values, ranging from $T = 5.7 \times 10^{-8}\,\text{K}$ ($J_\perp/J = 0.407$) to $T \leq 10^{-10}\,\text{K}$ ($J_\perp/J = 1.46, 1.88$). As the hopping amplitude $J_\perp/J$ increases, this band gets progressively colder. Normalising the temperature with respect to J ($k_B T/J$), we observe that the relevant temperatures are generally around $k_B T/J \sim 1$. Beyond $J_\perp/J \geq 2.43$, the simulation no longer captures any area that could be experimentally relevant.

All in all, we observe that the experimentally realised state lies somewhere in the low temperature regime, around the energy scale of the hopping amplitude J, which was expected. However, we realised that given the way the state is prepared (see chapter 3), μ might not really be meaningfully defined. As such, instead of fitting for some μ, it could be useful to fix the total number of particles N in our system instead, which is experimentally often at half-filling (i.e. $N = (R \times L)/2$).

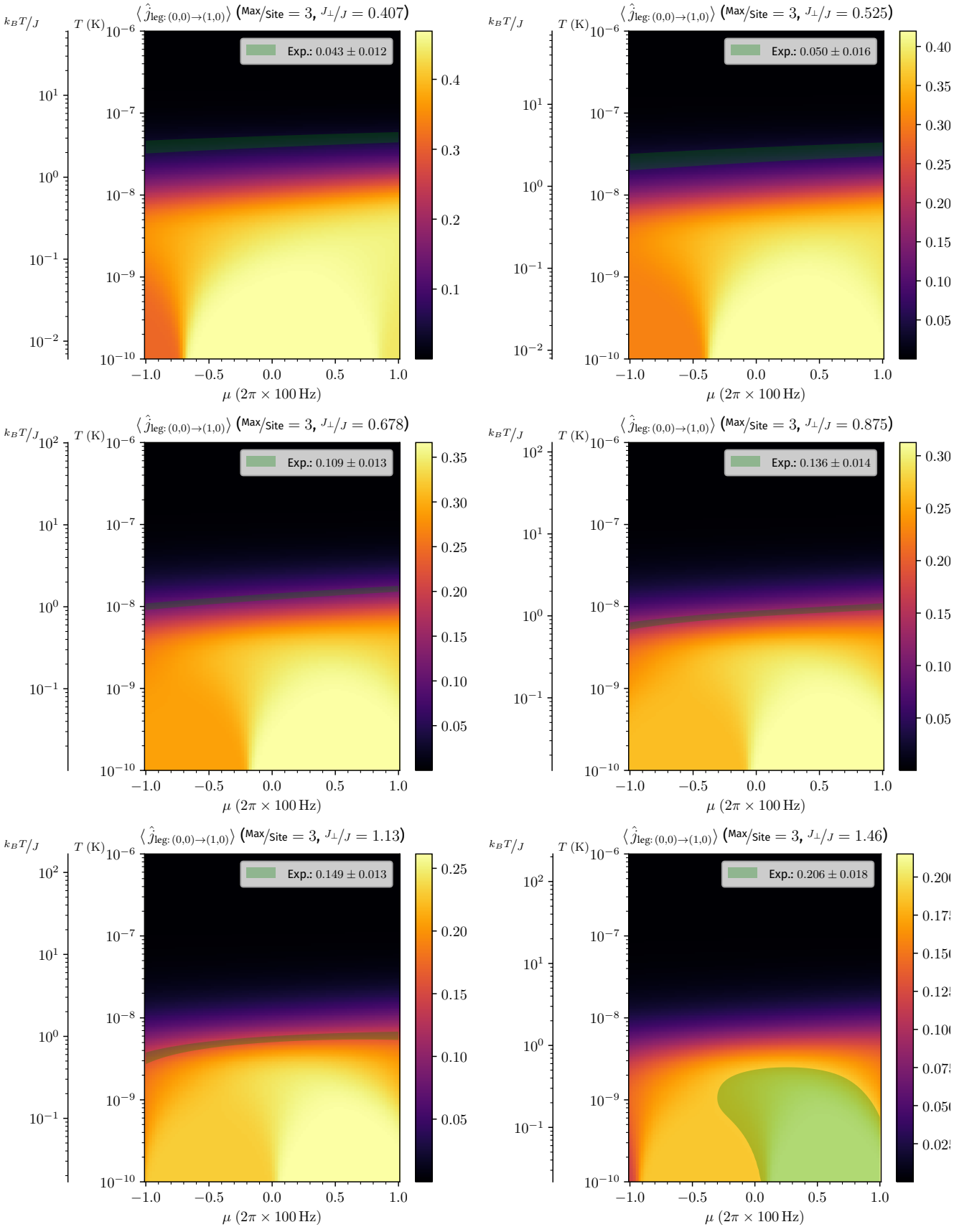

Figure 5.1: Parameter sweep over T and μ for the local current operator $\hat{j}_{\text{leg: }(0,0)\to(1,0)}$ in a plaquette (direct measurement, no parity projection, $U_0 = 9J_\perp$, open boundaries) for the experimental values $J_\perp/J = 0.407$ to $J_\perp/J = 1.46$. The green overlay represents the experimental measurement results [64]. Relevant absolute temperature range varies greatly between different $J_\perp/J$ values.

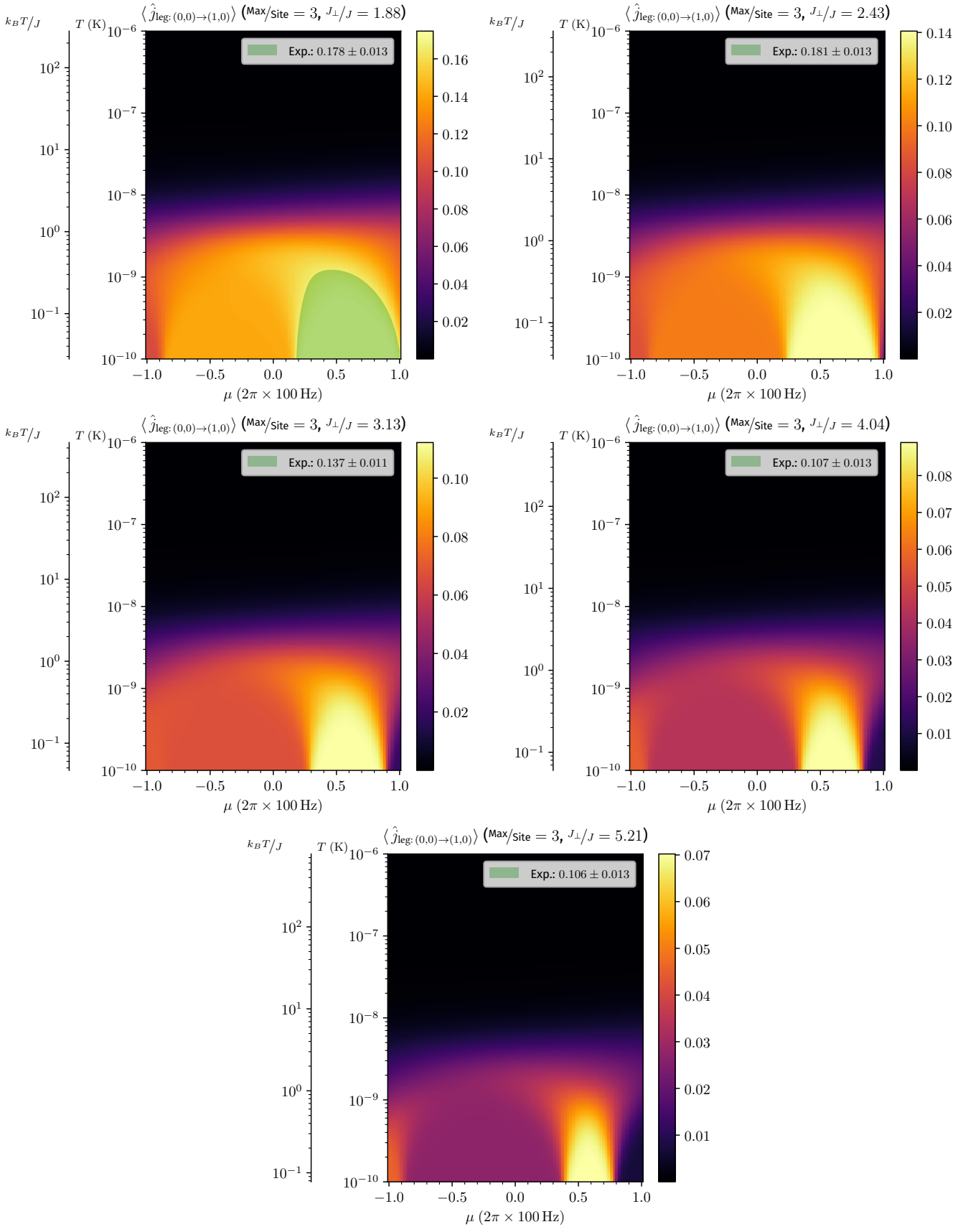

Figure 5.2: Parameter sweep over T and μ for the local current operator $\hat{j}_{\text{leg: (0,0)}\to\text{(1,0)}}$ in a plaquette (direct measurement, no parity projection, $U_0 = 9J_\perp$, open boundaries) for the experimental values $J_\perp/J = 1.88$ to $J_\perp/J = 5.21$. The green overlay represents the experimental measurement results [64]. Relevant absolute temperature range varies greatly between different $J_\perp/J$ values.

5.2 Numerical Verification of the Experimental Current Measurement Protocol

To truly be able to draw meaningful comparisons with experimental data, it is crucial that we take parity-projection and the experimental measurement protocol into account. Using the theoretical description in equation (2.48) and the methods described in chapter 4, We implemented the operators `j_leg_rot(r,l)` and `j_rung_rot(r)`, which respectively measure the leg and rung currents using the experimental protocol, and their parity-projected counterparts that take into account the parity projection in the final step of the measurement.

Just like how measurement devices in a laboratory have to be characterised, the correctness of scientific code is essential to the accuracy of the results obtained from it. As a consequence, testing scientific code is just as important as writing and using it, especially in this case where we have a complex measurement protocol and want to pinpoint the causes of discrepancies in the measured results. To test the correctness of our implementation of `j_leg_rot(r,l)` and `j_rung_rot(r)`, it is useful to respectively test them against a direct measurement of the operators $\langle \hat{j}_{\text{leg: }(r,l)\to(r+1,l)} \rangle$ and $\langle \hat{j}_{\text{rung: }(r,l)\to(r,l+1)} \rangle$ of the same state. Due to the equivalence of the measured values, at least in the non-interacting case, $\langle \hat{j}_{\text{leg: }(r,l)\to(r+1,l)} \rangle$ should, for example, be exactly equal to $\langle$`j_leg_rot(r,l)`$\rangle$, except for numerical errors.

Given the fact that we have already implemented the generation of the thermal state ρ_β, it was practical to use thermal states of some random temperature T_{rand} for the aforementioned unit tests[1]. Yet, while the tests worked for hard-core bosons (maximal occupation per site $M = 1$), setting $M \geq 2$ sometimes resulted in discrepancies that were rather perplexing. This was especially the case given that so far, tests for the implementation of the rest of the operators have been correct. As such, what was originally a routine unit test has seemingly revealed previously unnoticed intricacies of the current measuring protocol.

In retrospect, we suspect that a possible reason this issue went unnoticed previously is that simulations typically use only a symmetry subspace of some fixed particle number N. However, since we have not yet implemented the code for the projection into a fixed particle number sector, these thermal states were generated in the full Hilbert space, where these error effects are particularly pronounced.

In this section, we investigate and characterise the discrepancies that we have observed above. We will first examine the time evolution of the current operator eigenstates, followed by an analysis of the probability density distribution of our states during the experimental current measurement protocol. Finally, we will discuss the implications of these results for the experimental protocol.

[1] A *unit* test makes sure that a *unit* of code is doing what you think it does. Sources such as [62] goes into more details about testing in scientific software. In this case, we are testing the unit of code that implements the current measuring protocol as an operator.

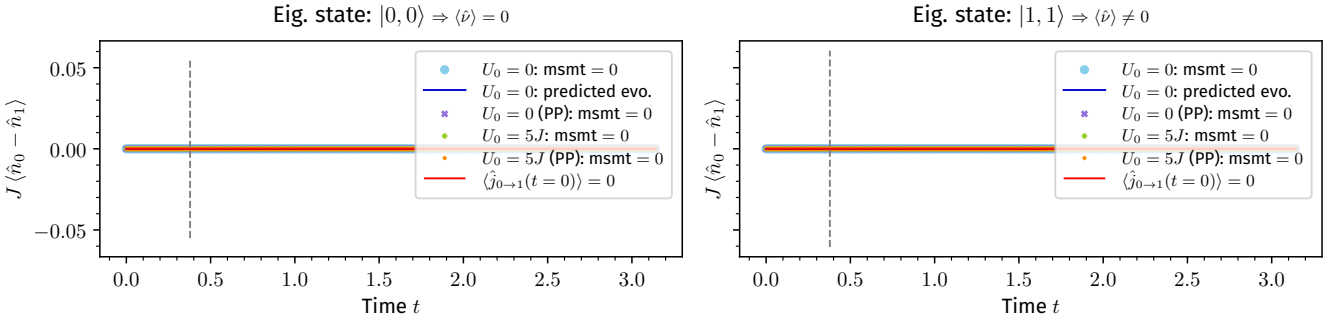

(a) Eigenvalue $(j = 0)$

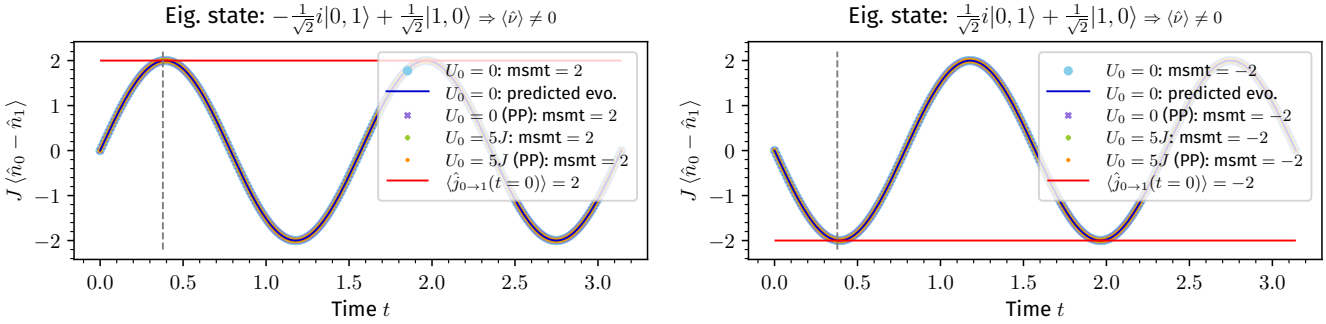

(b) Eigenvalue $(j = 2)$

(c) Eigenvalue $(j = -2)$

Figure 5.3: Time evolution using the current measurement protocol for hard-core bosons, with maximum occupancy per site $M = 1$ and $J/J_\perp = 2$. $\hat{\nu}$ is the validity observable as defined in (2.55). The gray vertical line is the time $t = \tau$ at which the measurement happens, and *msmt* gives the measured value. *(PP)* means that we also take parity projection into account. We observe that the protocol indeed works for all cases, even in the case of finite interactions U_0.

5.2.1 Time Evolution of Eigenstates of the Current Operator in a Double Well

To analyse the time evolution of any state during the protocol, it is useful to systematically examine time evolution of the eigenstates of the current operator. Since these eigenstates have a well-defined current corresponding to its eigenvalue, any non-zero current states are guaranteed to have a non-trivial time evolution. If the protocol works for all eigenstates, then it would also work for any state with some arbitrary current.

We begin with hard-core bosons. From Figure 5.3, we observe that the protocol indeed works for all eigenstates, even for the interacting case of $U_0 \neq 0$. Here, we included the $U_0 > 0$ case despite its inapplicability that was theoretically described in section 2.4. This is because anecdotal evidence suggests that, under some conditions, applying parity projection *after* basis rotation (with finite U_0 present) still yields results consistent with the non-interacting case [55]. We chose $J/J_\perp = 2$ so that the impact of a non-unity J would be obvious.

For soft core bosons, the story is no longer as straightforward. Some selected evolutions are

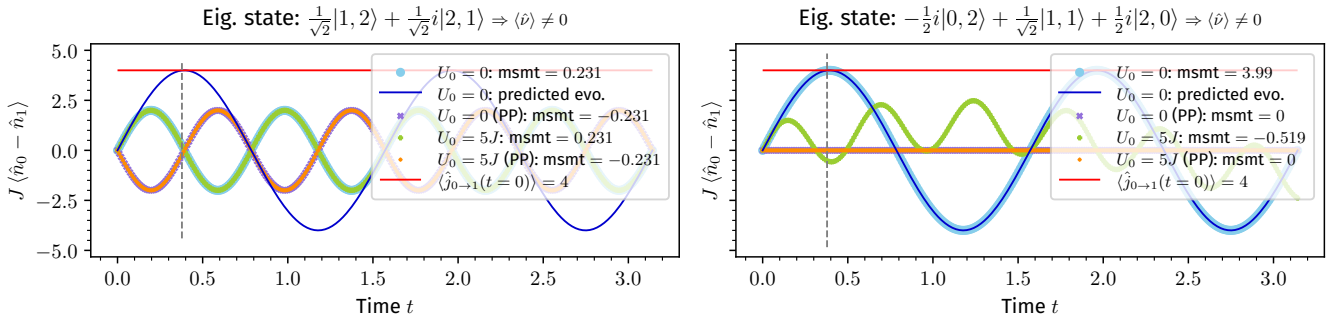

(a) $M = 2$, Eigenvalue $(j = 4)$

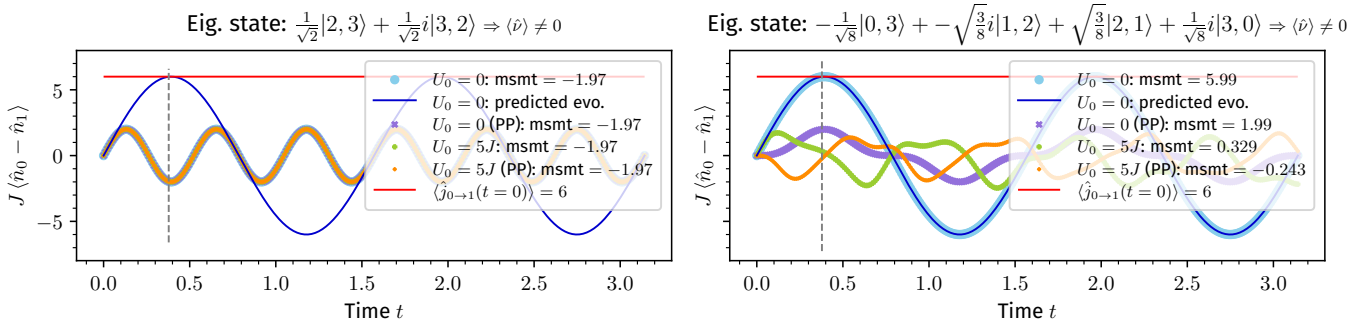

(b) $M = 3$, Eigenvalue $(j = 6)$

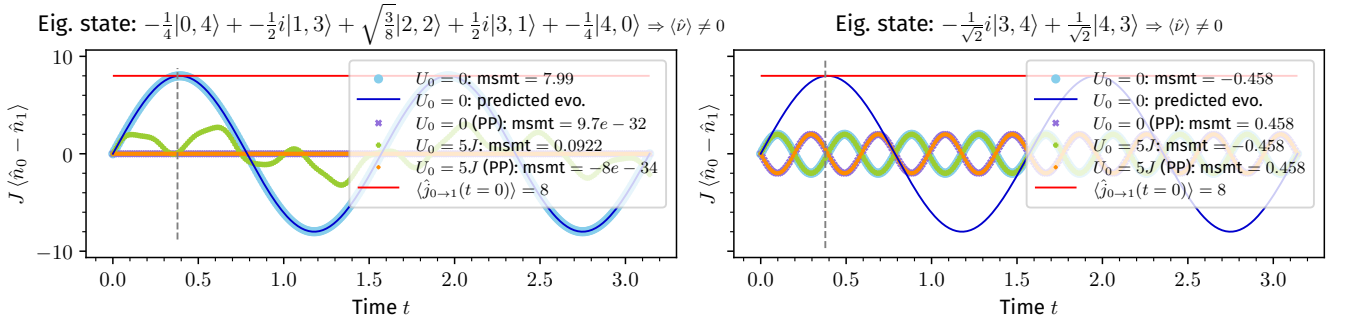

(c) $M = 4$, Eigenvalue $(j = 8)$

Figure 5.4: Time evolution of selected current eigenstates using the current measurement protocol (soft core bosons, maximum occupation per site $M = 2, 3, 4$, $J/J_\perp = 2$). $\hat{\nu}$ is the validity observable as defined in (2.55). The gray vertical line is the time $t = \tau$ at which the measurement happens, and *msmt* gives the measured value. *(PP)* means that we also take parity projection into account. We observe that a finite U_0 during the rotation, with or without parity projection, results in the wrong measured current. For eigenstates where the total number of particles is less than or equal to the maximum occupation per site, i.e. $N \leq M$, the measurement protocol works in the case where there is no parity projection.

depicted in Figure 5.4, with the full results documented in Appendix D. As we have predicted in section 2.4, having a finite interaction U_0 results in very different time evolutions that produce an incorrect measurement of the current using the protocol, whether with or without parity projection. We also confirmed (at least up to $M = 4$) that a vanishing expectation value of the validity operator $\langle \hat{\nu} \rangle = 0$ is indeed a *sufficient* but not *necessary* condition for the current measurement protocol to work, as evidenced by the evolutions in figures 5.4a (right), 5.4b (right), and 5.4c (left). For these evolutions, we see that the time evolution (light blue points) does indeed follow the theoretically predicted evolution of classical bosons (dark blue line) despite $\langle \hat{\nu} \rangle \neq 0$.

Looking at the other three evolutions, 5.4a (left), 5.4b (left), and 5.4c (right), we observe that the time evolution with $U_0 = 0$ and no parity projection never reaches the actual value of the current $\langle \hat{j}_{0\to1}(t = 0) \rangle$, nor did it follow the theoretically predicted evolution described by equation (2.46). To understand this intuitively, we may use the example of

$$\big|j = 6, v_j = 0\big\rangle = \frac{1}{\sqrt{2}} \left(|2, 3\rangle + i \, |3, 2\rangle \right) \ . \tag{5.1}$$

To measure the true current of $2(n_0 - n_1) = 6$, we observe that an occupancy difference of $(n_0 - n_1) = 3$ would be necessary. At the same time, since the Hamiltonian $\hat{H}_{\text{DW, hop}}$ preserves the total number of particles $N = 5$, the state would have to evolve to $|4, 1\rangle$. Given the maximum occupation of $M = 3$, this is simply not possible. As a result, the current measurement protocol fails.

Furthermore, from our analyses, we observe empirically that of all the eigenstates with a non-vanishing expectation of the validity observable $\langle \hat{\nu} \rangle \neq 0$, those with a total particle number of $N = M$ seem to work, suggesting that if the maximum occupancy per site M is chosen such that it is at least equal to the total number of particles N, then the current measurement protocol would still succeed. Intuitively, given some fixed number of particles N_{fix}, and the local dimension is large enough to exactly describe the dynamics, then the current measurement protocol will work as expected.

Last but not least, we observed that except in the case of hard-core bosons, parity projection systematically leads to the measurement of a reduced current as compared to the true current, and can sometimes even cause a sign flip of the measured current, resulting in significant loss of information.

Based on the evidence that we have gathered so far, we recognise that if the state that we would like to measure has components of these "pathological" states, as is the case with the thermal state, then we will experience these undesired finite-dimensional effects during the measurement of the local particle current using this protocol.

5.2.2 Understanding the Impact of Pathological States

How big is the impact of these "pathological" states on our current measurement? To provide further evidence to support our conclusions and understand the impact of these finite-dimensional effects with respect to the local current operator $\hat{j}_{\text{leg: }(0,0)\to(1,0)}$, we track the eigenvalue (measurement outcome) distribution of our state at three critical stages of the measurement protocol presented in section 2.4: (i) pre-rotation, (ii) post-unitary-rotation, and (iii) post-parity-projection, constructing corresponding measured eigenvalue distribution as previously described in section 4.5. We denote the current measured using the protocol as j_{rot}, and with parity projection $j_{\text{rot, pp}}$. Given some theoretical current j_{theo}, the percentage error in the histogram plots is given by:

$$\text{Percentage Error} = \frac{|j_{\text{theo}} - j_{\text{meas}}|}{|j_{\text{theo}}|} \times 100\,\% \quad \text{where} \quad j_{\text{meas}} = \left\{ j_{\text{rot}},\, j_{\text{rot, pp}} \right\} \tag{5.2}$$

We do this analysis for ground states and thermal states ($T = 10^{-9}\,\text{K}$) of a plaquette with different parameters (e.g. U_0, and whether this interaction is turned off during the rotation). Since $[\hat{H}_{\text{FL}}, \hat{N}] = 0$, every eigenstate of the Hamiltonian has a well-defined total particle number N associated with it, and we may use this to find the N-particle ground state of the plaquette. To obtain our initial pre-rotation state, we compute the reduced density matrix ρ_{DW} for the $(0,0) \to (1,0)$ double well.

For example, in Figure 5.5, we have a plaquette ground state with a fixed $N = 4$ and $U_0 = 0$. We observe that as we increase the maximum occupation per site M, the error in the middle column (i.e. after the rotation) decreases, until $M = N = 4$, at which point the error vanishes and the measured current using the protocol exactly matches the current of the initial state. We may understand this intuitively as follows: if the local dimension is too small, then the full dynamics cannot be captured. By increasing the local dimension until/beyond N, we obtain stable dynamics. This is despite the fact that we have projected our state onto a double well (two sites), where we would only expect half of the total number of particles as compared to a plaquette (four sites). While this is generally not a problem for small systems where the total number of particles are small, for larger flux ladder systems, the local M might need to be as large as N of the entire system, which can be very large. This confirms our observation from the previous subsection. Furthermore, we note that because $(n_0 - n_1)$ is discrete, any contributions from eigenstates with non-integer eigenvalues are automatically *pathological*. Eigenstates with large current eigenvalues also tend to be *pathological*.

Unfortunately, we cannot simply avoid this by increasing the number of experimentally bound states per site (i.e. M), especially if we have a generic thermal state or a ground state. This is because how these states look like also depend on the local Hilbert space dimensions on each site. In fact, we observe that if $U_0 = 0$ with no N restrictions, then both ground states and thermal states tend to be *pathological*. For example, in Figure 5.6, we see that at large M, both the thermal state and ground states of the plaquette have significant contributions from *pathological* eigenstates, either with non-integer eigenvalues or with large current eigenvalues, leading to errors as large as 94.55 % arising from the protocol.

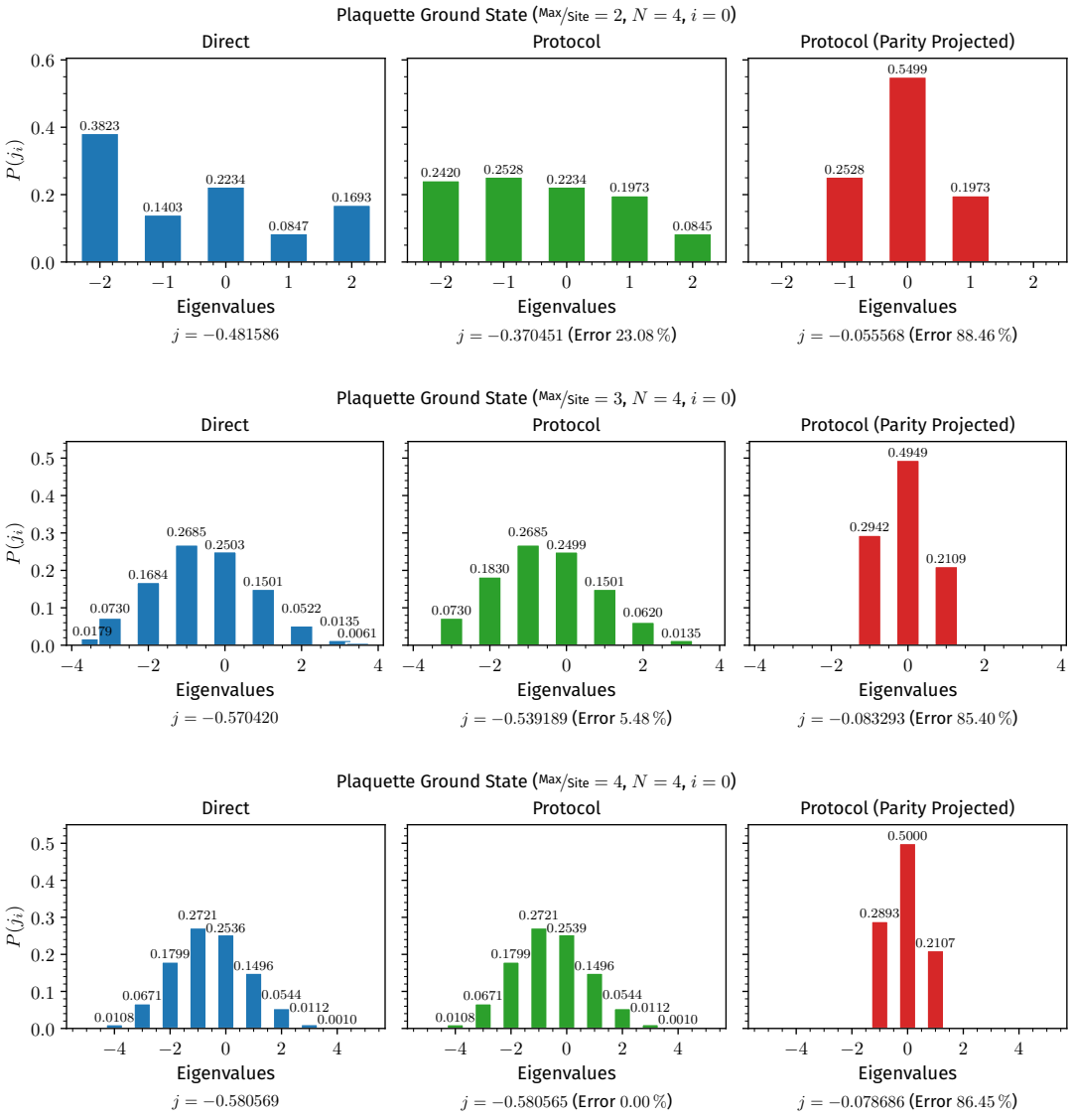

Figure 5.5: Probability distribution of the plaquette ground state with fixed $N = 4$ and $U_0 = 0$ projected onto a double well, with the maximum occupation per site $M = \{2, 3, 4\}$, $J/J_\perp = 1$, and $\varphi = 0.75 \cdot \frac{\pi}{2}$. We look at the initial state (left), state after the current measurement protocol (middle), and state after parity projection (right). We observe that increasing M until $M = N$ enables stable dynamics.

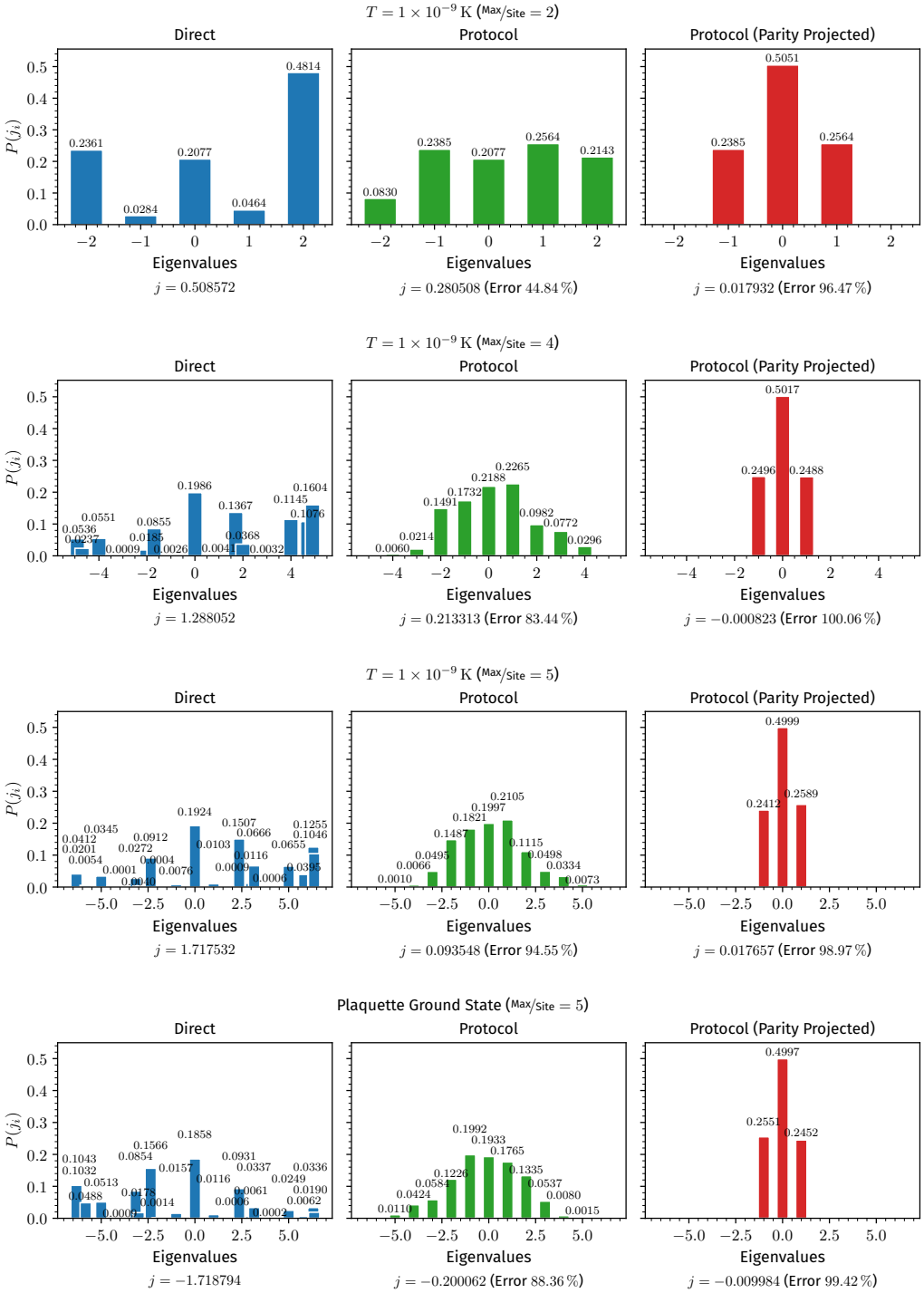

Figure 5.6: Probability distribution of the plaquette ground state and thermal state ($T = 1 \times 10^{-9}$ K, $U_0 = 0$) projected onto a double well, with the maximum occupation per site $M = \{2, 4, 5\}$, no restrictions on N, $J/J_\perp = 1$, and $\varphi = 0.75 \cdot \frac{\pi}{2}$. We look at the initial state (left), state after the current measurement protocol (middle), and state after parity projection (right). We observe that increasing M increases the error in the current measurement protocol.

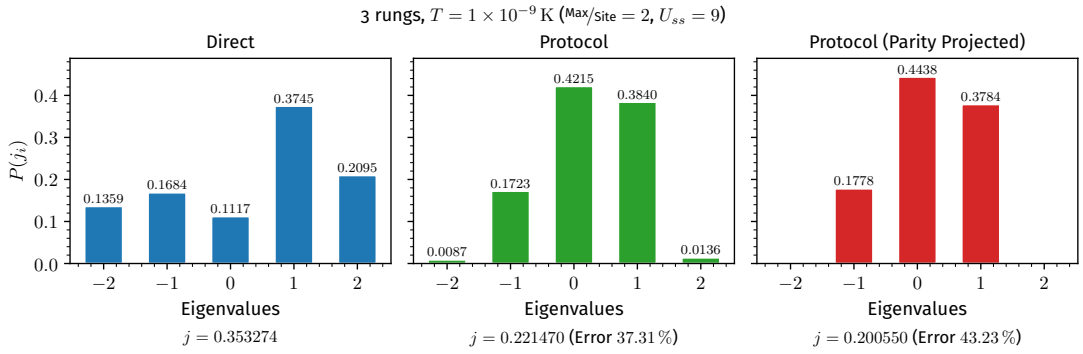

(a) Probability distribution of the 3-rung flux ladder thermal state with $J/J_\perp = 1$, $\varphi = 0.75 \cdot \frac{\pi}{2}$, and $M = 2$, analogous to Figure 5.6, except $U_0 = 9J_\perp$. The on-site interaction was not turned off during the rotation.

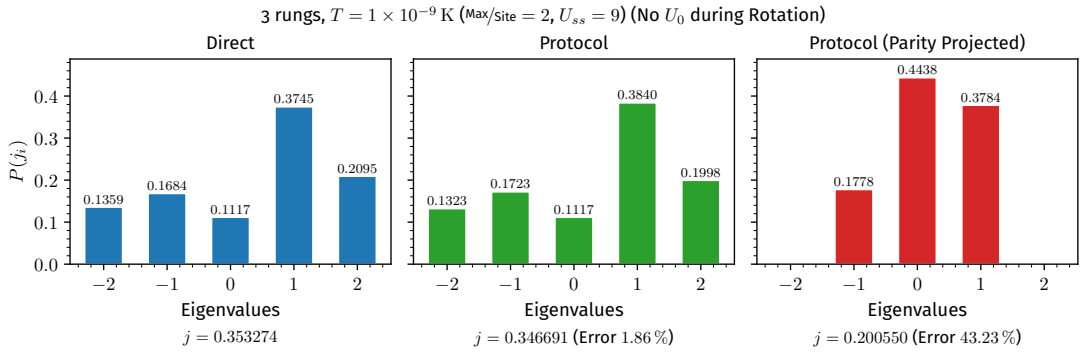

(b) Probability distribution of the 3-rung flux ladder thermal state with $J/J_\perp = 1$, $\varphi = 0.75 \cdot \frac{\pi}{2}$, and $M = 2$, analogous to Figure 5.6, except $U_0 = 9J_\perp$. The on-site interaction was turned off during the rotation.

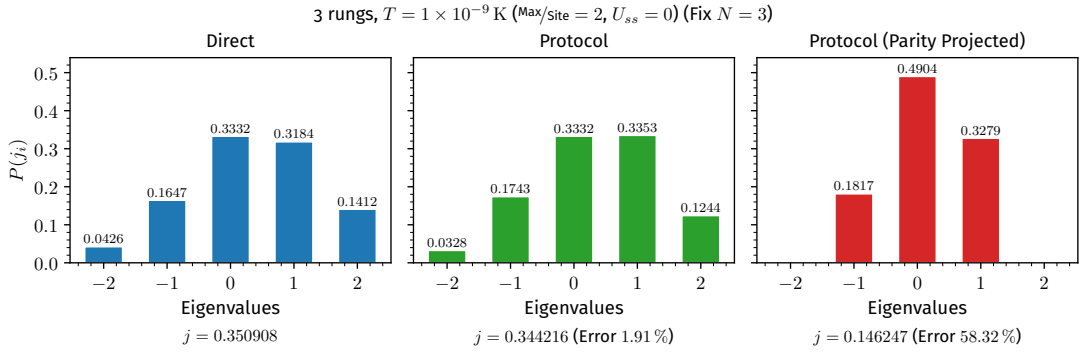

(c) Probability distribution of the 3-rung flux ladder thermal state with $J/J_\perp = 1$, $\varphi = 0.75 \cdot \frac{\pi}{2}$, $U_0 = 0$, and $M = 2$, analogous to Figure 5.6, except we fix the number of particles at half-filling: $N_{1/2} = 3 (> M = 2)$

Figure 5.7: Compared to Figure 5.6, the error from the current measurement protocol is greatly reduced. In the case where $U_0 > 0$, it is important to turn off on-site interactions during the protocol.

Experimentally, if we can effectively restrict the number of particles in the system, the probability of the occurrence of these pathological states could be **greatly reduced**. This may be achieved by either (1) using a large U_0 and then turning off this interaction during the rotation (e.g. using magnetic Feshbach resonances [19]), or (2) experimentally fixing the number of particles in the system. We demonstrate this in Figure 5.7 with the thermal state of a 3-rung flux ladder projected onto the double well $\big[(0,0),(1,0)\big]$. Here, we see that although the error introduced by the protocol does not vanish, it is greatly reduced ($< 2\,\%$) despite the fact that $M = 2$ is less than $N_{1/2} = 3$, which corresponds to the system at half-filling.

As established in the previous subsection, anecdotal evidence suggests that in the interacting case ($U_0 > 0$), parity projection applied after a basis rotation with finite U_0 yields results consistent with a basis rotation where interactions are turned off [55]. Our quantitative analysis now directly corroborates this observation, at least for the states that we have tested: comparing Figure 5.7a ($j_{\text{pp, int}}$) and Figure 5.7b ($j_{\text{pp, no int}}$), we observe that the measured parity-projected currents are indeed the same regardless of whether interactions were turned off during the basis rotation. For other tested states not presented here where there were no exact agreement, $j_{\text{pp, int}}$ and $j_{\text{pp, no int}}$ only differed up to 5 % from each other.

In all cases, parity projection results in a large loss of information, and is one of the main sources of error during the experimental measurement of local particle currents, even for systems with half-filling.

As such, our key observations may be summarised as follows:

- Using a finite interaction U_0 during state-preparation or strictly controlling the number of particles in the whole system N results in initial states that work better with the protocol.
- In the ideal case, the number of experimentally bound states (M) should at least be as many as N, which may be very large for larger systems.
- Parity projection results in large errors in the current measurement in all cases except in the case of hard-core bosons, (potentially) dwarfing other sources of error.

With this analysis, we are now confident that the errors we have observed previously were intrinsic to the current measuring protocol, and that the operators which incorporate the current measurement protocol, `j_leg_rot(r,l)` and `j_rung_rot(r)`, have been correctly implemented in the code.

5.3 Preparation for Larger System Dynamics

In order to simulate the dynamics of larger systems, it is necessary to use MPS techniques due to the exponentially increasing Hilbert space dimension of the system, making calculations intractable for the ED techniques that we have been using so far. Since an MPS can only describe pure states, we use state purification and imaginary time evolution with the time-dependent variational principle (TDVP) method to create a thermal state, as we have previously explored in section 4.6. As expected, the observables computed from our MPS thermal state agree with

those from our ED thermal state. In particular[2], for $\beta_{\text{rand}} = 1.2850/J$, and a TDVP time-step of $\delta t = -0.01i$, the errors in local observables, $\langle \hat{n}_{(r,l)} \rangle$, were $< 10^{-5}$, while the errors in non-local observables, $\langle \hat{j}_{\text{leg}} \rangle$, $\langle \hat{j}_{\text{rung}} \rangle$, $\langle \hat{H} \rangle$, were $< 10^{-2}$.

Adjusting the time-step δt, and comparing different methods used in the imaginary time evolution, we find that the error

$$\varepsilon(\hat{O}) = 100\,\% \cdot \frac{\left| \langle \hat{O} \rangle_{\text{MPS}} - \langle \hat{O} \rangle_{\text{ED}} \right|}{\langle \hat{O} \rangle_{\text{ED}}}, \tag{5.3}$$

averaged over all the previously mentioned observables, scales with the chosen δt. There was were also little difference observed between the methods employed in TDVP, global subspace expansion (GSE) and local subspace expansion (LSE), allowing us choose the less computationally expensive LSE for calculating our thermal states. This behaviour is depicted in Figure 5.8. With that, we can be confident that our implementation of the MPS thermal state is correct, and higher accuracy is achievable through smaller δt values in the imaginary time evolution at the cost of longer computation times due to the finer discretisation. This in turn lays a solid foundation upon which the study of local currents may be extended to larger system sizes closer to that achievable in experiments.

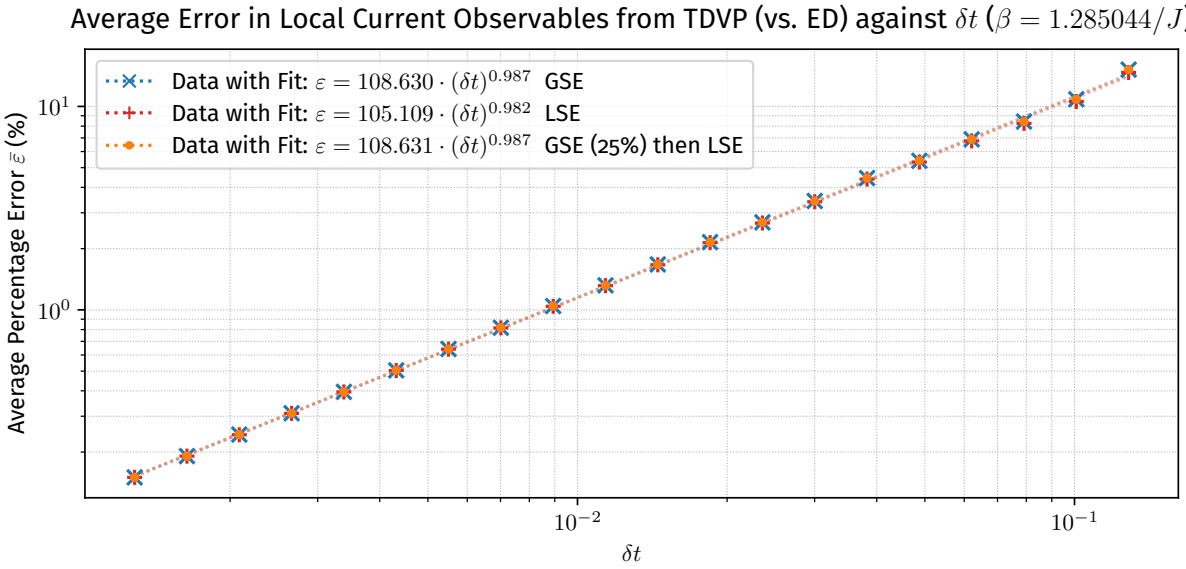

Figure 5.8: The observables $\hat{n}_{(r,l)}$, $\hat{j}_{\text{leg: }(r,l)\to(r+1,l)}$, $\hat{j}_{\text{rung: }(r,l)\to(r,l+1)}$ and $\hat{H}$ of the MPS thermal state were compared to that of the ED thermal state. We plot the average percentage error ε of the MPS observables against the TDVP time step δt. We observe that increased numerical accuracy can be achieved by reducing δt, and that there is no significant difference in accuracy between the different methods used in TDVP.

[2]Unless otherwise specified, we used a plaquette (2×2) as our test system in this section, with the coupling ratio $J/J_\perp = 1$, the complex phase $\varphi = \pi/2$, and a maximum occupation per site of $M = 3$.

5.4 Finite Temperature Effects: Rung Correlator

Using the toolkit that we have developed, we then performed finite temperature MPS simulations and compared that to the experimental measurements [85] and ED simulations of the parity-projected rung correlator $\bar{C}_{\text{rung}}$ published by Impertro et al. [19], where the parity-projected rung correlator $C_{\text{rung,pp},\,r}$ for some rung r is defined as:

$$C_{\text{rung,pp},\,r} = \langle \hat{n}_{\text{pp},(r,0)} \hat{n}_{\text{pp},(r,1)} \rangle - \langle \hat{n}_{\text{pp},(r,0)} \rangle \langle \hat{n}_{\text{pp},(r,0)} \rangle \ , \tag{5.4}$$

Each experimental data point was averaged over 30 repetitions and 14 ladders with 48 sites, which are system sizes much bigger than the (2×6) or even the (2×10) system that we have simulated here. As such, we use periodic boundary conditions in our simulations to (hopefully) better capture the physics of these large experimentally realised systems. Importantly, this observable is directly accessible in the quantum gas microscope without the need for any basis rotation, allowing us to separate the effects of the experimental current measurement protocol from the state itself. Here, just one of the U_0 value $U_0/J = 11.02(5)$ was sufficient in helping us provide a benchmark for our simulations. For the (6×2) system, we aggregate data from an $N = 5$ and an $N = 6$ simulation with the weights 0.6 and 0.4 to recover the experimental filling of 0.45,

From Figure 5.9, we see that despite using completely different methods, we observe good agreement between the physics captured by our simulation results and the simulation results from Impertro et al. There is therefore a high probability of correctness of the simulations that we have developed here.

Given the computational efficiency of MPS techniques, we were also able to extend upon the temperature[3] range of the simulation to $T = 0.05J$ to $3.0J$, and $J_\perp = 0.3J$ to $2.5J$ over a total of $(70 \times 30) = 2100$ datapoints, corresponding to a resolution of $\Delta J_\perp = 0.0759J$ and $\Delta T = 0.0428J$. This provides data beyond prior results in the range of $T = 1J$ to $0.5J$. For the plots that we see here, we show only most relevant temperature range of $T = 0.1J$ to $1.5J$ to reduce clutter. Due to the continuous nature of the change in the curve with a change in temperature observable in Figure 5.9a, we can even further extrapolate the behaviour beyond the range that we have simulation data for.

In order to probe the effects of an even larger system, we do the same finite temperature simulations for a (10×2) lattice, the results of which is depicted in Figure 5.10. Since $0.45 \times 20 = 9$ is an integer, we no longer need to aggregate our results over two different N values. The general trend of the curves are qualitatively similar to the (2×6) system, with signatures in the temperature curves getting continuously weaker with increasing temperature. However, the shape of the curves at low temperatures, especially at larger coupling ratios $J_\perp/J$, differ significantly between the two system sizes.

While not very obvious in the simulation curves of the (6×2) system, a phase transition around $J_\perp/J \approx 0.8$ is clearly visible at low temperatures in the larger (10×2) simulations. This phase

[3] We drop the constant k_B in $k_B T/J$ following common practice. This also helps to improve clarity.

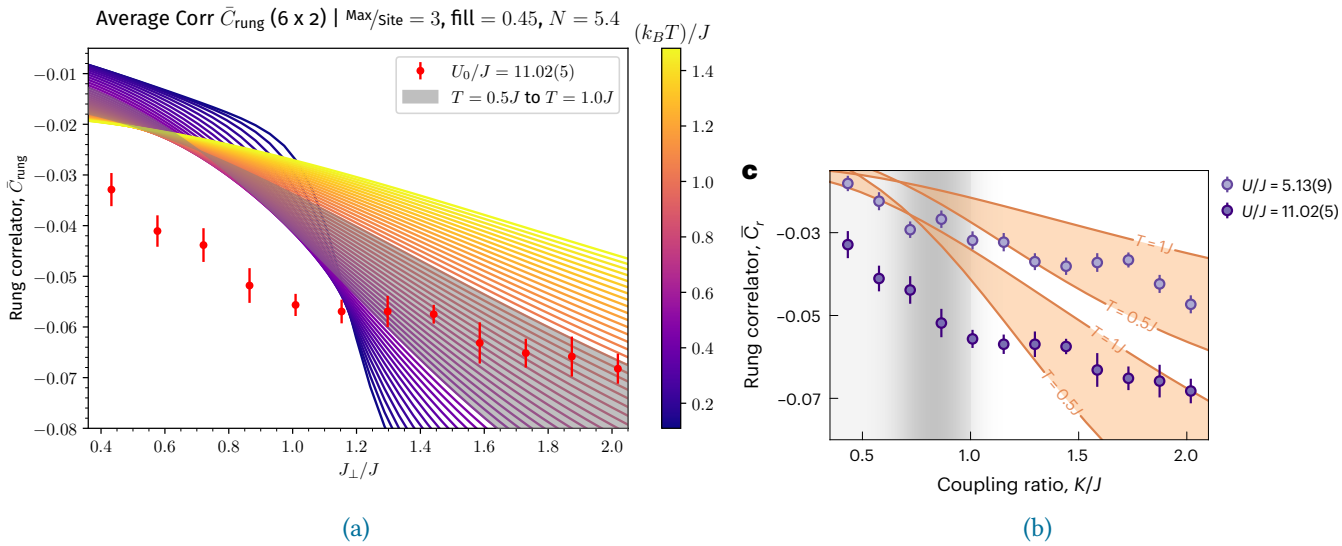

(a) (b)

Figure 5.9: Average parity-projected rung correlator $\bar{C}_{\text{rung}}$ and finite temperature simulations (6×2) with $\varphi = \pi/2$ and periodic boundary conditions along the legs. (a) Finite-temperature MPS simulations for $U_0/J = 11.02$ across $T/J = 0.1$ to 1.5, overlaid with experimental data [85]. Error bar is s.e.m.. (b) Finite-temperature ED simulations and experimental measurements from Impertro et al. Each experimental data point was averaged over 30 repetitions and 14 ladders with 48 sites [15, Figure 5(c), CC BY 4.0]. The data and simulations curves for $U_0/J = 5.13(9)$ are not relevant for our comparison. Our MPS results in (a) reproduce the published data in (b) and extend the temperature range beyond prior results, providing data above $T = 1J$ and below $T = 0.5J$.

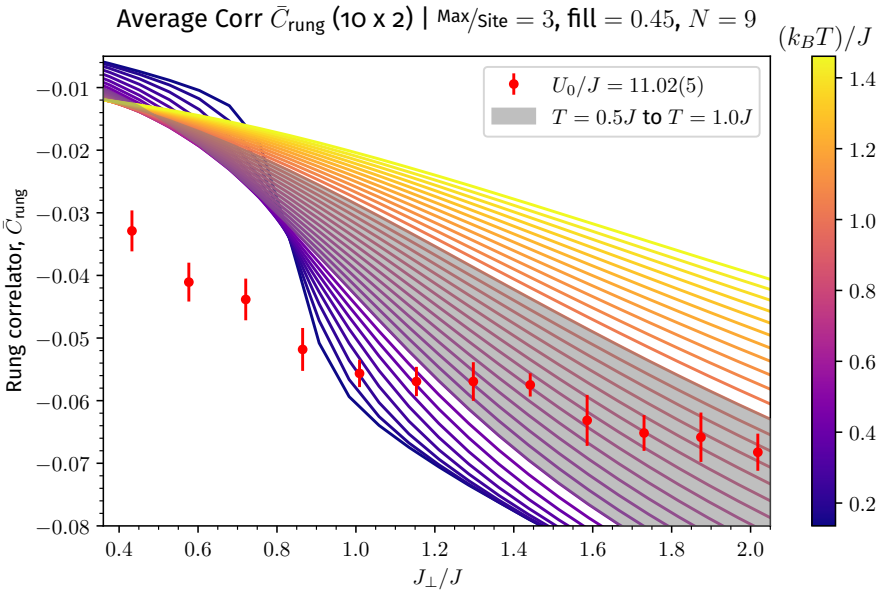

Figure 5.10: Average parity-projected rung correlator $\bar{C}_{\text{rung}}$ and finite temperature simulations (10×2) with $\varphi = \pi/2$ and periodic boundary conditions along the legs, and $U_0/J = 11.02$. Finite-temperature MPS simulations curves over $T/J = 0.1$ to 1.5 are overlaid with experimental data [85]. Error bar is s.e.m..

transition is however **completely not visible** in the experimental data. The general shape of the data points also generally deviates from the signature of the simulated curve for both system sizes simulated. Where the data points do overlap with the simulation curves, they overlap over a large range of T/J values. Given that the investigated temperature range correspond well to the observations we have previous made in section 5.1, this incongruence is unlikely to be explained by finite temperature effects.

As such, close comparison between the simulation results and experimental data for the parity-projected average rung correlator $\bar{C}_{\text{rung}}$ strongly indicates that the experimentally realized state is not a finite-temperature state.

Chapter 6

Conclusion and Outlook

6.1 Summary

Scientific Results In this thesis, we have systematically investigated the experimental current measurement protocol as proposed by Kessler and Marquardt [16], both analytically and numerically, for a system of soft-core bosons. By explicitly re-deriving the expressions used for the protocol, we could incorporate the error terms resulting from the non-bosonic commutation relation of soft-core bosons.

The results in the previous chapter, chapter 5, provide a systematic and rigorous numerical verification of the current measurement protocol, allowing us to have a better understanding of the conditions under which the protocol does work. In fact, we realize that this protocol is generally not valid for a system with soft-core bosons, and we find that:

(a) Using a finite interaction U_0 during state-preparation or strictly controlling the number of particles in the whole system N results in initial states that work better with the protocol.

(b) In the ideal case, the number of experimentally bound states (M) should at least be as many as total number of particles in the system N, which may be very large for larger systems.

(c) Parity projection results in large errors in the current measurement in all cases except in the case of hard-core bosons, (potentially) dwarfing other sources of error.

Theoretically, one could use the condition $\langle \hat{\nu} \rangle = 0$, where $\hat{\nu}$ is the *validity* observable as defined in (2.55), to determine if the current measurement protocol will work with a given state, but it is only a *sufficient* but not *necessary* condition for the current measurement protocol to work. A more robust but computationally expensive way would be to determine the exact subspaces in which the protocol works by calculating explicitly the first term in equation (2.52).

Without improved characterisation of experimental parameters such as the local Hilbert space (e.g. in terms of the depth of the potential) in relation to the number of particles N, there are simply too many confounding error sources. Consequently, isolating finite-temperature effects

to assess their specific contribution to the current measurement error is very challenging. The fact that only parity-projected occupations can be measured also results in a significant loss of information that cannot easily be accounted for.

To circumvent the limitations of the current measurement protocol, we also performed finite-temperature matrix product state (MPS) simulations of the rung correlator for a larger (6×2) and a (10×2) system. Our analysis of the results compared to the experimental data provided strong evidence that the experimentally realised state by Impertro et al. [15] is not a thermal state. Here, we observe from our simulation data that signatures of the rung correlator do indeed get weaker with increasing temperature, which is consistent with what we expect of a high-temperature state.

All in all, at least with the available data, we conclude that the state realised in the experiments of Impertro et al. [15] is very likely neither a ground state, nor a thermal state, but rather a non-equilibrium state.

Technical Results Besides scientific results, we have also developed a well-tested and robust numerical toolkit in Python for investigating the physics of bosonic flux ladders. The toolkit produces not just exact results for smaller systems using exact diagonalisation (ED) techniques (using both dense and sparse representations), but also approximate results for larger system using MPS techniques.

Furthermore, the toolkit provides a unified interface across ED and MPS backends, allowing high-level scripts to easily switch between the two backends based on the requirements of the task at hand. Given the various levels of abstraction and modularisation, the code is also expected to be easy to maintain, should it be useful in other contexts.

By exploiting fixed-N symmetries, we were able to use ED techniques to reach system sizes of up to (6×2), with a local maximum occupation per site of $M = 3$ (i.e. four states per site), which is equivalent to a system of $N_{\text{spin}} = 24$ spins. For MPS calculations using the SyTen toolkit [59, 60], thermal states for system sizes as large as (10×2) (40 sites due to purification) were calculated for results in this thesis.

6.2 Outlook

The work in this thesis provide a solid foundation for future work in the field of bosonic flux ladders, and in general, ultracold atoms in optical lattices, especially in the context of current measurements.

Given that we cannot describe our experimentally realised state as a thermal state or a ground state, the next natural step is to use an open quantum system approach to describe the system. We do note that however, the Davies map [86, 87] does not work as the spectrum of our Hamiltonian is degenerate. In that regard, it could also be useful to investigate the impact on our states if we take into account the characterised finite residual hopping strength from our ladder to neighbouring ladders.

At the same time, we can continue to push our MPS calculations to even larger system sizes that require more compute time so that we can provide a better understanding of the impact of system size on our observables, e.g. the rung correlator.

In the specific context of measuring current, further characterisation of the experimental system with regard to the size of the local Hilbert space on each site, potential depth and the number of particles would provide much deeper insights into the sources of errors in the system. We can further complement this by calculating the first term of (2.52) explicitly for different M-values to determine the subspaces in which the current measurement protocol works reliably.

Finally, the analysis of the current measurement protocol could also easily be expanded to larger system sizes by generating the state using MPS methods, and then taking the partial trace of the state over all sites except for the double-well that we are interested in. We can then feed this double-well state into the ED solver and run numerical analyses using ED, thereby allowing us to combine the strengths of both methods into a single calculation.

The codes used in this thesis are made available for archival purposes at [88].

Appendix A

Building Global Single-Site Projectors from Operators Exclusively

Due to the nature of quantum gas microscopes for experimental realisations of ultracold atoms, direct experimental measurements of local occupations is limited to a parity projection (see section 3.2). To simulate that, we utilise single-site projectors $\hat{P}_m^{(r,l)}$ as defined in Equation 4.2:

$$\hat{P}_0^{(r,l)} = |0\rangle_{(r,l)}\langle 0|_{(r,l)} = \frac{\left(\hat{b}_{(r,l)}\right)^M \left(\hat{n}_{(r,l)}\right) \left(\hat{b}^\dagger_{(r,l)}\right)^M}{M \cdot M!} \,, \tag{A.1}$$

and recursively for $m = 1, 2, \ldots, M$:

$$\hat{P}_m^{(r,l)} = |m\rangle_{(r,l)}\langle m|_{(r,l)} = \frac{\hat{b}^\dagger_{r,l}\, \hat{P}^{(r,l)}_{m-1}\, \hat{b}_{r,l}}{m} \,. \tag{A.2}$$

Here, M is the maximum occupation per site. Although irrelevant to the simulations done in this thesis, do note that if the local occupation per site is unbounded, then this expression would not work.

Motivation

The usual way of making a global single-site projector is to start with a local single-site projector, and then expanding this single-site project into a global operator. Unfortunately, doing this would require higher-level code (my code, i.e. `FluxLadder_ED` and `FluxLadder_MPS`) to know how the exact representation of a state / projector looks like (libraries that my code uses, i.e. `pyten` and `evos`), and does not respect the abstraction that was built into the simulation code.

To motivate this abstraction further: Given some Hilbert space $\mathcal{H}$, we represent states $|v_i\rangle \in \mathcal{H}$ using vectors $\vec{v_i} \in \mathbb{C}^{\dim(\mathcal{H})}$ in exact diagonalisation (ED) code. This mapping between $\mathcal{H}$ and $\mathbb{C}^{\dim(\mathcal{H})}$ is not unique and may be arbitrarily chosen. While many people choose reasonable

mappings, it can still be ambiguous. For example, in a two-level system with $|0\rangle$ and $|1\rangle$, both of the following mappings are equally valid:

- $|0\rangle = \begin{pmatrix}0\\1\end{pmatrix}, |1\rangle = \begin{pmatrix}1\\0\end{pmatrix}$
- $|0\rangle = \begin{pmatrix}1\\0\end{pmatrix}, |1\rangle = \begin{pmatrix}0\\1\end{pmatrix}$

To add contribute further to the ambiguity, in a many-body quantum system, the global state or operator would be constructed via a tensor product of local site-specific components. The final representation thus *implicitly* depends on some predefined ordering of the sites (e.g. left-to-right, or right-to-left). While this ordering is pre-defined, taking it into account outside of the underlying library can be error-prone.

It is thus best to leave the *concrete* representation to the libraries itself, and only use the operators and states from the library in an abstract manner.

Deriving the expression for the projector

We may write a local particle number operator as such:

$$\hat{n}_{(r,l)} = \sum_{n=0}^{M} n\,|n\rangle\langle n| = \cancel{0\,|0\rangle\langle 0|} + 1\,|1\rangle\langle 1| + \ldots + M\,|M\rangle\langle M| \ , \tag{A.3}$$

where $|i\rangle\langle i|\,, i \in \mathbb{N}_0, i \leq M$ refers to the global single-site projector to the state $|i\rangle_{(r,l)}$.

Upon application of $\hat{b}_{(r,l)}$ on the left and $\hat{b}^\dagger_{(r,l)}$ on the right, we obtain:

$$\left(\hat{b}_{(r,l)}\right)\left(\hat{n}_{(r,l)}\right)\left(\hat{b}^\dagger_{(r,l)}\right) = 1(1)\,|0\rangle\langle 0| + 2(2)\,|1\rangle\langle 1| + \ldots + M(M)\,|M-1\rangle\langle M-1| \ . \tag{A.4}$$

Applying $\hat{b}_{(r,l)}$ on the left and $\hat{b}^\dagger_{(r,l)}$ on the right again yields:

$$\begin{aligned}\left(\hat{b}_{(r,l)}\right)^2\left(\hat{n}_{(r,l)}\right)\left(\hat{b}^\dagger_{(r,l)}\right)^2 = \cancel{\hat{b}_{(r,l)}\,|0\rangle\langle 0|\,\hat{b}^\dagger_{(r,l)}} &+ 2(2)(1)\,|0\rangle\langle 0| \\ &+ \ldots \\ &+ M(M)(M-1)\,|M-2\rangle\langle M-2| \ .\end{aligned} \tag{A.5}$$

After successively applying the operators M times, we obtain the following:

$$\left(\hat{b}_{(r,l)}\right)^M\left(\hat{n}_{(r,l)}\right)\left(\hat{b}^\dagger_{(r,l)}\right)^M = M(M!)\,|0\rangle\langle 0| \ . \tag{A.6}$$

Dividing the coefficient on both sides of the equation, we obtain exactly Equation A.1:

$$\frac{\left(\hat{b}_{(r,l)}\right)^M\left(\hat{n}_{(r,l)}\right)\left(\hat{b}^\dagger_{(r,l)}\right)^M}{M \cdot M!} = |0\rangle\langle 0| \ . \tag{A.7}$$

From there, we can simply recursively apply $\hat{b}^{\dagger}_{(r,l)}$ on the left and $\hat{b}_{(r,l)}$ on the LHS of the expression (A.7) to obtain projectors for higher occupations. Since the application of the operators also results in an additional factor m, we have to normalise the resulting operator with $1/m$ to obtain the expression in Equation A.2.

Appendix B

Derivation of the Definition for the Local Particle Current on a Site

The expressions for the local currents on each site may be derived from a couple of basic concepts and equations. In particular, we make use of the continuity equation together with the Heisenberg equation of motion for our derivation. This appendix expands upon the short explanation in Section D of the supplementary information of Impertro et al. [19] and presents the derivation in more details for future reference, allowing us to clarify any implicit assumptions that went into the definition of the current operator in its popular current form.

We start with the Hamiltonian presented in Equation (2.11) in the thesis. In order to have a more general description, we expand the system into a generic lattice of sites, as we see in Figure B.1. This way, we can explore all four directions a particle at a site (r, l) may hop to. In particular, this description encompasses both the case where the site is on the upper leg (i.e. $l = 0$ and there is only coupling to the site below), and the case where the site on the lower leg (i.e. $l = 1$ and there is only coupling to the site above).

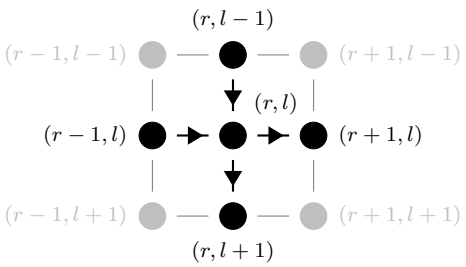

Figure B.1: Sketch of the square lattice around the site (r, l), showing the current from its nearest neighbours.

Using this expanded lattice, the Hamiltonian becomes the general Hofstadter-Bose-Hubbard (HBH) Hamiltonian in the rung gauge:

$$\hat{H}'_{\mathrm{HBH}} = \overbrace{-J\sum_{r,l}\left(\hat{b}^{\dagger}_{(r,l)}\hat{b}_{(r+1,l)} + \mathrm{h.c.}\right)}^{(1)\ \text{Hopping along legs}} \overbrace{-J_{\perp}\sum_{r,l}\left(e^{-ir\varphi}\cdot\hat{b}^{\dagger}_{(r,l)}\hat{b}_{(r,l+1)} + \mathrm{h.c.}\right)}^{(2)\ \text{Hopping along rungs}} + \underbrace{\sum_{r,l}\frac{U_0}{2}\left[\hat{n}_{(r,l)}\left(\hat{n}_{(r,l)} - 1\right)\right]}_{(3)\ \text{On-site interaction}}, \tag{B.1}$$

where J and $J_\perp$ are the tunnelling amplitudes along the legs and the rungs respectively, and U_0 the on-site inter-particle repulsion.

Since the system has a $U(1)$ symmetry with respect to the total particle number over the whole lattice, it follows from the conservation of particles that we can use the continuity equation to obtain the definition of the current operator. We start with the continuity equation in its differential form:

$$\frac{\partial}{\partial t}\hat{n}_{(r,l)[\mathrm{H}]} + \boldsymbol{\nabla}\cdot\hat{\mathbf{J}}_{(r,l)[\mathrm{H}]} = 0\,, \tag{B.2}$$

where $\hat{\mathbf{J}}_{(r,l)[\mathrm{H}]} = \left(\hat{j}_{\text{leg: }(r,l)[\mathrm{H}]}, \hat{j}_{\text{rung: }(r,l)[\mathrm{H}]}\right)^T$ is the particle current operator vector, and $\hat{n}_{(r,l)[\mathrm{H}]}$ is the particle number operator. Here, we are in the Heisenberg picture in which it is the observables and not the states that evolve in time. This is denoted by the subscript [H]. We note that in this case, the continuity equation differs slightly from that used in Impertro et al. [19] and Kessler and Marquardt [16].

Divergence of Current Since we have a *discrete* lattice, the second term gives the *discrete* divergence of the current operator. We may then use the method of finite difference to write the divergence explicitly:

$$\begin{aligned}\boldsymbol{\nabla}\cdot\hat{\mathbf{J}}_{(r,l)[\mathrm{H}]} &= \begin{pmatrix}\partial_r\\ \partial_l\end{pmatrix}\cdot\begin{pmatrix}\hat{j}_{\text{leg: }(r,l)[\mathrm{H}]}\\ \hat{j}_{\text{rung: }(r,l)[\mathrm{H}]}\end{pmatrix} = \partial_r\left(\hat{j}_{\text{leg: }(r,l)[\mathrm{H}]}\right) + \partial_l\left(\hat{j}_{\text{rung: }(r,l)[\mathrm{H}]}\right)\\ &= \frac{\hat{j}_{\text{leg: }(r+1,l)[\mathrm{H}]} - \hat{j}_{\text{leg: }(r,l)[\mathrm{H}]}}{\Delta r} + \frac{\hat{j}_{\text{rung: }(r,l+1)[\mathrm{H}]} - \hat{j}_{\text{rung: }(r,l)[\mathrm{H}]}}{\Delta l}\,,\end{aligned} \tag{B.3}$$

Since $\Delta r = \Delta l = 1$, (B.2) becomes:

$$\frac{\partial}{\partial t}\hat{n}_{(r,l)[\mathrm{H}]} + \left(\hat{j}_{\text{leg: }(r+1,l)[\mathrm{H}]} - \hat{j}_{\text{leg: }(r,l)[\mathrm{H}]} + \hat{j}_{\text{rung: }(r,l+1)[\mathrm{H}]} - \hat{j}_{\text{rung: }(r,l)[\mathrm{H}]}\right) = 0 \tag{B.4}$$

Heisenberg Equation of Motion On the other hand, we know from the Heisenberg equation of motion [46] that for an operator like $\hat{n}_{(r,l)[\mathrm{S}]} = \hat{b}^\dagger_{(r,l)[\mathrm{S}]}\hat{b}_{(r,l)[\mathrm{S}]}$ that has no explicit time-dependence in the Schrödinger picture, we can write its time-derivative in the Heisenberg picture as:

$$\frac{\mathrm{d}}{\mathrm{d}t}\hat{n}_{(r,l)[\mathrm{H}]} = \frac{i}{\hbar}\left[\hat{H}'_{\mathrm{HBH},[\mathrm{H}]}, \hat{n}_{(r,l)[\mathrm{H}]}\right] + \cancel{\left(\frac{\mathrm{d}}{\mathrm{d}t}\hat{n}_{(r,l)[\mathrm{S}]}\right)_{[\mathrm{H}]}}\,. \tag{B.5}$$

At this point, we make the observation that although time-independent (Schrödinger picture) and time-dependent (Heisenberg picture) operators generally differ, their functional forms remain identical, for example for the particle number operator:

$$\hat{n}_{(r,l)[\mathrm{S}]} = \hat{b}^\dagger_{(r,l)[\mathrm{S}]}\hat{b}_{(r,l)[\mathrm{S}]} \qquad \rightarrow \qquad \hat{n}_{(r,l)[\mathrm{H}]}(t) = \hat{b}^\dagger_{(r,l)[\mathrm{H}]}(t)\hat{b}_{(r,l)[\mathrm{H}]}(t)\,.$$

Most importantly, the equal-time commutation relations are preserved, for example:

$$\left[\hat{b}_{(r,l)[\mathrm{S}]}, \hat{b}^\dagger_{(r,l)[\mathrm{S}]}\right] = 1\,. \qquad \Leftrightarrow \qquad \left[\hat{b}_{(r,l)[\mathrm{H}]}(t), \hat{b}^\dagger_{(r,l)[\mathrm{H}]}(t)\right] = 1$$

As such, the commutator in (B.5) may be easily calculated. Given that $\hat{n}_{(r,l)[\mathrm{H}]} = \hat{b}^\dagger_{(r,l)[\mathrm{H}]}\hat{b}_{(r,l)[\mathrm{H}]}$, we find that

$$\left[\hat{b}_{(s,m)[\mathrm{H}]}, \hat{n}_{(r,l)[\mathrm{H}]}\right] = \hat{b}_{(s,m)[\mathrm{H}]}\delta_{sr}\delta_{lm} \quad \text{and} \quad \left[\hat{b}^\dagger_{(s,m)[\mathrm{H}]}, \hat{n}_{(r,l)[\mathrm{H}]}\right] = -\hat{b}^\dagger_{(s,m)[\mathrm{H}]}\delta_{sr}\delta_{lm}\,. \tag{B.6}$$

Calculating the commutator $\left[\hat{H}'_{\mathrm{HBH},[\mathrm{H}]}, \hat{n}_{(r,l)[\mathrm{H}]}\right]$, we see that only terms (1) and (2) of equation (B.1) are relevant, since the last term commutes with $\hat{n}_{(r,l)[\mathrm{H}]}$. Furthermore, the commutator also vanishes for any term that does not contain at least one factor with the indices (r,l). This allows us to simplify the expression to obtain:

$$-\frac{1}{J}\left[(1), \hat{n}_{(r,l)[\mathrm{H}]}\right] = \left(-\hat{b}^\dagger_{(r,l)[\mathrm{H}]}\hat{b}_{(r+1,l)[\mathrm{H}]} + \mathrm{h.c.}\right) + \left(\hat{b}^\dagger_{(r-1,l)[\mathrm{H}]}\hat{b}_{(r,l)[\mathrm{H}]} - \mathrm{h.c.}\right)\,, \tag{B.7}$$

$$-\frac{1}{J_\perp}\left[(2), \hat{n}_{(r,l)[\mathrm{H}]}\right] = \left(-e^{-ir\varphi}\cdot\hat{b}^\dagger_{(r,l)[\mathrm{H}]}\hat{b}_{(r,l+1)[\mathrm{H}]} + \mathrm{h.c.}\right) + \left(e^{-ir\varphi}\cdot\hat{b}^\dagger_{(r,l-1)[\mathrm{H}]}\hat{b}_{(r,l)[\mathrm{H}]} - \mathrm{h.c.}\right)\,. \tag{B.8}$$

Substituting Terms Since the position $\mathbf{x} = (r,l)$ is generally independent of time t, it follows that:

$$\frac{\mathrm{d}}{\mathrm{d}t}\hat{n}_{(r,l)[\mathrm{H}]} = \frac{\partial}{\partial t}\hat{n}_{(r,l)[\mathrm{H}]}\,, \tag{B.9}$$

and we can replace the first term in (B.4) with the LHS of (B.5). Substituting (B.7) and (B.8) back into the RHS of (B.5), we obtain:

$$\begin{aligned}\frac{\mathrm{d}}{\mathrm{d}t}\hat{n}_{(r,l)[\mathrm{H}]} = {}& \frac{iJ}{\hbar}\left[\left(\hat{b}^\dagger_{(r,l)[\mathrm{H}]}\hat{b}_{(r+1,l)[\mathrm{H}]} - \mathrm{h.c.}\right) - \left(\hat{b}^\dagger_{(r-1,l)[\mathrm{H}]}\hat{b}_{(r,l)[\mathrm{H}]} - \mathrm{h.c.}\right)\right] \\ & + \frac{iJ_\perp}{\hbar}\left[\left(e^{-ir\varphi}\cdot\hat{b}^\dagger_{(r,l)[\mathrm{H}]}\hat{b}_{(r,l+1)[\mathrm{H}]} - \mathrm{h.c.}\right) - \left(e^{-ir\varphi}\cdot\hat{b}^\dagger_{(r,l-1)[\mathrm{H}]}\hat{b}_{(r,l)[\mathrm{H}]} - \mathrm{h.c.}\right)\right]\end{aligned} \tag{B.10}$$

$$\stackrel{!}{=} -\hat{j}_{\text{leg: }(r+1,l)[\mathrm{H}]} + \hat{j}_{\text{leg: }(r,l)[\mathrm{H}]} - \hat{j}_{\text{rung: }(r,l+1)[\mathrm{H}]} + \hat{j}_{\text{rung: }(r,l)[\mathrm{H}]} \tag{B.11}$$

We now set $\hbar = 1$ and assign each term in (B.11) to its corresponding term in (B.10). Based on the creation/annihilation operators that make up each term in the definition of the current operators, we can also deduce which pair of sites the current is defined between:

$$\hat{j}_{\text{leg: }(r+1,l)\langle\leftrightarrow(r,l)\rangle[\mathrm{H}]} = -iJ\left[\hat{b}^\dagger_{(r,l)[\mathrm{H}]}\hat{b}_{(r+1,l)[\mathrm{H}]} - \mathrm{h.c.}\right]\,, \tag{B.12}$$

$$\hat{j}_{\text{rung: }(r,l+1)\langle\leftrightarrow(r,l)\rangle[\mathrm{H}]} = -iJ_\perp\left[e^{-ir\varphi}\cdot\hat{b}^\dagger_{(r,l)[\mathrm{H}]}\hat{b}_{(r,l+1)[\mathrm{H}]} - \mathrm{h.c.}\right]\,. \tag{B.13}$$

Now, we adopt a current direction convention that differs from many publications, following instead that used by Buser [24], and set the current direction in the above definitions to be $(r+1,l) \to (r,l)$ and $(r,l+1) \to (r,l)$ respectively. This choice has the advantage of yielding a positive expression where the $\hat{b}^\dagger_{(r,l)}$ term appears first.

As such, we may reverse the direction of the currents above and drop the $[\mathrm{H}]$ subscript (since their functional form remains the same in both pictures) to obtain our definitions of the particle currents:

$$\hat{j}_{\text{leg: }(r,l)\to(r+1,l)} = iJ\left[\hat{b}^\dagger_{(r,l)}\hat{b}_{(r+1,l)} - \text{h.c.}\right] , \tag{B.14}$$

$$\hat{j}_{\text{rung: }(r,l)\to(r,l+1)} = iJ_\perp\left[e^{-ir\varphi}\cdot\hat{b}^\dagger_{(r,l)}\hat{b}_{(r,l+1)} - \text{h.c.}\right] . \tag{B.15}$$

The convention corresponding to this definition is illustrated in Figure B.1.

Appendix C

Additional Calculations: Current Measurement Protocol with Soft-Core Bosons

In section 2.3, we explored the fact that the bosonic commutation relations do not hold for soft-core bosons. At the same time, we saw in section 2.4 that commutators play a significant role in the derivation of the current measurement protocol. This appendix acts as a continuation of the last part of the above-mentioned section and document some additional computer-assisted calculations.

First, let us recap some key definitions. With finite dimensions, the commutation relation for the creation and annihilation operators for some site q is:

$$[\hat{b}_q, \hat{b}_q^\dagger] = \hat{\mathbb{1}} + \hat{\delta}_q \qquad \text{where} \qquad \hat{\delta}_q = -(M+1)\,|M\rangle_q\langle M|_q \ , \tag{C.1}$$

as defined in (2.33). We assume that a double well of sites k and l has a tight-binding Hamiltonian (i.e. no on-site interactions):

$$\hat{H}_{\text{hop}} = -\left(\tilde{J}\,\hat{b}_k^\dagger \hat{b}_l + \text{h.c.}\right) = i|\tilde{J}|\,\left(\hat{b}_\rightarrow^\dagger \hat{b}_\leftarrow - \hat{b}_\leftarrow^\dagger \hat{b}_\rightarrow\right) \ , \tag{C.2}$$

where $\tilde{J}$ is some possibly-complex hopping amplitude between the two sites, and $\hat{b}_\rightarrow$ and $\hat{b}_\leftarrow$ are the annihilation operators of the current operator

$$\hat{j}_{k\to l} = i\left[\tilde{J}\,\hat{b}_k^\dagger \hat{b}_l - \tilde{J}^* \hat{b}_l^\dagger \hat{b}_k\right] = |\tilde{J}|\left(\hat{b}_\rightarrow^\dagger \hat{b}_\rightarrow - \hat{b}_\leftarrow^\dagger \hat{b}_\leftarrow\right) \ . \tag{C.3}$$

Under this Hamiltonian, we may calculate the time evolution of our operators $\hat{b}_{\rightarrow/\leftarrow}$ using the Heisenberg equation of motion. The additional error term $\hat{\delta}_q$, $q \in \{k, l\}$ in the bosonic commutator results in a set of coupled first-order differential equations (2.52) that cannot be easily decoupled:

$$\frac{\mathrm{d}}{\mathrm{d}t}\hat{b}_{\rightarrow/\leftarrow} = \frac{i}{\hbar}\left[\hat{H}_{\text{hop}}, \hat{b}_{\rightarrow/\leftarrow}\right] = -\frac{|\tilde{J}|}{\hbar}\left[\pm\frac{\hat{\delta}_l - \hat{\delta}_k}{2}\hat{b}_{\rightarrow/\leftarrow} \mp \left(\hat{\mathbb{1}} + \frac{\hat{\delta}_l + \hat{\delta}_k}{2}\right)\hat{b}_{\leftarrow/\rightarrow}\right] \ , \tag{C.4}$$

While we were already able to draw our conclusions from this result, we can go a step further and use computer-assisted calculations to solve our system. Using Mathematica [89], we obtain the following solution:

$$\hat{b}_{\rightarrow}(t) = \frac{e^{-iKt\hat{A}}}{4\hat{A}}\left[i\left(e^{2iKt\hat{A}} - \hat{\mathbb{1}}\right)\left(\hat{\delta}_l - \hat{\delta}_k\right) + 2\hat{A}\left(e^{2iKt\hat{A}} + \hat{\mathbb{1}}\right)\right]\cdot\hat{b}_{\rightarrow}(0) - \frac{ie^{-iKt\hat{A}}\left(e^{2iKt\hat{A}} - \hat{\mathbb{1}}\right)(2 + \hat{\delta}_l + \hat{\delta}_k)}{4\hat{A}}\cdot\hat{b}_{\leftarrow}(0), \tag{C.5}$$

$$\hat{b}_{\leftarrow}(t) = \frac{ie^{-iKt\hat{A}}\left(e^{2iKt\hat{A}} - \hat{\mathbb{1}}\right)(2 + \hat{\delta}_l + \hat{\delta}_k)}{4\hat{A}}\cdot\hat{b}_{\rightarrow}(0) + \frac{e^{-iKt\hat{A}}}{4\hat{A}}\left[i\left(\hat{\mathbb{1}} - e^{2iKt\hat{A}}\right)\left(\hat{\delta}_l - \hat{\delta}_k\right) + 2\hat{A}\left(e^{2iKt\hat{A}} + \hat{\mathbb{1}}\right)\right]\cdot\hat{b}_{\leftarrow}(0)\ , \tag{C.6}$$

where $K = \frac{|\tilde{J}|}{\hbar}$ and $\hat{A} = \sqrt{(\hat{\mathbb{1}} + \hat{\delta}_l)(\hat{\mathbb{1}} + \hat{\delta}_k)}$.

Here, it is important to point out that in general,

$$\left[\hat{\delta}_q, \hat{b}_{\rightarrow/\leftarrow}\right] \neq 0 \ \text{ for } \ q \in \{\, k, l \,\}\ . \tag{C.7}$$

Unfortunately, Mathematica could not solve the ODE if we use the operator ** (non-commutative multiply) in place of the operator * (commutative multiply) between $\hat{\delta}_q$ and $\hat{b}_{\rightarrow/\leftarrow}$. Nevertheless, intuition suggests that this result remains correct: the coefficients are always to the left of the variables $\hat{b}_{\rightarrow/\leftarrow}$, and the coefficients commute within themselves. More verification is however required to understand the effects of the non-commutativity on the solution of this set of coupled differential equations.

Since $(\hat{\mathbb{1}} + \hat{\delta}_l)(\hat{\mathbb{1}} + \hat{\delta}_k)$ is diagonal with all (and only) its diagonal elements being non-zero, its square-root $\hat{A}$ is well-defined by taking the square-root along the diagonal elements. As such, the inverse (written here as $1/\hat{A}$) is also well-defined. In all cases, $\hat{A}$ is diagonal, and $[\hat{A}, \hat{b}_k] = [\hat{A}, \hat{b}_l] = 0$.

Due to the complexity of the algebraic expressions and the need to take into account trigonometric identities, we may leverage the Large Language Model (LLM) DeepSeek (DeepThink R1) [90] to simplify the above expressions, obtaining:

$$\hat{b}_{\rightarrow}(t) = \left(\cos\left(Kt\hat{A}\right) - \frac{\hat{\delta}_l - \hat{\delta}_k}{2\hat{A}}\sin\left(Kt\hat{A}\right)\right)\hat{b}_{\rightarrow}(0) + \left(\frac{2\hat{\mathbb{1}} + \hat{\delta}_l + \hat{\delta}_k}{2\hat{A}}\sin\left(Kt\hat{A}\right)\right)\hat{b}_{\leftarrow}(0) \tag{C.8}$$

$$\hat{b}_{\leftarrow}(t) = \left(-\frac{2\hat{\mathbb{1}} + \hat{\delta}_l + \hat{\delta}_k}{2\hat{A}}\sin\left(Kt\hat{A}\right)\right)\hat{b}_{\rightarrow}(0) + \left(\cos\left(Kt\hat{A}\right) + \frac{\hat{\delta}_l - \hat{\delta}_k}{2\hat{A}}\sin\left(Kt\hat{A}\right)\right)\hat{b}_{\leftarrow}(0) \tag{C.9}$$

We can now substitute (C.8) and (C.9) into (2.41) to understand the effect of the error term $\hat{\delta}$ on the current measurement protocol. However, since $[\hat{\delta}_q, \hat{b}_{\rightarrow/\leftarrow}] \neq 0$ for $q \in \{ k, l \}$, simplification of the expression is non-trivial.

For future work, we could employ numerical methods to simulate the dynamics and then compare it with the analytical results presented above from Mathematica to empirically check if the dynamics are correctly described by the symbolic expressions. Alternatively, we could employ more advanced analytical techniques to solve for the differential equations. If the above results prove to be correct, then it might be helpful to calculate the resultant evolution $\left(\hat{n}_k(t) - \hat{n}_l(t)\right)$ and understand whether it is possible to measure the current $\hat{j}_{k\rightarrow l}$ in the presence of the error term $\hat{\delta}_q$.

Appendix D

Complete Results: Evolution of Current Operator Eigenstates in a Double Well

In this appendix, we simply document the full results from the double-well analysis for soft-core bosons performed in Figure 5.4, including those already included in the main text. Please refer to section 5.2 for interpretation of the main results.

Maximum Occupation per Site $M = 2$

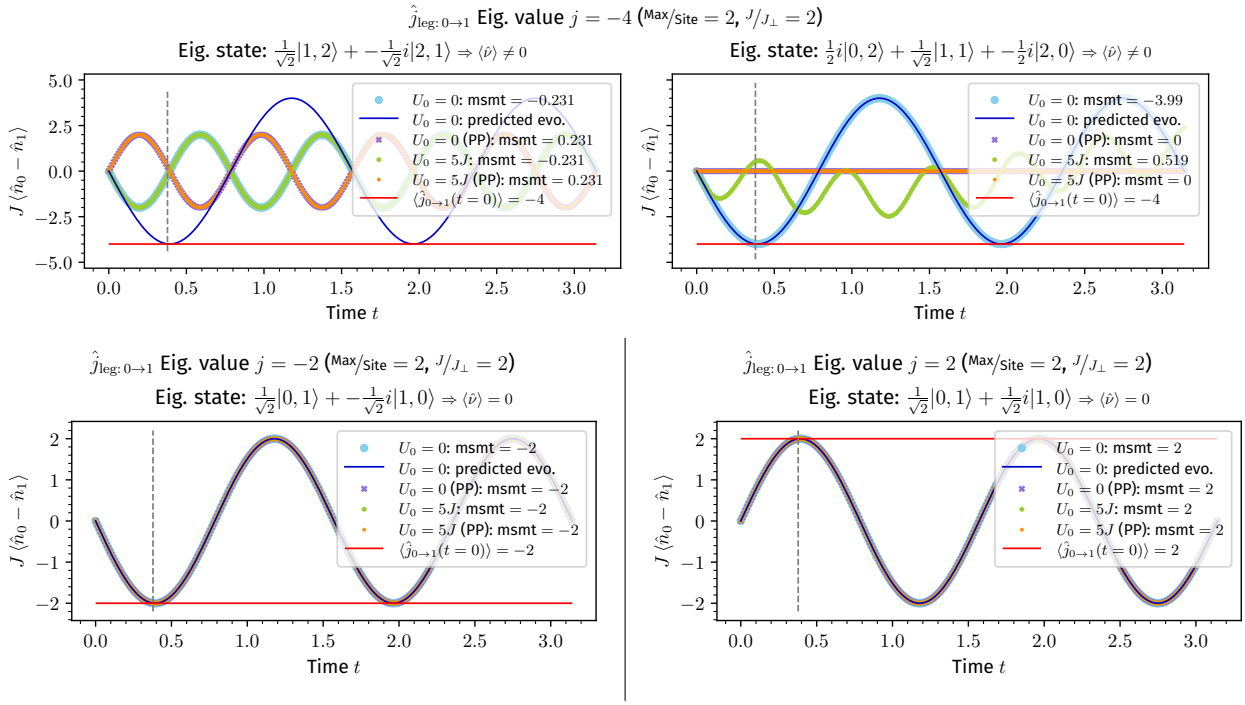

$\hat{j}_{\text{leg: }0\to1}$ Eig. value $j = 0$ (Max/Site $= 2$, $J/J_\perp = 2$)

Eig. state: $\frac{1}{\sqrt{2}}|0,2\rangle + \frac{1}{\sqrt{2}}|2,0\rangle \Rightarrow \langle\hat{\nu}\rangle \neq 0$

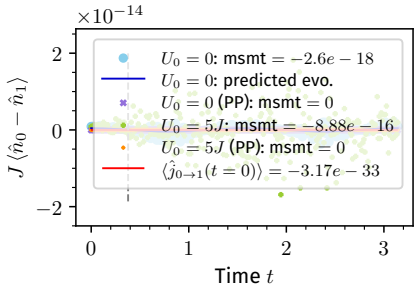

Eig. state: $|0,0\rangle \Rightarrow \langle\hat{\nu}\rangle = 0$

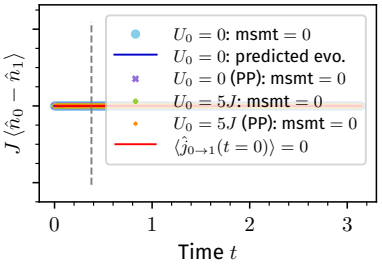

Eig. state: $|2,2\rangle \Rightarrow \langle\hat{\nu}\rangle \neq 0$

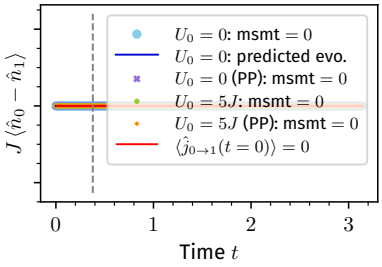

$\hat{j}_{\text{leg: }0\to1}$ Eig. value $j = 4$ (Max/Site $= 2$, $J/J_\perp = 2$)

Eig. state: $\frac{1}{\sqrt{2}}|1,2\rangle + \frac{1}{\sqrt{2}}i|2,1\rangle \Rightarrow \langle\hat{\nu}\rangle \neq 0$

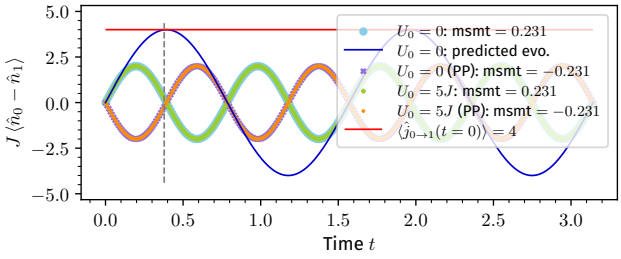

Eig. state: $-\frac{1}{2}i|0,2\rangle + \frac{1}{\sqrt{2}}|1,1\rangle + \frac{1}{2}i|2,0\rangle \Rightarrow \langle\hat{\nu}\rangle \neq 0$

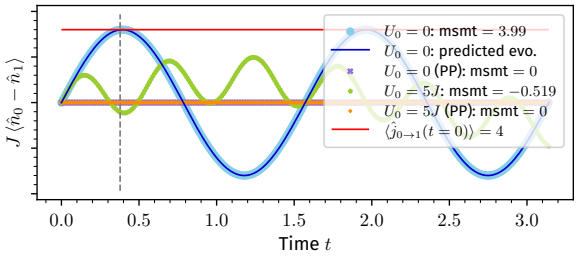

Maximum Occupation per Site $M = 3$

$\hat{j}_{\text{leg: }0\to1}$ Eig. value $j = -\sqrt{48}$ (Max/Site $= 3$, $J/J_\perp = 2$)

Eig. state: $\frac{1}{2}i|1,3\rangle + \frac{1}{\sqrt{2}}|2,2\rangle + -\frac{1}{2}i|3,1\rangle \Rightarrow \langle\hat{\nu}\rangle \neq 0$

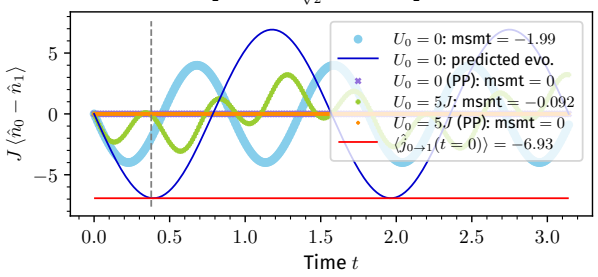

$\hat{j}_{\text{leg: }0\to1}$ Eig. value $j = \sqrt{48}$ (Max/Site $= 3$, $J/J_\perp = 2$)

Eig. state: $-\frac{1}{2}i|1,3\rangle + \frac{1}{\sqrt{2}}|2,2\rangle + \frac{1}{2}i|3,1\rangle \Rightarrow \langle\hat{\nu}\rangle \neq 0$

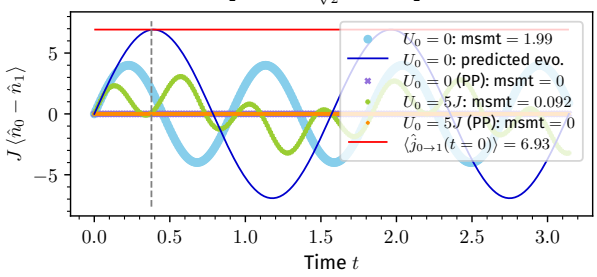

$\hat{j}_{\text{leg: }0\to1}$ Eig. value $j = -6$ (Max/Site $= 3$, $J/J_\perp = 2$)

Eig. state: $\frac{1}{\sqrt{2}}|2,3\rangle + -\frac{1}{\sqrt{2}}i|3,2\rangle \Rightarrow \langle\hat{\nu}\rangle \neq 0$

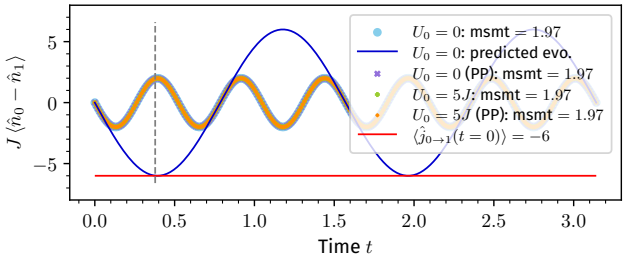

Eig. state: $\frac{1}{\sqrt{8}}i|0,3\rangle + \sqrt{\frac{3}{8}}|1,2\rangle + -\sqrt{\frac{3}{8}}i|2,1\rangle + -\frac{1}{\sqrt{8}}|3,0\rangle \Rightarrow \langle\hat{\nu}\rangle \neq 0$

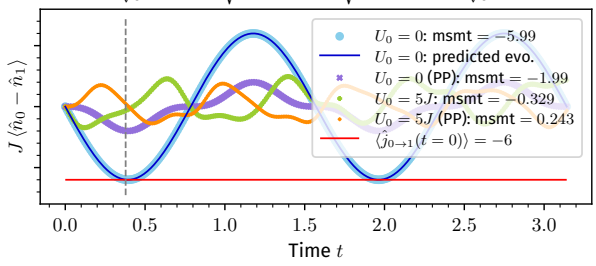

$\hat{j}_{\text{leg: }0\to1}$ Eig. value $j=-4$ ($^{\text{Max}}/_{\text{Site}}=3$, $^{J}/_{J_\perp}=2$)

Eig. state: $\frac{1}{2}i|0,2\rangle+\frac{1}{\sqrt{2}}|1,1\rangle+-\frac{1}{2}i|2,0\rangle \Rightarrow \langle\dot{\nu}\rangle=0$

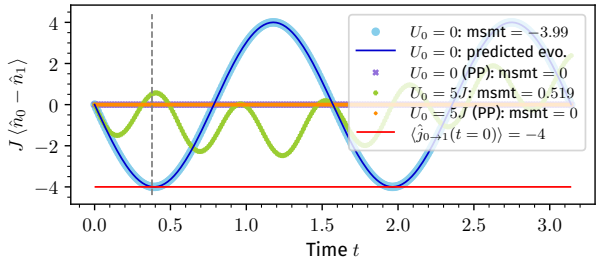

$\hat{j}_{\text{leg: }0\to1}$ Eig. value $j=4$ ($^{\text{Max}}/_{\text{Site}}=3$, $^{J}/_{J_\perp}=2$)

Eig. state: $-\frac{1}{2}i|0,2\rangle+\frac{1}{\sqrt{2}}|1,1\rangle+\frac{1}{2}i|2,0\rangle \Rightarrow \langle\dot{\nu}\rangle=0$

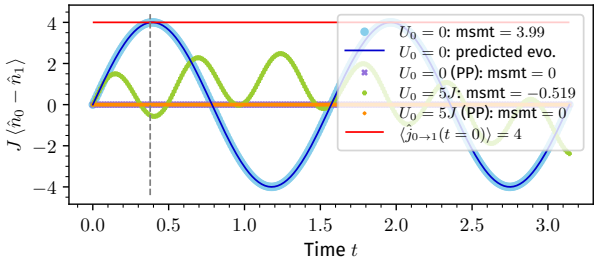

$\hat{j}_{\text{leg: }0\to1}$ Eig. value $j=-2$ ($^{\text{Max}}/_{\text{Site}}=3$, $^{J}/_{J_\perp}=2$)

Eig. state: $\frac{1}{\sqrt{2}}i|0,1\rangle+\frac{1}{\sqrt{2}}|1,0\rangle \Rightarrow \langle\dot{\nu}\rangle=0$

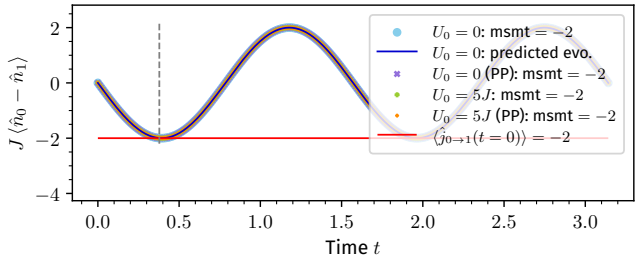

Eig. state: $\sqrt{\frac{3}{8}}i|0,3\rangle+\frac{1}{\sqrt{8}}|1,2\rangle+\frac{1}{\sqrt{8}}i|2,1\rangle+\sqrt{\frac{3}{8}}|3,0\rangle \Rightarrow \langle\dot{\nu}\rangle\neq0$

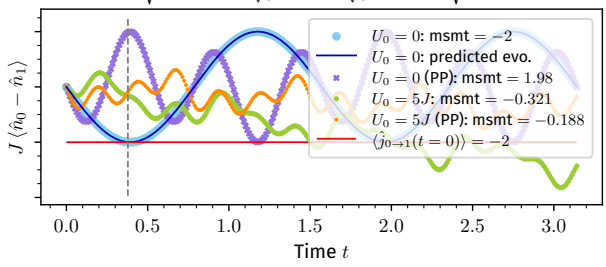

$\hat{j}_{\text{leg: }0\to1}$ Eig. value $j=0$ ($^{\text{Max}}/_{\text{Site}}=3$, $^{J}/_{J_\perp}=2$)

Eig. state: $\frac{1}{\sqrt{2}}|0,2\rangle+\frac{1}{\sqrt{2}}|2,0\rangle \Rightarrow \langle\dot{\nu}\rangle=0$

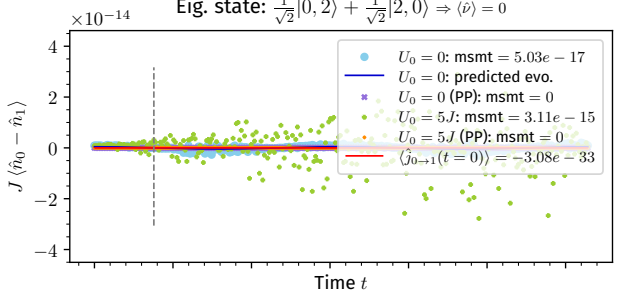

Eig. state: $|0,0\rangle \Rightarrow \langle\dot{\nu}\rangle=0$

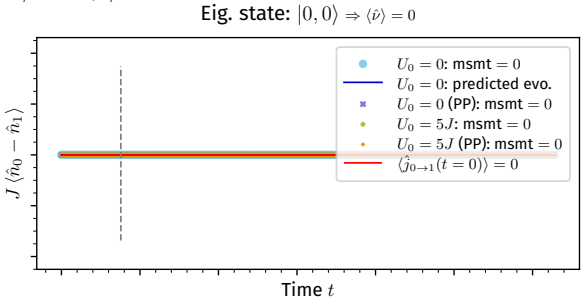

Eig. state: $|3,3\rangle \Rightarrow \langle\dot{\nu}\rangle\neq0$

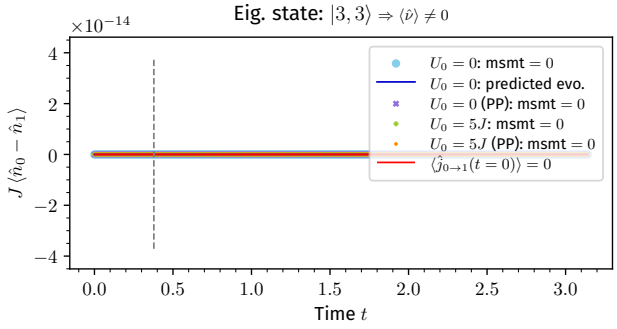

Eig. state: $\frac{1}{\sqrt{2}}|1,3\rangle+\frac{1}{\sqrt{2}}|3,1\rangle \Rightarrow \langle\dot{\nu}\rangle\neq0$

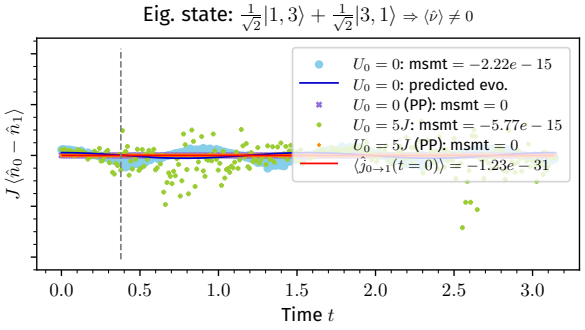

$\hat{j}_{\text{leg: }0\to1}$ Eig. value $j = 2$ ($^{\text{Max}}/_{\text{Site}} = 3$, $^{J}/_{J_\perp} = 2$)

Eig. state: $-\sqrt{\frac{3}{8}}i|0,3\rangle + \frac{1}{\sqrt{8}}|1,2\rangle + -\frac{1}{\sqrt{8}}i|2,1\rangle + \sqrt{\frac{3}{8}}|3,0\rangle \Rightarrow \langle\hat{\nu}\rangle \neq 0$

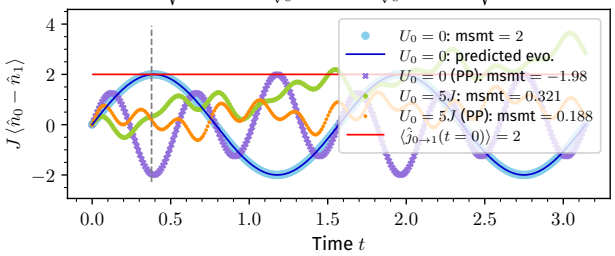

Eig. state: $-\frac{1}{\sqrt{2}}i|0,1\rangle + \frac{1}{\sqrt{2}}|1,0\rangle \Rightarrow \langle\hat{\nu}\rangle = 0$

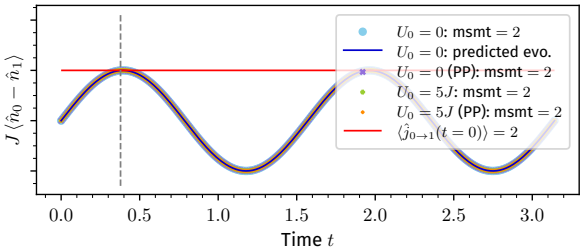

$\hat{j}_{\text{leg: }0\to1}$ Eig. value $j = 6$ ($^{\text{Max}}/_{\text{Site}} = 3$, $^{J}/_{J_\perp} = 2$)

Eig. state: $\frac{1}{\sqrt{2}}|2,3\rangle + \frac{1}{\sqrt{2}}i|3,2\rangle \Rightarrow \langle\hat{\nu}\rangle \neq 0$

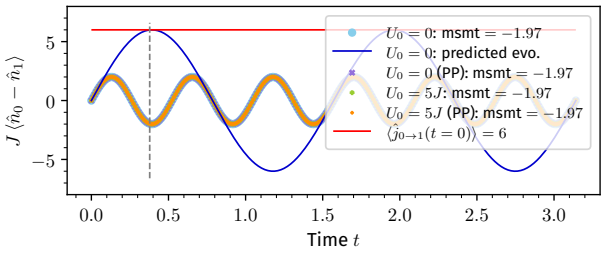

Eig. state: $-\frac{1}{\sqrt{8}}|0,3\rangle + -\sqrt{\frac{3}{8}}i|1,2\rangle + \sqrt{\frac{3}{8}}|2,1\rangle + \frac{1}{\sqrt{8}}i|3,0\rangle \Rightarrow \langle\hat{\nu}\rangle \neq 0$

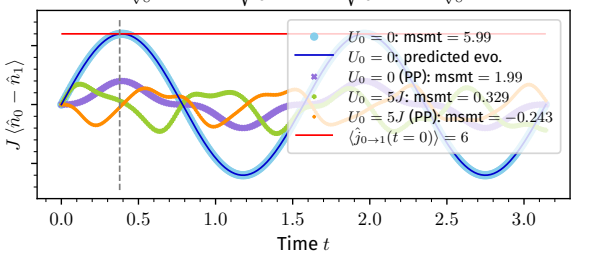

Maximum Occupation per Site $M = 4$

$\hat{j}_{\text{leg: }0\to1}$ Eig. value $j = -\sqrt{96}$ ($^{\text{Max}}/_{\text{Site}} = 4$, $^{J}/_{J_\perp} = 2$)

Eig. state: $\frac{1}{2}i|2,4\rangle + \frac{1}{\sqrt{2}}|3,3\rangle + -\frac{1}{2}i|4,2\rangle \Rightarrow \langle\hat{\nu}\rangle \neq 0$

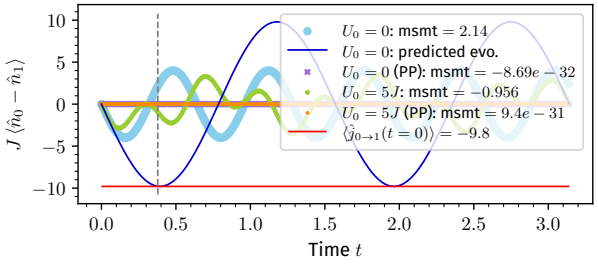

$\hat{j}_{\text{leg: }0\to1}$ Eig. value $j = \sqrt{96}$ ($^{\text{Max}}/_{\text{Site}} = 4$, $^{J}/_{J_\perp} = 2$)

Eig. state: $-\frac{1}{2}i|2,4\rangle + \frac{1}{\sqrt{2}}|3,3\rangle + \frac{1}{2}i|4,2\rangle \Rightarrow \langle\hat{\nu}\rangle \neq 0$

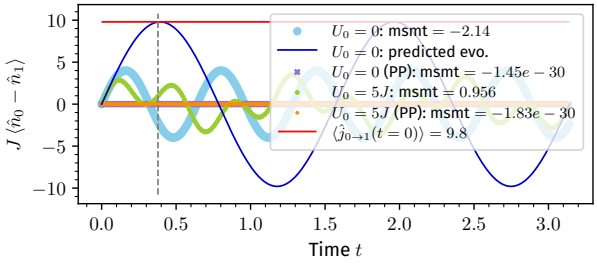

$\hat{j}_{\text{leg: }0\to1}$ Eig. value $j = -9.40312$ ($^{\text{Max}}/_{\text{Site}} = 4$, $^{J}/_{J_\perp} = 2$)

Eig. state: $0.36451i|1,4\rangle + 0.60591|2,3\rangle + -0.60591i|3,2\rangle + -0.36451|4,1\rangle \Rightarrow \langle\hat{\nu}\rangle \neq 0$

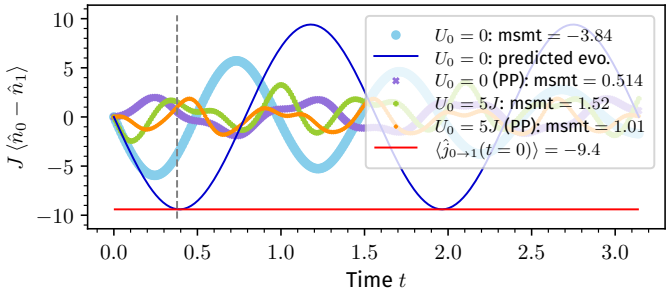

$\hat{j}_{\text{leg: }0\to1}$ Eig. value $j = 9.40312$ (Max/Site $= 4$, $J/J_\perp = 2$)

Eig. state: $-0.36451|1,4\rangle + -0.60591i|2,3\rangle + 0.60591|3,2\rangle + 0.36451i|4,1\rangle \Rightarrow \langle\hat{\nu}\rangle \neq 0$

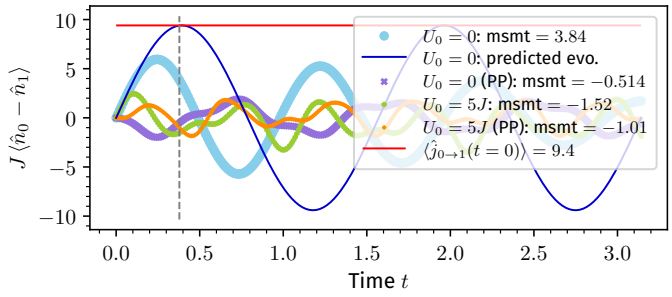

$\hat{j}_{\text{leg: }0\to1}$ Eig. value $j = -8$ (Max/Site $= 4$, $J/J_\perp = 2$)

Eig. state: $\frac{1}{\sqrt{2}}i|3,4\rangle + \frac{1}{\sqrt{2}}|4,3\rangle \Rightarrow \langle\hat{\nu}\rangle \neq 0$

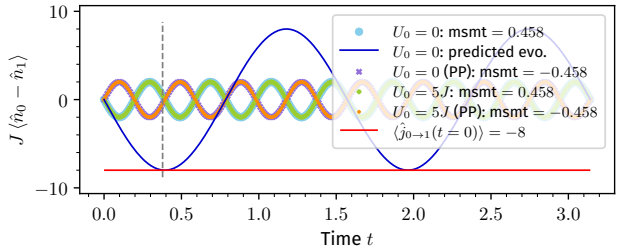

Eig. state: $-\frac{1}{4}|0,4\rangle + \frac{1}{2}i|1,3\rangle + \sqrt{\frac{3}{8}}|2,2\rangle + -\frac{1}{2}i|3,1\rangle + -\frac{1}{4}|4,0\rangle \Rightarrow \langle\hat{\nu}\rangle \neq 0$

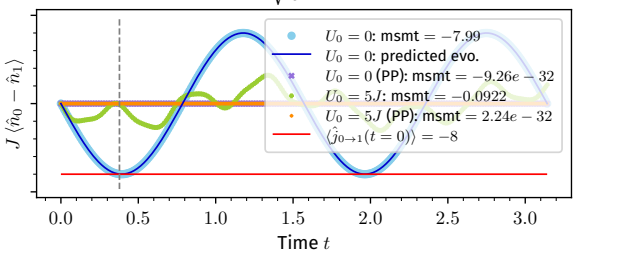

$\hat{j}_{\text{leg: }0\to1}$ Eig. value $j = -6$ (Max/Site $= 4$, $J/J_\perp = 2$)

Eig. state: $-\frac{1}{\sqrt{8}}|0,3\rangle + \sqrt{\frac{3}{8}}i|1,2\rangle + \sqrt{\frac{3}{8}}|2,1\rangle + -\frac{1}{\sqrt{8}}i|3,0\rangle \Rightarrow \langle\hat{\nu}\rangle = 0$

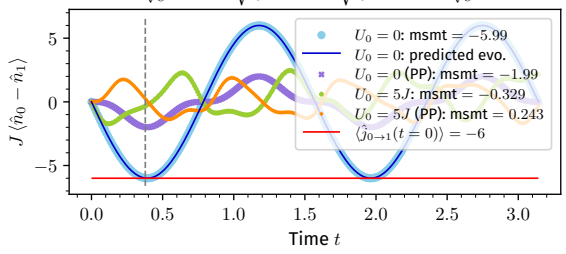

$\hat{j}_{\text{leg: }0\to1}$ Eig. value $j = 6$ (Max/Site $= 4$, $J/J_\perp = 2$)

Eig. state: $-\frac{1}{\sqrt{8}}i|0,3\rangle + \sqrt{\frac{3}{8}}|1,2\rangle + \sqrt{\frac{3}{8}}i|2,1\rangle + -\frac{1}{\sqrt{8}}|3,0\rangle \Rightarrow \langle\hat{\nu}\rangle = 0$

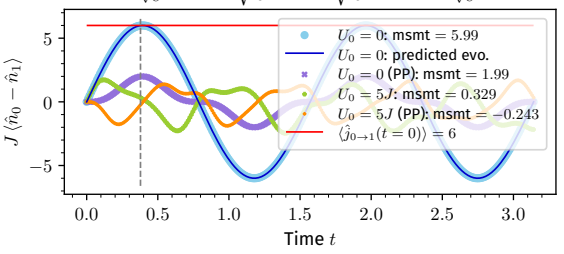

$\hat{j}_{\text{leg: }0\to1}$ Eig. value $j = -4$ (Max/Site $= 4$, $J/J_\perp = 2$)

Eig. state: $-\frac{1}{2}|0,4\rangle + \frac{1}{2}i|1,3\rangle + \frac{1}{2}i|3,1\rangle + \frac{1}{2}|4,0\rangle \Rightarrow \langle\hat{\nu}\rangle \neq 0$

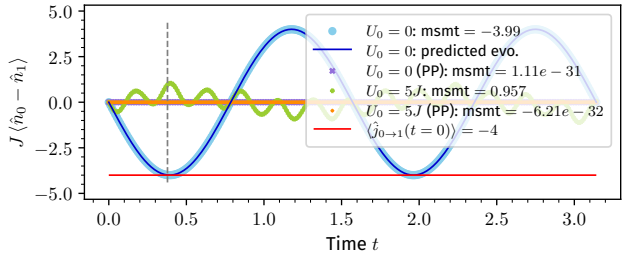

Eig. state: $\frac{1}{2}i|0,2\rangle + \frac{1}{\sqrt{2}}|1,1\rangle + -\frac{1}{2}i|2,0\rangle \Rightarrow \langle\hat{\nu}\rangle = 0$

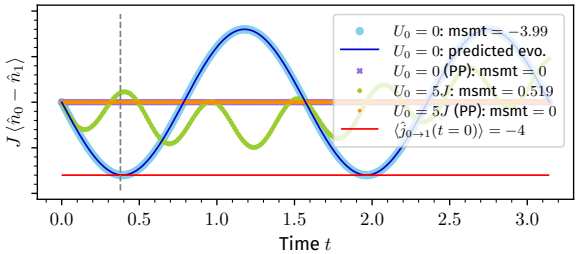

$\hat{j}_{\text{leg: }0\to1}$ Eig. value $j = -3.40312$ ($^{\text{Max}}/_{\text{Site}} = 4$, $^{J}/_{J_\perp} = 2$)

Eig. state: $0.60591|1,4\rangle + -0.36451i|2,3\rangle + 0.36451|3,2\rangle + -0.60591i|4,1\rangle \Rightarrow \langle\hat{\nu}\rangle \neq 0$

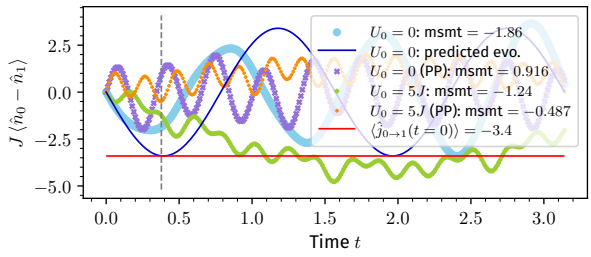

$\hat{j}_{\text{leg: }0\to1}$ Eig. value $j = 3.40312$ ($^{\text{Max}}/_{\text{Site}} = 4$, $^{J}/_{J_\perp} = 2$)

Eig. state: $0.60591|1,4\rangle + 0.36451i|2,3\rangle + 0.36451|3,2\rangle + 0.60591i|4,1\rangle \Rightarrow \langle\hat{\nu}\rangle \neq 0$

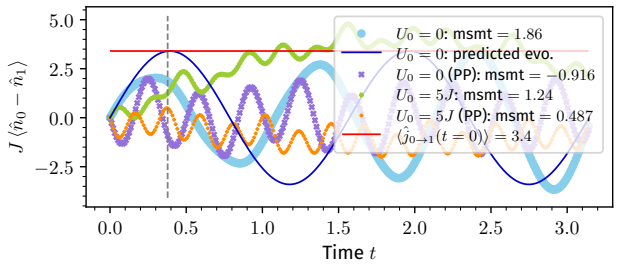

$\hat{j}_{\text{leg: }0\to1}$ Eig. value $j = -2$ ($^{\text{Max}}/_{\text{Site}} = 4$, $^{J}/_{J_\perp} = 2$)

Eig. state: $\frac{1}{\sqrt{2}}i|0,1\rangle + \frac{1}{\sqrt{2}}|1,0\rangle \Rightarrow \langle\hat{\nu}\rangle = 0$

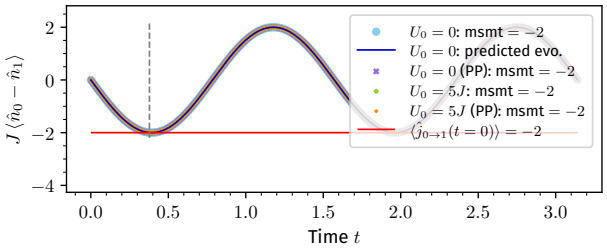

Eig. state: $\sqrt{\frac{3}{8}}|0,3\rangle + -\frac{1}{\sqrt{8}}i|1,2\rangle + \frac{1}{\sqrt{8}}|2,1\rangle + -\sqrt{\frac{3}{8}}i|3,0\rangle \Rightarrow \langle\hat{\nu}\rangle = 0$

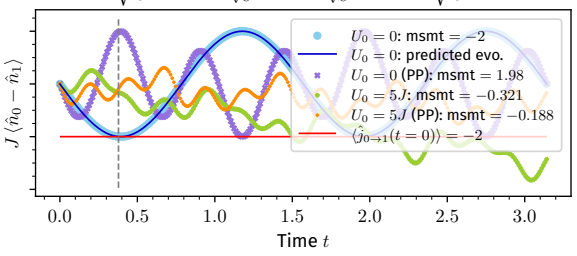

Note: here we skip the results for the eigenvalue $j = 0$ as there are five eigenstates, all of which did not evolve in time.

$\hat{j}_{\text{leg: }0\to1}$ Eig. value $j = 2$ ($^{\text{Max}}/_{\text{Site}} = 4$, $^{J}/_{J_\perp} = 2$)

Eig. state: $\sqrt{\frac{3}{8}}|0,3\rangle + \frac{1}{\sqrt{8}}i|1,2\rangle + \frac{1}{\sqrt{8}}|2,1\rangle + \sqrt{\frac{3}{8}}i|3,0\rangle \Rightarrow \langle\hat{\nu}\rangle = 0$

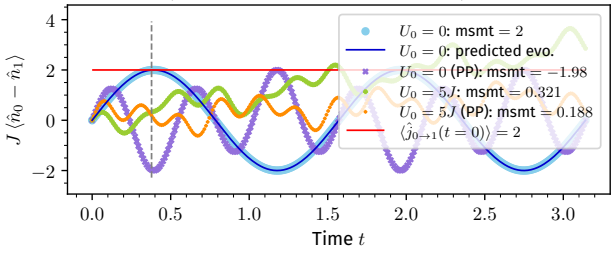

Eig. state: $-\frac{1}{\sqrt{2}}i|0,1\rangle + \frac{1}{\sqrt{2}}|1,0\rangle \Rightarrow \langle\hat{\nu}\rangle = 0$

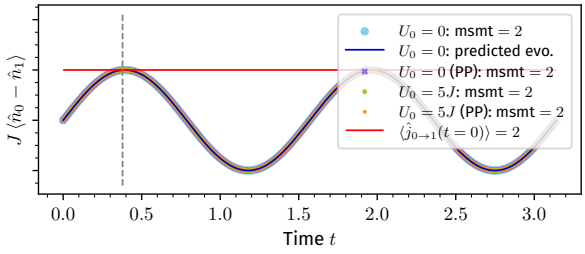

$\hat{j}_{\text{leg: } 0\to 1}$ Eig. value $j = 4$ ($^{\text{Max}}/_{\text{Site}} = 4$, $^{J}/_{J_\perp} = 2$)

Eig. state: $-\frac{1}{2}i|0,2\rangle + \frac{1}{\sqrt{2}}|1,1\rangle + \frac{1}{2}i|2,0\rangle \Rightarrow \langle\hat{\nu}\rangle = 0$

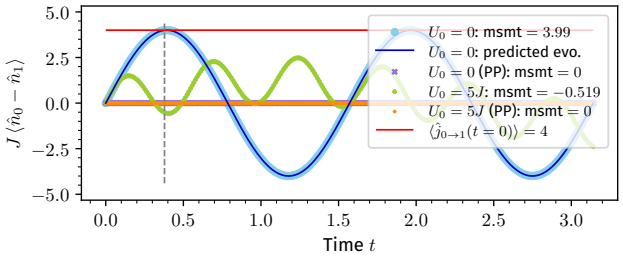

Eig. state: $-\frac{1}{2}i|0,4\rangle + \frac{1}{2}|1,3\rangle + \frac{1}{2}|3,1\rangle + \frac{1}{2}i|4,0\rangle \Rightarrow \langle\hat{\nu}\rangle \neq 0$

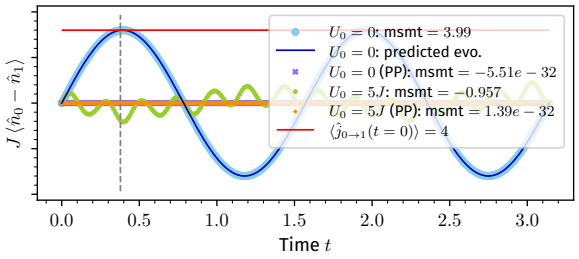

$\hat{j}_{\text{leg: } 0\to 1}$ Eig. value $j = 8$ ($^{\text{Max}}/_{\text{Site}} = 4$, $^{J}/_{J_\perp} = 2$)

Eig. state: $-\frac{1}{4}|0,4\rangle + -\frac{1}{2}i|1,3\rangle + \sqrt{\frac{3}{8}}|2,2\rangle + \frac{1}{2}i|3,1\rangle + -\frac{1}{4}|4,0\rangle \Rightarrow \langle\hat{\nu}\rangle \neq 0$

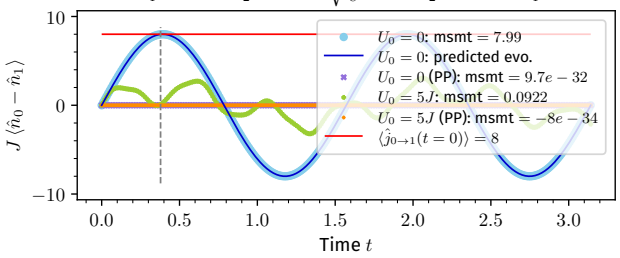

Eig. state: $-\frac{1}{\sqrt{2}}i|3,4\rangle + \frac{1}{\sqrt{2}}|4,3\rangle \Rightarrow \langle\hat{\nu}\rangle \neq 0$

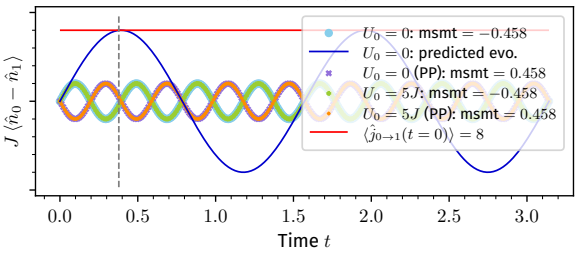

Appendix E

Generating Occupations for a Fixed-N Subspace

As we have previously explored in subsection 4.4.1, it is useful and important to be able to work in a fixed-N subspace, especially since the flux ladder Hamiltonian conserves the number of particles N. This not just greatly increases the efficiency of our code and allows us to reach larger system sizes purely with exact diagonalisation (ED), but also allows us to easily simulate the experimental condition where the number of particles in the system is fixed.

Let the system that we are interested in have G sites, each with a maximum occupation of M. Then, we can create the transformation matrix T of N-particle basis states as described in subsection 4.4.1. To generate the N-particle basis states, we build up occupation arrays by traversing a pruned $(M+1)$-ary tree of depth $G+1$, with the vacuum state $|\varnothing\rangle$ as the root. Each node at depth $k+1$ corresponds to a partial occupation array $[n_0, n_1, \ldots, n_{k-1}]$ for the first k sites, and has $(M+1)$ children corresponding to occupation values 0 to M for the next site k. As such, each path down the tree represents a possible occupation configuration of the system's G sites. By doing a breadth-first traversal, we can prune the tree when the cumulative particle count along a path exceeds N, or when N particles are reached (even if sites remain). Each valid path is saved as an array and right-padded with zeros if the depth of the path is less than G. This results in a list of arrays, each representing a valid occupation configuration with exactly N particles. We then convert these occupation arrays to Fock states using the `get_fock_state(occupations)` method described in section 4.4, which returns the corresponding state array.

This is a modification of the well-established multi-ary tree for combinatorics [91]. A minimum working example in Python is provided in source code E.1.

To check if we have generated the correct number of basis states, we calculate the expected number of basis states as a classic problem of stars and bars [91], but with a constraint on the maximum occupancy. As such, this problem can be mapped to that of finding the coefficient of expansion of the x^N term in $f(x) = (x^0 + .. + x^M)^G$.

```python
import numpy as np

def generate_basis_states_occups_N(N: int, M: int, G: int) -> List[np.ndarray]:
    """Generate the occupations that give a total of N particles

    Args:
        N (int): Target particle number
        M (int): Maximum occupation per site
        G (int): Total number of sites

    Returns:
        List[np.ndarray]: List of occupations
    """
    def _grow(arrays: List[np.ndarray], _results: List[np.ndarray] = []) ->
    ↪ List[np.ndarray]:
        next_arr = []
        for occ in arrays:
            s = np.sum(occ)
            if s == N:
                _results.append(occ) # store valid occ into accumulator
            if s < N and len(occ) < G: # continue
                next_arr += [np.append(occ, _i) for _i in range(M + 1)]

        if len(next_arr):
            return _grow(next_arr, _results)
        return _results

    # we may also optionally cache the results
    _results = _grow(next_arr)
    return [occ_pad_zeros(combi, G) for combi in _results]

def occ_pad_zeros(combi_arr: np.ndarray, G: int) -> np.ndarray:
    """Pad zeros at the back of an occupational array

    Args:
        combi_arr (np.ndarray): Combination array
        G (int): Total number of sites

    Returns:
        np.ndarray: combination
    """
    ret = np.zeros(shape = (self.L,), dtype = np.int_)
    ret[:len(combi_arr)] = combi_arr
    return ret
```

Source Code E.1: Generating N-particle basis states using a pruned multi-ary tree.

Since each term $(x^0 + .. + x^M)$ is a geometric series, we can rewrite $f(x)$ as:

$$f(x) = \left(x^0 + .. + x^M\right)^G = \left(\frac{1 - x^{M+1}}{1 - x}\right)^G = (1 - x^{M+1})^G \cdot (1 - x)^{-G} \,. \tag{E.1}$$

Using the (negative) binomial theorem, we have:

$$f(x) = \left[\sum_{k=0}^{G} (-1)^k \binom{G}{k} x^{k(M+1)}\right] \cdot \left[\sum_{q=0}^{\infty} \binom{G+q-1}{q} x^q\right] . \tag{E.2}$$

As such, to obtain the exponent N of the x^N-term, the condition $k(M+1) + q \stackrel{!}{=} N$ must be fulfilled. Since we can define a unique q that is relevant for each unique k with $q = N - k(M+1)$, we can calculate the coefficient C_N of x^N as:

$$\begin{aligned} C_N &= \sum_{k=0}^{G} (-1)^k \binom{G}{k} \binom{G + N - k(M+1) - 1}{N - k(M+1)} \\ &= \sum_{k=0}^{G} (-1)^k \binom{G}{k} \binom{G + N - k(M+1) - 1}{G - 1} \,, \end{aligned} \tag{E.3}$$

with the condition $k(M+1) \leq N$

A minimum working example in Python for the above calculation may be found in source code E.2.

```python
import scipy.special.comb

def count_basis_states_N(N: int, M: int, G: int) -> int:
    """
    Calculate the number of ways to distribute N particles among L sites with maximum occupancy M.

    Args:
        N (int): Total number of particles
        M (int): Maximum occupation per site
        G (int): Total number of sites

    Returns:
        int: Number of possible arrangements i.e. the number of Fock Basis States with N particles
    """

    # Check if the problem is possible
    if N > G * M or N < 0:
        return 0

    xn_coeff = 0
    for k in range(G):
        # Condition is that (G + N - k(m+1) - 1) >= (G - 1) \equiv k(m+1) <= N
        if k*(M+1) > N:
            break

        _sign  = 1 if k % 2 == 0 else -1

        term_1 = scipy.special.comb(G, k, exact = True)

        _n = G + N - k*(M+1) - 1
        _r = G - 1
        term_2 = scipy.special.comb(_n, _r, exact = True)

        xn_coeff += _sign * term_1 * term_2

    return xn_coeff
```

Source Code E.2: Calculating the number of N-particle basis states by finding the coefficient of expansion of the x^N term in $(x^0 + .. + x^M)^G$.

Appendix F

Indexing

We document here how the indexing is implemented in the case of a system with or without periodic boundary conditions. Here, we intentionally include input validation in the code as an example of how we can ensure the correctness of our code, and allow easy debugging should we make a mistake somewhere else.

```python
import numpy as np

def get_index(r: int | np.ndarray, l: int | np.ndarray, rungs: int, legs: int, PBC: bool) -> int | np.ndarray:
    """0-indexed, Maps the site index (r, l) to the corresponding (linear) index in the lattice

    For the PBC case, we investigate the properties of the ring.
    See the code comment for more information.

    Args:
        r (int): rung-index
        l (int): leg-index
        rungs (int): number of rungs
        legs (int): number of legs
        PBC (bool): periodic boundary conditions

    Returns:
        int: index in the lattice
    """
    # Check if within range
    if isinstance(r, np.ndarray) and isinstance(l, np.ndarray):
        # https://stackoverflow.com/a/10542347/3211506
        if not np.all((0 <= r) & (r < rungs)) or not np.all((0 <= l) & (l < legs)):
            raise IndexError(f"(r, l) out of range, (maxr, maxl) = ({rungs-1}, {legs-1})")
        if r.shape != l.shape:
            raise TypeError(f"r and l must have the same shape")
    elif isinteger(r) and isinteger(l):
        if not (0 <= r < rungs and 0 <= l < legs):
```

```
            raise IndexError(f"(r, l) = ({r}, {l}) out of range, (maxr, maxl) =
            ↪  ({rungs-1}, {legs-1})")
    else:
        raise TypeError(f"r and l must be integers or numpy array of integers")

    if not PBC:
        return r * legs + l
    else:
        def _calc_idx(r, l):
            arr_idx = 0

            # We map this to the single ring case, and then extend it
            # See drawings for more information
            # Doing the snake means if that if split the ring down the middle, we get
            ↪  1 3 5 7 ... on one side
            #   and 2 4 6 ... on the other side (but in the returning direction)
            # So we do a case differentiation to check which side of the ring a
            ↪  particular node is
            # then map it accordingly

            # To obtain the mapping for the ladder case (i.e. legs > 1), we just need
            ↪  to multiply the indices
            # by the number of legs, as the pattern is the same, just that the
            ↪  increments goes in multiples of
            # numlegs

            # do the rungs (x-coord)
            if 0 < r <= (rungs // 2):
                arr_idx = 2*r - 1
            elif r > (rungs  // 2):
                arr_idx = 2*(rungs - r)

            arr_idx *= legs
            arr_idx += l # y-coord

            return arr_idx

        if isinteger(r) and isinteger(l):
            return _calc_idx(r, l)
        elif isinstance(r, np.ndarray) and isinstance(l, np.ndarray):
            # See also https://stackoverflow.com/a/2704693
            return np.vectorize(_calc_idx)(r, l)

def get_rl(self, idx: int, rungs: int, legs: int, PBC: bool) -> Tuple[int, int]:
    """0-indexed, inverse function of get_index(r, l)

    Args:
        idx (int): lattice index
        rungs (int): number of rungs
        legs (int): number of legs
        PBC (bool): periodic boundary conditions

```

```
75          Returns:
76              Tuple[int, int]: (r, l)
77          """
78
79          if not (0 <= idx < rungs*legs):
80              raise IndexError(f"idx = {idx} out of range, max_idx = ({(rungs * legs) -
                ↪  1})")
81
82          _l = idx % legs
83
84          if not PBC:
85              _r = idx // legs
86          else:
87              _x = idx // legs
88              _r = (rungs - _x//2) if (_x % 2 == 0) else (_x//2 + 1)
89
90          return (_r, _l)
91
92      def isinteger(obj: any) -> bool:
93          if not isnumber(obj):
94              return False
95
96          try:
97              return float(obj).is_integer()
98          except TypeError:
99              return False
```

List of Figures

Acronyms

DMRG density matrix renormalisation group. 31
ED exact diagonalisation. 3, 21, 23–25, 27, 29, 31, 35, 36, 47–50, 54, 55, 57, 77

GSE global subspace expansion. 33, 48

HBH Hofstadter-Bose-Hubbard. 2, 19, 62

LSE local subspace expansion. 33, 48

MPO matrix product operator. 31

MPS matrix product state. 3, 4, 23–25, 31, 33, 35, 47–50, 54, 55
s.e.m. standard error of the mean. 36, 50

SVD singular value decomposition. 31
TDVP time-dependent variational principle. 33, 47, 48

1TDVP single-site time-dependent variational principle. 33
TEBD time-evolving block-decimation. 33

Glossary

method A method is a named sequence of instructions, also known as a subroutine or a function, that performs a specific task. This differs from the generic definition of a method (= methodology) as a procedure or process for achieving a specific goal.. 24–29, 32

Bibliography

[1] J. Hubbard. "Electron Correlations in Narrow Energy Bands". In: *Proceedings of the Royal Society of London. Series A, Mathematical and Physical Sciences* 276.1365 (1963), pp. 238–257. ISSN: 0080-4630. JSTOR: 2414761. URL: https://www.jstor.org/stable/2414761 (visited on 15/05/2025) (cit. on p. 1).

[2] Daniel P. Arovas et al. "The Hubbard Model". In: *Annual Review of Condensed Matter Physics* 13 (Volume 13, 2022 10th Mar. 2022), pp. 239–274. ISSN: 1947-5454, 1947-5462. DOI: 10.1146/annurev-conmatphys-031620-102024. URL: https://www.annualreviews.org/content/journals/10.1146/annurev-conmatphys-031620-102024 (visited on 30/05/2025) (cit. on p. 1).

[3] J. G. Bednorz and K. A. Müller. "Possible highTc Superconductivity in the Ba-La-Cu-O System". In: *Zeitschrift für Physik B Condensed Matter* 64.2 (1st June 1986), pp. 189–193. ISSN: 1431-584X. DOI: 10.1007/BF01303701. URL: https://doi.org/10.1007/BF01303701 (visited on 06/07/2025) (cit. on p. 1).

[4] Leon N. Cooper. "Bound Electron Pairs in a Degenerate Fermi Gas". In: *Physical Review* 104.4 (15th Nov. 1956), pp. 1189–1190. DOI: 10.1103/PhysRev.104.1189. URL: https://link.aps.org/doi/10.1103/PhysRev.104.1189 (visited on 06/07/2025) (cit. on p. 1).

[5] J. Bardeen, L. N. Cooper and J. R. Schrieffer. "Microscopic Theory of Superconductivity". In: *Physical Review* 106.1 (1st Apr. 1957), pp. 162–164. DOI: 10.1103/PhysRev.106.162. URL: https://link.aps.org/doi/10.1103/PhysRev.106.162 (visited on 06/07/2025) (cit. on p. 1).

[6] J. Bardeen, L. N. Cooper and J. R. Schrieffer. "Theory of Superconductivity". In: *Physical Review* 108.5 (1st Dec. 1957), pp. 1175–1204. DOI: 10.1103/PhysRev.108.1175. URL: https://link.aps.org/doi/10.1103/PhysRev.108.1175 (visited on 06/07/2025) (cit. on p. 1).

[7] P. W. Anderson. "The Resonating Valence Bond State in La2CuO4 and Superconductivity". In: *Science* 235.4793 (6th Mar. 1987), pp. 1196–1198. DOI: 10.1126/science.235.4793.1196. URL: https://www.science.org/doi/10.1126/science.235.4793.1196 (visited on 06/07/2025) (cit. on p. 1).

[8] "From the Cuprate Compounds to the Hubbard Model". In: *Quantum Electron Liquids and High-T c Superconductivity*. Vol. 38. Berlin, Heidelberg: Springer Berlin Heidelberg, 1995, pp. 127–149. ISBN: 978-3-540-60503-4. DOI: 10.1007/978-3-540-47678-8_6. URL: http://link.springer.com/10.1007/978-3-540-47678-8_6 (visited on 30/05/2025) (cit. on p. 1).

[9] Simons Collaboration on the Many-Electron Problem et al. "Solutions of the Two-Dimensional Hubbard Model: Benchmarks and Results from a Wide Range of Numerical Algorithms".

In: *Physical Review X* 5.4 (14th Dec. 2015), p. 041041. DOI: 10.1103/PhysRevX.5.041041. URL: https://link.aps.org/doi/10.1103/PhysRevX.5.041041 (visited on 06/07/2025) (cit. on p. 1).

[10] H. A. Gersch and G. C. Knollman. "Quantum Cell Model for Bosons". In: *Physical Review* 129.2 (15th Jan. 1963), pp. 959–967. DOI: 10.1103/PhysRev.129.959. URL: https://link.aps.org/doi/10.1103/PhysRev.129.959 (visited on 30/05/2025) (cit. on p. 1).

[11] Douglas R. Hofstadter. "Energy Levels and Wave Functions of Bloch Electrons in Rational and Irrational Magnetic Fields". In: *Physical Review B* 14.6 (15th Sept. 1976), pp. 2239–2249. DOI: 10.1103/PhysRevB.14.2239. URL: https://link.aps.org/doi/10.1103/PhysRevB.14.2239 (visited on 10/06/2025) (cit. on pp. 1, 7).

[12] M. Hafezi et al. "Fractional Quantum Hall Effect in Optical Lattices". In: *Physical Review A* 76.2 (28th Aug. 2007), p. 023613. DOI: 10.1103/PhysRevA.76.023613. URL: https://link.aps.org/doi/10.1103/PhysRevA.76.023613 (visited on 06/07/2025) (cit. on p. 2).

[13] Rebecca N. Palmer, Alexander Klein and Dieter Jaksch. "Optical Lattice Quantum Hall Effect". In: *Physical Review A* 78.1 (7th July 2008), p. 013609. DOI: 10.1103/PhysRevA.78.013609. URL: https://link.aps.org/doi/10.1103/PhysRevA.78.013609 (visited on 06/07/2025) (cit. on p. 2).

[14] G. Möller and N. R. Cooper. "Composite Fermion Theory for Bosonic Quantum Hall States on Lattices". In: *Physical Review Letters* 103.10 (4th Sept. 2009), p. 105303. DOI: 10.1103/PhysRevLett.103.105303. URL: https://link.aps.org/doi/10.1103/PhysRevLett.103.105303 (visited on 06/07/2025) (cit. on p. 2).

[15] Alexander Impertro et al. "Strongly Interacting Meissner Phases in Large Bosonic Flux Ladders". In: *Nature Physics* (2nd May 2025), pp. 1–7. ISSN: 1745-2481. DOI: 10.1038/s41567-025-02890-0. URL: https://www.nature.com/articles/s41567-025-02890-0 (visited on 16/05/2025) (cit. on pp. 2, 19–21, 50, 54).

[16] Stefan Kessler and Florian Marquardt. "Single-Site-Resolved Measurement of the Current Statistics in Optical Lattices". In: *Physical Review A* 89.6 (3rd June 2014), p. 061601. ISSN: 1050-2947, 1094-1622. DOI: 10.1103/PhysRevA.89.061601. arXiv: 1309.3890 [cond-mat]. URL: http://arxiv.org/abs/1309.3890 (visited on 24/04/2025) (cit. on pp. 2, 9, 11, 12, 14, 21, 29, 30, 35, 53, 62).

[17] Alexander Impertro et al. "Local Readout and Control of Current and Kinetic Energy Operators in Optical Lattices". In: *Physical Review Letters* 133.6 (5th Aug. 2024), p. 063401. ISSN: 0031-9007, 1079-7114. DOI: 10.1103/PhysRevLett.133.063401. URL: https://link.aps.org/doi/10.1103/PhysRevLett.133.063401 (visited on 25/04/2025) (cit. on pp. 2, 11, 19, 21, 36).

[18] Maximilian Buser, Ulrich Schollwöck and Fabian Grusdt. "Snapshot-Based Characterization of Particle Currents and the Hall Response in Synthetic Flux Lattices". In: *Physical Review A* 105.3 (3rd Mar. 2022), p. 033303. DOI: 10.1103/PhysRevA.105.033303. URL: https://link.aps.org/doi/10.1103/PhysRevA.105.033303 (visited on 06/07/2025) (cit. on p. 2).

[19] Alexander Impertro et al. *Realization of Strongly-Interacting Meissner Phases in Large Bosonic Flux Ladders*. 12th Dec. 2024. DOI: 10.48550/arXiv.2412.09481. arXiv: 2412.09481 [cond-mat]. URL: http://arxiv.org/abs/2412.09481 (visited on 21/04/2025). Prepublished (cit. on pp. 3, 9, 17, 19, 23, 35, 47, 49, 61, 62).

[20] V. Fock. "Konfigurationsraum und zweite Quantelung". In: *Zeitschrift für Physik* 75.9 (1st Sept. 1932), pp. 622–647. ISSN: 0044-3328. DOI: 10.1007/BF01344458. URL: https://doi.org/10.1007/BF01344458 (visited on 19/04/2025) (cit. on p. 5).

[21] Alexander Altland and Ben Simons. "2.1 Introduction to Second Quantization". In: *Condensed Matter Field Theory*. Second edition. Leiden: Cambridge University Press, 2010, pp. 40–50. ISBN: 978-0-511-78928-1. URL: https://nucleares.unam.mx/~alberto/apuntes/altland.pdf (cit. on p. 5).

[22] Jens Eisert. "Advanced Quantum Mechanics – Chapter 3: Elements of Second Quantization". Berlin, 2018. URL: https://www.physik.fu-berlin.de/en/einrichtungen/ag/ag-eisert/teaching/ws18-19/AdvancedQuantumMechanicsChapter3.pdf (visited on 20/04/2025) (cit. on p. 6).

[23] Monika Aidelsburger. "Artificial gauge fields with ultracold atoms in optical lattices". PhD Thesis. Ludwig-Maximilians-Universität München, 4th Feb. 2015. URL: https://edoc.ub.uni-muenchen.de/18148/ (visited on 08/06/2025) (cit. on pp. 6, 7).

[24] Maximilian Buser. "Matrix-product-state based studies of bosonic flux ladders". PhD Thesis. Ludwig-Maximilians-Universität München, 12th Apr. 2021. URL: https://edoc.ub.uni-muenchen.de/27836/ (visited on 22/11/2023) (cit. on pp. 6–9, 64).

[25] Y. Aharonov and D. Bohm. "Significance of Electromagnetic Potentials in the Quantum Theory". In: *Physical Review* 115.3 (1st Aug. 1959), pp. 485–491. DOI: 10.1103/PhysRev.115.485. URL: https://link.aps.org/doi/10.1103/PhysRev.115.485 (visited on 08/06/2025) (cit. on p. 6).

[26] Simon Wächter. *The Aharonov-Bohm Effect | Proseminar on Algebra, Topology & Group Theory in Physics*. 30th Mar. 2018. URL: https://ethz.ch/content/dam/ethz/special-interest/phys/theoretical-physics/itp-dam/documents/gaberdiel/proseminar_fs2018/06_Waechter.pdf (visited on 08/06/2025) (cit. on p. 6).

[27] R. Peierls. "Zur Theorie des Diamagnetismus von Leitungselektronen". In: *Zeitschrift für Physik* 80.11 (1st Nov. 1933), pp. 763–791. ISSN: 0044-3328. DOI: 10.1007/BF01342591. URL: https://doi.org/10.1007/BF01342591 (visited on 04/06/2025) (cit. on pp. 6, 7).

[28] J. M. Luttinger. "The Effect of a Magnetic Field on Electrons in a Periodic Potential". In: *Physical Review* 84.4 (15th Nov. 1951), pp. 814–817. DOI: 10.1103/PhysRev.84.814. URL: https://link.aps.org/doi/10.1103/PhysRev.84.814 (visited on 08/06/2025) (cit. on p. 7).

[29] Maximilian Buser et al. "Interacting Bosonic Flux Ladders with a Synthetic Dimension: Ground-state Phases and Quantum Quench Dynamics". In: *Physical Review A* 102.5 (16th Nov. 2020), p. 053314. DOI: 10.1103/PhysRevA.102.053314. URL: https://link.aps.org/doi/10.1103/PhysRevA.102.053314 (visited on 22/01/2024) (cit. on p. 8).

[30] Matthew P. A. Fisher et al. "Boson Localization and the Superfluid-Insulator Transition". In: *Physical Review B* 40.1 (1st July 1989), pp. 546–570. DOI: 10.1103/PhysRevB.40.546. URL: https://link.aps.org/doi/10.1103/PhysRevB.40.546 (visited on 12/06/2025) (cit. on p. 8).

[31] Markus Greiner et al. "Quantum Phase Transition from a Superfluid to a Mott Insulator in a Gas of Ultracold Atoms". In: *Nature* 415.6867 (Jan. 2002), pp. 39–44. ISSN: 1476-4687. DOI: 10.1038/415039a. URL: https://www.nature.com/articles/415039a (visited on 12/06/2025) (cit. on p. 8).

[32] Dario Hügel and Belén Paredes. "Chiral Ladders and the Edges of Quantum Hall Insulators". In: *Physical Review A* 89.2 (14th Feb. 2014), p. 023619. DOI: 10.1103/PhysRevA.89.023619. URL: https://link.aps.org/doi/10.1103/PhysRevA.89.023619 (visited on 11/06/2025) (cit. on p. 8).

[33] Akiyuki Tokuno and Antoine Georges. "Ground States of a Bose–Hubbard Ladder in an Artificial Magnetic Field: Field-Theoretical Approach". In: *New Journal of Physics* 16.7 (July 2014), p. 073005. ISSN: 1367-2630. DOI: 10.1088/1367-2630/16/7/073005. URL: https://dx.doi.org/10.1088/1367-2630/16/7/073005 (visited on 11/06/2025) (cit. on p. 8).

[34] S. Greschner et al. "Symmetry-Broken States in a System of Interacting Bosons on a Two-Leg Ladder with a Uniform Abelian Gauge Field". In: *Physical Review A* 94.6 (22nd Dec. 2016), p. 063628. DOI: 10.1103/PhysRevA.94.063628. URL: https://link.aps.org/doi/10.1103/PhysRevA.94.063628 (visited on 24/04/2025) (cit. on p. 8).

[35] E. Orignac and T. Giamarchi. "Meissner Effect in a Bosonic Ladder". In: *Physical Review B* 64.14 (21st Sept. 2001), p. 144515. DOI: 10.1103/PhysRevB.64.144515. URL: https://link.aps.org/doi/10.1103/PhysRevB.64.144515 (visited on 16/05/2025) (cit. on p. 8).

[36] Alexandru Petrescu and Karyn Le Hur. "Bosonic Mott Insulator with Meissner Currents". In: *Physical Review Letters* 111.15 (7th Oct. 2013), p. 150601. DOI: 10.1103/PhysRevLett.111.150601. URL: https://link.aps.org/doi/10.1103/PhysRevLett.111.150601 (visited on 12/06/2025) (cit. on p. 8).

[37] M. Di Dio et al. "Persisting Meissner State and Incommensurate Phases of Hard-Core Boson Ladders in a Flux". In: *Physical Review B* 92.6 (26th Aug. 2015), p. 060506. DOI: 10.1103/PhysRevB.92.060506. URL: https://link.aps.org/doi/10.1103/PhysRevB.92.060506 (visited on 12/06/2025) (cit. on p. 8).

[38] M. Piraud et al. "Vortex and Meissner Phases of Strongly Interacting Bosons on a Two-Leg Ladder". In: *Physical Review B* 91.14 (10th Apr. 2015), p. 140406. DOI: 10.1103/PhysRevB.91.140406. URL: https://link.aps.org/doi/10.1103/PhysRevB.91.140406 (visited on 12/06/2025) (cit. on pp. 8, 19).

[39] J. Monecke. "Conduction in Narrow Energy Bands". In: *physica status solidi (b)* 51.1 (May 1972), pp. 369–376. ISSN: 0370-1972, 1521-3951. DOI: 10.1002/pssb.2220510137. URL: https://onlinelibrary.wiley.com/doi/10.1002/pssb.2220510137 (visited on 16/05/2025) (cit. on p. 9).

[40] D. Cabib and T. A. Kaplan. "On the Definition of the Current Operator Application to the Hubbard Model". In: *physica status solidi (b)* 58.1 (July 1973), pp. 85–90. ISSN: 0370-1972, 1521-3951. DOI: 10.1002/pssb.2220580108. URL: https://onlinelibrary.wiley.com/doi/10.1002/pssb.2220580108 (visited on 24/04/2025) (cit. on p. 9).

[41] J. Monecke. "On the Definition of the Current Operator Application to the Hubbard Model". In: *physica status solidi (b)* 62.2 (Apr. 1974), pp. 417–423. ISSN: 0370-1972, 1521-3951. DOI: 10.1002/pssb.2220620210. URL: https://onlinelibrary.wiley.com/doi/10.1002/pssb.2220620210 (visited on 16/05/2025) (cit. on p. 9).

[42] E. Marsch. "On the Frequency-dependent Conductivity and the Current Operator of the Hubbard Model". In: *physica status solidi (b)* 72.2 (Dec. 1975). ISSN: 0370-1972, 1521-3951. DOI: 10.1002/pssb.2220720248. URL: https://onlinelibrary.wiley.com/doi/10.1002/pssb.2220720248 (visited on 24/04/2025) (cit. on p. 9).

[43] Waseem S. Bakr et al. "A Quantum Gas Microscope for Detecting Single Atoms in a Hubbard-regime Optical Lattice". In: *Nature* 462.7269 (5th Nov. 2009), pp. 74–77. ISSN: 1476-4687. DOI: 10.1038/nature08482. PMID: 19890326 (cit. on p. 11).

[44] Jacob F. Sherson et al. "Single-Atom-Resolved Fluorescence Imaging of an Atomic Mott Insulator". In: *Nature* 467.7311 (2nd Sept. 2010), pp. 68–72. ISSN: 1476-4687. DOI: 10.1038/nature09378. PMID: 20720540 (cit. on p. 11).

[45] Annabelle Bohrdt. "Visualizing Atom Currents in Optical Lattices". In: *Physics* 17 (5th Aug. 2024), p. 120. DOI: 10.1103/PhysRevLett.133.063401. URL: https://physics.aps.org/articles/v17/120 (visited on 19/06/2025) (cit. on p. 11).

[46] Claude Cohen-Tannoudji, Bernard Diu and Frank Laloe. "Complement G III: The Schrödinger and Heisenberg Pictures". In: *Quantum Mechanics: Volume I: Basic Concepts, Tools, and Applications*. Trans. by Nicole Ostrowsky and Daniel Ostrowsky. 2. Edition. Weinheim: Wiley-VCH Verlag GmbH & Co. KGaA, 2020, pp. 317–319. ISBN: 978-3-527-82270-6 (cit. on pp. 13, 62).

[47] Andrei A. Stepanenko and Marco Di Liberto. "Vortex Bound States in Dimerized π-Flux Optical Lattices: Characterization, State Preparation and Current Measurement". In: *Physical Review A* 110.6 (23rd Dec. 2024), p. L061304. ISSN: 2469-9926, 2469-9934. DOI: 10.1103/PhysRevA.110.L061304. arXiv: 2410.06184 [cond-mat]. URL: http://arxiv.org/abs/2410.06184 (visited on 22/06/2025) (cit. on p. 13).

[48] Josiah Willard Gibbs. *Elementary Principles in Statistical Mechanics, Developed with Especial Reference to the Rational Foundation of Thermodynamics*. C. Scribner's Sons New York, 1902. URL: http://gallica.bnf.fr/ark:/12148/bpt6k99748x (visited on 15/06/2025) (cit. on p. 16).

[49] Claude Cohen-Tannoudji, Bernard Diu and Frank Laloe. "Appendix VI: Brief Review of Quantum Statistical Mechanics". In: *Quantum Mechanics: Volume III: Fermions, Bosons, Photons, Correlations, and Entanglement*. Trans. by Nicole Ostrowsky and Daniel Ostrowsky. 1. Auflage. Weinheim: Wiley-VCH Verlag GmbH & Co. KGaA, 2020. ISBN: 978-3-527-82274-4 (cit. on p. 16).

[50] Peter Mohr et al. *CODATA Recommended Values of the Fundamental Physical Constants: 2022*. 30th Aug. 2024. DOI: 10.48550/arXiv.2409.03787. arXiv: 2409.03787 [hep-ph]. URL: http://arxiv.org/abs/2409.03787 (visited on 16/06/2025). Pre-published (cit. on p. 16).

[51] Gaoyong Sun and André Eckardt. "Optimal Frequency Window for Floquet Engineering in Optical Lattices". In: *Physical Review Research* 2.1 (2nd Mar. 2020), p. 013241. DOI: 10.1103/PhysRevResearch.2.013241. URL: https://link.aps.org/doi/10.1103/PhysRevResearch.2.013241 (visited on 06/07/2025) (cit. on p. 19).

[52] Melih Okan. "Controlling Ultracold Fermions under a Quantum Gas Microscope". PhD Thesis. Massachusetts Institute of Technology, 2018. URL: https://dspace.mit.edu/handle/1721.1/115688 (visited on 06/07/2025) (cit. on p. 20).

[53] Marshall T. DePue et al. "Unity Occupation of Sites in a 3D Optical Lattice". In: *Physical Review Letters* 82.11 (15th Mar. 1999), pp. 2262–2265. DOI: 10.1103/PhysRevLett.82.2262. URL: https://link.aps.org/doi/10.1103/PhysRevLett.82.2262 (visited on 06/07/2025) (cit. on p. 20).

[54] Kalle-Antti Suominen. "Theories for Cold Atomic Collisions in Light Fields". In: *Journal of Physics B: Atomic, Molecular and Optical Physics* 29.24 (Dec. 1996), p. 5981. ISSN: 0953-4075. DOI: 10.1088/0953-4075/29/24/008. URL: https://dx.doi.org/10.1088/0953-4075/29/24/008 (visited on 06/07/2025) (cit. on p. 20).

[55] Alexander Impertro. personal communication. 23rd Sept. 2024 (cit. on pp. 20, 40, 47).

[56] Marvin Weinstein, Assa Auerbach and V. Ravi Chandra. *Reducing Memory Cost of Exact Diagonalization Using Singular Value Decomposition*. arXiv.org. 29th Apr. 2011. DOI: 10.1103/PhysRevE.84.056701. URL: https://arxiv.org/abs/1105.0007v2 (visited on 20/04/2025) (cit. on p. 23).

[57] D. Perez-Garcia et al. *Matrix Product State Representations*. 14th May 2007. DOI: 10.48550/arXiv.quant-ph/0608197. arXiv: quant-ph/0608197. URL: http://arxiv.org/abs/quant-ph/0608197 (visited on 20/04/2025). Pre-published (cit. on p. 23).

[58] [SW] Mattia Moroder et al., *evos (Branch yudong)*. URL: https://gitlab.physik.lmu.de/Martin.Grundner/evos/-/tree/yudong (cit. on p. 24).

[59] Claudius Hubig et al. *The SyTen Toolkit*. URL: https://syten.eu (cit. on pp. 24, 31, 54).

[60] Claudius Hubig. "Symmetry-Protected Tensor Networks". PhD thesis. LMU München, 2017. URL: https://edoc.ub.uni-muenchen.de/21348/ (cit. on pp. 24, 31, 54).

[61] Anthony Scopatz and Kathryn D. Huff. "Chapter 6: Classes and Objects". In: *Effective Computation in Physics: Field Guide to Research with Python*. First edition. ProQuest E-Book Central. Beijing Boston Farnham Sebastopol Tokyo: O'Reilly, 2015, pp. 117–142. ISBN: 978-1-4919-0153-3. URL: https://lilith.fisica.ufmg.br/~dickman/transfers/comp/textos/Effective%20Computation%20in%20Physics%20(Python).pdf (visited on 03/07/2025) (cit. on p. 24).

[62] Anthony Scopatz and Kathryn D. Huff. "Chapter 18: Testing". In: *Effective Computation in Physics: Field Guide to Research with Python*. First edition. ProQuest E-Book Central. Beijing Boston Farnham Sebastopol Tokyo: O'Reilly, 2015, pp. 403–423. ISBN: 978-1-4919-0153-3. URL: https://lilith.fisica.ufmg.br/~dickman/transfers/comp/textos/Effective%20Computation%20in%20Physics%20(Python).pdf (visited on 03/07/2025) (cit. on pp. 24, 39).

[63] Immanuel Bloch. "Ultracold Quantum Gases in Optical Lattices". In: *Nature Physics* 1.1 (Oct. 2005), pp. 23–30. ISSN: 1745-2481. DOI: 10.1038/nphys138. URL: https://www.nature.com/articles/nphys138 (visited on 23/04/2025) (cit. on p. 26).

[64] Alexander Impertro. personal communication. 27th Aug. 2024 (cit. on pp. 26, 36–38).

[65] *Fcntl - The Fcntl and Ioctl System Calls*. Python documentation. URL: https://docs.python.org/3/library/fcntl.html (visited on 06/07/2025) (cit. on p. 26).

[66] [SW], *opencollab/arpack-ng* 1st July 2025. opencollab. URL: https://github.com/opencollab/arpack-ng(visited on 04/07/2025) (cit. on p. 27).

[67] R. B. Lehoucq, D. C. Sorensen and C. Yang. *ARPACK Users' Guide: Solution of Large-Scale Eigenvalue Problems with Implicitly Restarted Arnoldi Methods*. Society for Industrial and Applied Mathematics, Jan. 1998. ISBN: 978-0-89871-407-4. DOI: 10.1137/1.9780898719628. URL: http://epubs.siam.org/doi/book/10.1137/1.9780898719628 (visited on 04/07/2025) (cit. on p. 27).

[68] E. Anderson et al. *LAPACK Users' Guide*. Third. Philadelphia, PA: Society for Industrial and Applied Mathematics, 1999. ISBN: 0-89871-447-8 (paperback) (cit. on p. 28).

[69] Anthony Scopatz and Kathryn D. Huff. "Chapter 5: Operating with Functions". In: *Effective Computation in Physics: Field Guide to Research with Python*. First edition. ProQuest E-Book Central. Beijing Boston Farnham Sebastopol Tokyo: O'Reilly, 2015, pp. 95–116. ISBN: 978-1-4919-0153-3. URL: https://lilith.fisica.ufmg.br/~dickman/transfers/comp/textos/Effective%20Computation%20in%20Physics%20(Python).pdf (visited on 03/07/2025) (cit. on p. 28).

[70] "IEEE Standard for Floating-Point Arithmetic". In: *IEEE Std 754-2019 (Revision of IEEE 754-2008)* (July 2019), pp. 1–84. DOI: 10.1109/IEEESTD.2019.8766229. URL: https://ieeexplore.ieee.org/document/8766229 (visited on 05/07/2025) (cit. on p. 29).

[71] Steven R. White. "Density Matrix Formulation for Quantum Renormalization Groups". In: *Physical Review Letters* 69.19 (9th Nov. 1992), pp. 2863–2866. DOI: 10.1103/PhysRevLett.69.2863. URL: https://link.aps.org/doi/10.1103/PhysRevLett.69.2863 (visited on 05/07/2025) (cit. on p. 31).

[72] Steven R. White. "Density-Matrix Algorithms for Quantum Renormalization Groups". In: *Physical Review B* 48.14 (1st Oct. 1993), pp. 10345–10356. DOI: 10.1103/PhysRevB.48.10345. URL: https://link.aps.org/doi/10.1103/PhysRevB.48.10345 (visited on 05/07/2025) (cit. on p. 31).

[73] Ulrich Schollwöck. "The Density-Matrix Renormalization Group in the Age of Matrix Product States". In: *Annals of Physics*. January 2011 Special Issue 326.1 (1st Jan. 2011), pp. 96–192. ISSN: 0003-4916. DOI: 10.1016/j.aop.2010.09.012. URL: https://www.sciencedirect.com/science/article/pii/S0003491610001752 (visited on 05/07/2025) (cit. on p. 31).

[74] F. Verstraete, J. J. García-Ripoll and J. I. Cirac. "Matrix Product Density Operators: Simulation of Finite-Temperature and Dissipative Systems". In: *Physical Review Letters* 93.20 (12th Nov. 2004), p. 207204. DOI: 10.1103/PhysRevLett.93.207204. URL: https://link.aps.org/doi/10.1103/PhysRevLett.93.207204 (visited on 05/07/2025) (cit. on p. 31).

[75] Sukhwinder Singh, Robert N. C. Pfeifer and Guifre Vidal. "Tensor Network States and Algorithms in the Presence of a Global U(1) Symmetry". In: *Physical Review B* 83.11 (15th Mar. 2011), p. 115125. DOI: 10.1103/PhysRevB.83.115125. URL: https://link.aps.org/doi/10.1103/PhysRevB.83.115125 (visited on 05/07/2025) (cit. on p. 32).

[76] Philipp Westhoff, Sebastian Paeckel and Mattia Moroder. *Fast and Direct Preparation of a Genuine Lattice BEC via the Quantum Mpemba Effect*. Version 2. 3rd June 2025. DOI: 10.48550/arXiv.2504.05549. arXiv: 2504.05549 [cond-mat]. URL: http://arxiv.org/abs/2504.05549 (visited on 06/07/2025). Pre-published (cit. on p. 33).

[77] Sebastian Paeckel et al. "Time-Evolution Methods for Matrix-Product States". In: *Annals of Physics* 411 (1st Dec. 2019), p. 167998. ISSN: 0003-4916. DOI: 10.1016/j.aop.2019.167998. URL: https://www.sciencedirect.com/science/article/pii/S0003491619302532 (visited on 06/07/2025) (cit. on p. 33).

[78] Masuo Suzuki. "Generalized Trotter's Formula and Systematic Approximants of Exponential Operators and Inner Derivations with Applications to Many-Body Problems". In: *Communications in Mathematical Physics* 51.2 (1st June 1976), pp. 183–190. ISSN: 1432-

0916. DOI: 10.1007/BF01609348. URL: https://doi.org/10.1007/BF01609348 (visited on 06/07/2025) (cit. on p. 33).

[79] Guifré Vidal. "Efficient Simulation of One-Dimensional Quantum Many-Body Systems". In: *Physical Review Letters* 93.4 (19th July 2004), p. 040502. DOI: 10.1103/PhysRevLett.93.040502. URL: https://link.aps.org/doi/10.1103/PhysRevLett.93.040502 (visited on 06/07/2025) (cit. on p. 33).

[80] Jutho Haegeman et al. "Time-Dependent Variational Principle for Quantum Lattices". In: *Physical Review Letters* 107.7 (10th Aug. 2011), p. 070601. DOI: 10.1103/PhysRevLett.107.070601. URL: https://link.aps.org/doi/10.1103/PhysRevLett.107.070601 (visited on 05/07/2025) (cit. on p. 33).

[81] Jutho Haegeman et al. "Unifying Time Evolution and Optimization with Matrix Product States". In: *Physical Review B* 94.16 (10th Oct. 2016), p. 165116. DOI: 10.1103/PhysRevB.94.165116. URL: https://link.aps.org/doi/10.1103/PhysRevB.94.165116 (visited on 05/07/2025) (cit. on p. 33).

[82] Mingru Yang and Steven R. White. *Time Dependent Variational Principle with Ancillary Krylov Subspace*. Version 2. 2nd July 2020. DOI: 10.48550/arXiv.2005.06104. arXiv: 2005.06104 [cond-mat]. URL: http://arxiv.org/abs/2005.06104 (visited on 05/07/2025). Pre-published (cit. on p. 33).

[83] Martin Grundner et al. *Cooper-Paired Bipolaronic Superconductors*. 25th Aug. 2023. DOI: 10.48550/arXiv.2308.13427. arXiv: 2308.13427 [cond-mat]. URL: http://arxiv.org/abs/2308.13427 (visited on 05/07/2025). Pre-published (cit. on p. 33).

[84] Sebastian Krinner et al. "Observation of Quantized Conductance in Neutral Matter". In: *Nature* 517.7532 (Jan. 2015), pp. 64–67. ISSN: 1476-4687. DOI: 10.1038/nature14049. URL: https://www.nature.com/articles/nature14049 (visited on 29/06/2025) (cit. on p. 36).

[85] Alexander Impertro et al. *Realization of Strongly-Interacting Meissner Phases in Large Bosonic Flux Ladders*. Edmond, 17th Mar. 2025. DOI: 10.17617/3.RXBLHT. URL: https://edmond.mpg.de/dataset.xhtml?persistentId=doi:10.17617/3.RXBLHT (visited on 01/07/2025) (cit. on pp. 49, 50).

[86] E. B. Davies. "Markovian Master Equations". In: *Communications in Mathematical Physics* 39.2 (1st June 1974), pp. 91–110. ISSN: 1432-0916. DOI: 10.1007/BF01608389. URL: https://doi.org/10.1007/BF01608389 (visited on 06/07/2025) (cit. on p. 54).

[87] Mattia Moroder et al. "Thermodynamics of the Quantum Mpemba Effect". In: *Physical Review Letters* 133.14 (4th Oct. 2024), p. 140404. ISSN: 0031-9007, 1079-7114. DOI: 10.1103/PhysRevLett.133.140404. arXiv: 2403.16959 [quant-ph]. URL: http://arxiv.org/abs/2403.16959 (visited on 06/07/2025) (cit. on p. 54).

[88] [SW] Yudong Sun, *Code Archive*. URL: https://gitlab.physik.lmu.de/Yudong.Sun/master-thesis-code-archive, SWHID: ⟨swh:1:dir:5a36ce9326d233eca3c946f3be91bda7f03777df;origin=https://gitlab.physik.uni-muenchen.de/Yudong.Sun/master-thesis-code-archive;visit=swh:1:snp:d3804804d27b315d9b9cb436b0994b716ddd4e8c;anchor=swh:1:rev:df9a0309f26652390e310a729790529e19b48f89⟩ (cit. on p. 55).

[89] Wolfram Research Inc. *Mathematica, Version 14.2*. Champaign, IL, 2024. URL: https://www.wolfram.com/mathematica (cit. on p. 66).

[90] Hangzhou DeepSeek Artificial Intelligence Basic Technology Research Co. Ltd. *DeepSeek. Large language model*. URL: https://chat.deepseek.com/ (visited on 24/06/2025) (cit. on p. 66).

[91] Philippe Flajolet and Robert Sedgewick. "Combinatorial Structures and Ordinary Generating Functions". In: *Analytic Combinatorics*. Cambridge ; New York: Cambridge University Press, 2009, pp. 15–94. ISBN: 978-0-521-89806-5. URL: https://algo.inria.fr/flajolet/Publications/book.pdf (cit. on p. 77).

Acknowledgements

I would like to begin by expressing my deepest gratitude to my supervisors Prof. Schollwöck and Dr. Sebastian Paeckel for their support, guidance and invaluable insights over this year of research, both professionally and personally, and also to Prof. Monika Aidelsburger for providing me with the opportunity to work on this rather unique collaboration project between experiments, theory and numerics. I am very grateful for the freedom (and luxury) that I had in this project to follow the science, even if it meant digging into the nitty gritty details of a paper that was published more than 10 years ago. I would also like to especially thank Dr. Paeckel for his patience, encouragements, and always trying to find the time to talk to me even when it got very busy.

Next I would like to thank Dr. Mattia Moroder and Dr. Thomas Köhler for the countless meetings that we have had, for proofreading and editing help, and their key insights into the physics and numerics of finite-temperature states, open quantum systems, and matrix product state calculations; and to Dr. Alexander Impertro and the Cs Lab for their experimental expertise and the long discussions we have had. This thesis project would not have been possible without them.

I am also grateful to my colleagues and office mates in the Schollwöck Chair: Zhaoxuan, Héloïse, Pit, Ke, Tomas, Julia, Tim, Henning, Damiano, Ludvik, Simon, Giovanni, Tizian, Fabian Pauw, Fabian Döschl, Annika, Ola, Alberto, Gaia, Hannah, and many more, listed in no particular order, for a great atomosphere in the group; and to my colleagues in the CIP and the RBG Physik for their support, especially when it came to working with computing cluster.

Finally, I would like thank my friends, my family and my partner Marlene for being there for me throughout my thesis; and everyone else not mentioned here that have helped me in one way or another throughout this thesis. Thank you!

The numerical computations were done on the ASC Cluster at LMU; We are grateful for the computational hours.

No computers were harmed in the making of this thesis.

Declaration:
I hereby declare that this thesis is my own work, and that I have not used any sources and aids other than those stated in the thesis.

München, 7th July 2025
Yudong Sun